REACTION KINETICS OF RARE EARTH AND ACTINIDE MATERIALS

by

Brian Jon Jaques

A dissertation

submitted in partial fulfillment

of the requirements for the degree of

Doctor of Philosophy in Materials Science and Engineering

Boise State University

May 2015

BOISE STATE UNIVERSITY GRADUATE COLLEGE

DEFENSE COMMITTEE AND FINAL READING APPROVALS

of the dissertation submitted by

Brian Jon Jaques

Dissertation Title: Reaction Kinetics of Rare Earth and Actinide Materials

Date of Final Oral Examination: 24 February 2015

The following individuals read and discussed the dissertation submitted by student Brian Jon Jaques, and they evaluated his presentation and response to questions during the final oral examination. They found that the student passed the final oral examination.

Darryl Butt, Ph.D.	Chair, Supervisory Committee
Amy J. Moll, Ph.D.	Member, Supervisory Committee
Dmitri Tenne, Ph.D.	Member, Supervisory Committee
Kenneth McClellan, Ph.D.	Member, Supervisory Committee

The final reading approval of the dissertation was granted by Darryl Butt, Ph.D., Chair of the Supervisory Committee. The dissertation was approved for the Graduate College by John R. Pelton, Ph.D., Dean of the Graduate College.

DEDICATION

This dissertation is dedicated to my wife and three children.

Rachel: Your constant words of encouragement, support, and patience has truly been testament of your support and our love. I love you. In ways, your commitment through this process has dwarfed mine, and for that I could not be more appreciative.

Trenton, Devin, and Allie: Simply your presence, curiosity, and compassion brightens my day, every day. You are unaware of the inspiration that you provide me day in and day out through your inquisitive nature, your love to learn, and your pure innocence. Thank you. You each have so much to learn, so much to see, and so much to do in this huge world; it is my vow to teach you, to show you, and to take you there.

I love you and am excited for the future.

Live as if you were to die tomorrow. Learn as if you were to live forever.

~ Mahatma Gandhi

Strive not to be a success, but rather to be of value.

~ Albert Einstein

ACKNOWLEDGEMENTS

My journey towards this dissertation was guided by people, both past and present, who have inspired, challenged, or supported me in one way or another. There are more people than I can list that have helped guide me and that have made my journey possible, but I wish to acknowledge a few of the instrumental ones here.

First and foremost, I would like to express my deepest appreciation to my committee chair, advisor, professor, mentor, and friend, Dr. Darryl Butt. Without his tireless guidance and support, this dissertation would not have been possible. Dr. Butt has provided me with opportunities I have never dreamed to have had and has significantly influenced the direction of my career. From my initial graduate fellowship to a graduate research assistant to an instructor to a research engineer, Dr. Butt has provided opportunities and inspiration to excel in my academics, my career, and my life. I do not think there is any way I could ever repay him, nor would he accept, so I can only hope that my plan to pay it forward is as fruitful to someone in my future as he has been for me.

I would like to thank Dr. Amy Moll and Dr. Don Plumlee for giving me an opportunity as an undergraduate research assistant in the Ceramic-MEMS laboratory. The mentoring and experience that you gave to me has served as both inspiration to pursue higher education and research as well as opening doors to opportunities that may not have

otherwise been available. You both continue to be very influential people that I admire very much.

Much of the research presented in this dissertation was conducted in affiliation with the Center for Advanced Energy Studies (CAES) and was partially funded by DOE NEUP grant #00120690. Of course, this work would not have been possible if the MSE department at BSU had not facilitated lab space nor presented such a great opportunity for me to continue my education. The MSE department has been committed to me and its students by providing a very positive, competent, and ambitious staff that everyone can grow and prosper from.

In addition to the acknowledgements presented at the end of each chapter, there are a few others that deserve recognition due to their assistance they have provided for me on this journey. I would like to acknowledge and thank my dissertation advisory committee members, Drs. Alex Punnoose, Dmitri Tenne, and Kenneth McClellan for their commitment and guidance throughout this research. I would also like to thank everyone in the Advanced Materials Laboratory, both past and present. A few of the folks that I would like to specifically acknowledge for their assistance in the lab or engaging in fruitful discussions include: Gordon Alanko, Daniel Osterberg, Jennifer Watkins, Joe Croteau, Joshua Heuther, Kelci Lester, Nicole Leraas, Sumit Tamrakar, Mike Hurley, John Youngsman, and Patrick Price. Additionally, I would like to acknowledge Jatu Burns, Kerry Allahar, and Bryan Forsmann at CAES. This dissertation was also made possible with support from many people within in the college of engineering, which include: Peter Mullner, Phil Boysen, Chad Watson, Dena Ross, Brittany Archuleta, Jane Hokanson, Paul Roberston, and Karthik Chinnathambi. Acknowledgement is also due to

folks outside of the college of engineering, which include Madhu Kongora, Jodi Chilson, and Marion Lytle.

Lastly, I would like to acknowledge my family and friends for the support they have provided. My parents, Jon and Renae, have always believed in me, fostered my curiosities, and have been supportive of my pursuit of education. My in-laws, Dennis and Bonita, have provided more for me than they are aware. They allowed me to take their daughter's hand in marriage, trusted me, and supported me and my family throughout this process. Lastly, but most important, I would like to thank my wife and our three children for the support, drive, and patience that I needed to see this through the end. This journey has been challenging, but with the support of all of those listed above, has been both enjoyable and rewarding.

ABSTRACT

This dissertation presents the effects of atmosphere, time, and energy input (thermal and mechanical) on the kinetics of gas-solid and solid-solid reactions in systems of dysprosium, uranium, oxygen, and nitrogen. Accordingly, Chapter Two presents a novel synthesis technique used to form DyN via a gas-solid reaction between dysprosium and nitrogen. DyN was rapidly formed through a mechanochemical process in a high energy ball mill at ambient temperatures. The progress of the reaction was quantified using *in situ* temperature and pressure measurements coupled with microscopy and x-ray diffraction. It was found that the rate of the nitridation reaction is controlled by the creation of fresh dysprosium surfaces, which is a function of milling intensity and the number of milling media.

Chapter Three describes how UN was synthesized prior to mixing with UO_2 in the fabrication of accident tolerant nitride fuels for nuclear reactor applications. High purity and carbon free UN was synthesized using a hydride-dehydride-nitride thermal synthesis route. In order to fabricate an accident tolerant nitride fuel, it is postulated that the addition of small amounts of UO_2 (up to 10 w%) to UN will significantly increase its corrosion resistance. UN-UO_2 composite pellets were sintered in Ar-(0-1 at%) N_2 to study the effects of nitrogen concentration on the evolved phases and microstructures. Further studies were conducted where UN and UN-UO_2 composites were sintered in Ar-100 ppm N_2 for five hours at various temperatures (1700-2000 °C) and the final grain

morphologies and phase concentrations were compared. Electron micrographs showed that the oxide inclusions remained homogenously dispersed throughout the microstructure and were located on UN grain boundaries. Increasing UO_2 additions resulted in microstructural coarsening, as did the sintering temperature. Higher sintering temperatures also resulted in lower sintered densities, presumably due to a preferential formation of oxygen-stabilized nitrides or uranium oxynitrides.

The high temperature oxidation kinetics of dysprosium is presented in Chapter Four. Dysprosium particles were isothermally oxidized from 500 - 1000 °C in N_2 - (2, 20, and 50%) O_2 and Ar - 20% O_2 using simultaneous thermal analysis techniques. Two distinct oxidation regions were identified at each isothermal temperature in each oxidizing atmosphere. Initially, the oxidation kinetics are very fast until the reaction enters a slower, intermediate region of oxidation. The two regions are defined and the kinetics of each are assessed to show an apparent activation energy of 8 - 25 $^{kJ}/_{mol}$ in the initial region and 80 - 95 $^{kJ}/_{mol}$ in the intermediate oxidation reaction region. The effects of varying the oxygen partial pressure on the reaction rate constant is used to show that dysprosium oxide (Dy_2O_3) generally acts as a p-type semiconductor in both regions of oxidation (with an exception above 750 °C in the intermediate region).

TABLE OF CONTENTS

LIST OF TABLES

LIST OF FIGURES

LIST OF ABBREVIATIONS

AmN	Americium nitride
α	Reaction extent
α-U	Alpha phase uranium
Ar	Argon gas
at%	Atomic percent
atm	Atmosphere
ATF	Accident tolerant nuclear fuel
BDB	Beyond design basis
BET	Brunauer-Emmett-Teller
BPR	Ball to powder ratio
BSE	Backscattered electron
BWR	Boiling water nuclear reactor
BWREoS	Benedict-Webb-Rubin equation of state
°C	Degrees Celsius
C	Carbon
CAES	Center for Advanced Energy Studies
CR	Coefficient of restitution
DB	Design basis
dMA	Double mechanical alloying

DOE	Department of Energy
DSC	Differential scanning calorimetry
Dy	Dysprosium
Dy_2O_3	Dysprosium oxide
DyN	Dysprosium nitride
E_a	Activation energy
EBR-II	Experimental breeder reactor-II
EDS	Energy dispersive X-ray spectroscopy
eV	Electron volt
FCC	Face centered cubic
FCM	Fully ceramic microencapsulated fuel
FFTF	Fast flux test facility
GWd/t	Gigawatt-days per ton of uranium
H_2	Hydrogen gas
HCP	Hexagonal close-packed
HEBM	High energy ball milling
HRC	Rockwell hardness C
Hz	Hertz
ICPMS	Inductively coupled plasma mass spectrometer
ICDD	International Centre for Diffraction Data
ICSD	Inorganic Crystal Structure Database
J	Joule
K	Kelvin

k	Kinetics rate constant
kJ	Kilojoule
kg	Kilogram
k_p	Parabolic rate constant
kPa	Kilopascal
ktons	Kilotons
LWR	Light water nuclear reactor
M2A	Mechanically activated annealing
MA	Mechanical alloying
MASHS	Mechanically activated self-propagating high-temperature synthesis
MD	Mechanical disordering
MEMS	Micro-electromechanical systems
MG	Mechanical grinding
MM	Mechanical mixing
mMoles	Millimoles
MPa	Megapascal
MSE	Materials Science and Engineering
n	Number of moles
N	Nitrogen
N-15	Nitrogen isotope with a mass of 15 grams per mole
N_2	Nitrogen gas
NERI	Nuclear Energy Research Initiative
NEUP	Nuclear Energy University Programs

nm	Nanometer
O	Oxygen
O_2	Oxygen gas
P	Pressure
PBM	Planetary ball milling
ppm	Parts per million
ppb	Parts per billion
PSA	Particle size analysis
PSD	Particle size distribution
PVDC	Polyvinylidene chloride
RM	Reactive milling
RMM	Reactive mechanical milling
rpm	Revolutions per minute
R	Universal gas constant
R_u	Universal gas constant
SEM	Scanning electron microscopy
SiO_2	Silicon dioxide
SPEX	Shaker milling
T	Temperature
t	time
TD	Theoretical density
TGA	Thermogravimetric analysis
Torr	Torr

XRD	X-ray diffraction
U	Uranium
U_2N_3	Uranium sesquinitride
U_3O_8	Triuranium octoxide
U-235	Uranium isotope with a mass of 235 grams per mole
UC	Uranium monocarbide
UHP	Ultra high purity
µg	Microgram
µL	Microliter
µm	Micrometer
UN	Uranium mononitride
UN_{1+x}	Hyperstoichiometric uranium nitride
UO_2	Uranium dioxide
USi_x	Compound of uranium and silicon
USDOE	United States Department of Energy
V	Volume
$\bar{v}$	Molar volume
YSZ	Yttria stabilized zirconia
W	Watt
w%	Weight percent
ZrC	Zirconium carbide

CHAPTER ONE: INTRODUCTION

The work presented in this dissertation highlights research that has been accepted for publication, or published through four publications in two separate journals: the *Journal of Nuclear Materials* and the *Journal of Alloys and Compounds*. Chapter Two describes the experimental preparation of dysprosium nitride (DyN) using a mechanochemical reaction method. The research described in Chapter Two is part of a larger effort in the understanding of reactive milling (also referred to as a mechanochemical synthesis or a mechanically induced gas-solid reaction) by high energy planetary ball milling elemental dysprosium in a nitrogen atmosphere to form DyN. The mechanochemical reaction was monitored (as a function of milling intensity and time) using *in situ* temperature and pressure measurements to calculate the extent of the reaction. A more detailed kinetics study is presented on the nitridation of dysprosium in a planetary ball mill in the Appendix (also published in the *Journal of Alloys and Compounds*), where a fundamental milling dynamics model is used to describe the behavior of the RM process.

Similar to Chapter Two, Chapter Three presents a synthesis technique to produce a nitride ceramic. However, instead of using mechanical energy to cause the reaction to proceed, the reaction was induced via thermal energy. Accordingly, Chapter Three describes the preparation of uranium mononitride (UN) using a thermal synthesis technique that avoids excessive carbon impurities. The UN powder was then used in the

fabrication of UN-UO_2 (up to 10 wt% UO_2) composite pellets for sintering atmosphere and temperature studies. The research presented in Chapter Three has been accepted for publication in the *Journal of Nuclear Materials*.

Another gas-solid kinetics study is presented in Chapter Four where elemental dysprosium particles were reacted with various oxygen containing atmospheres. Dysprosium was reacted in the temperature range of 450 – 1000 °C in N_2 - (2%, 20%, and 50%) O_2 and Ar - 20% O_2 process gas streams and monitored using simultaneous thermal analysis techniques. The rate of mass change in each gas stream was used in various kinetics models to determine apparent activation energies for oxidation in two defined regions of oxidation. In order to gain further insight into the oxidation mechanisms, Kroger-Vink plots were created and an inert marker experiment was conducted on a cast dysprosium rod. The research presented in Chapter Four has also been accepted for publication in the *Journal of Alloys and Compounds*.

Each chapter presents a conclusive study but are each related by the central theme of reaction kinetics. Accordingly, a detailed introduction to each article (each kinetics study and materials system) is provided at the beginning of each individual chapter.

CHAPTER TWO: *IN SITU* CHARACTERIZATION OF THE NITRIDATION OF DYSPROSIUM DURING MECHANOCHEMICAL PROCESSING*

This chapter is published by Elsevier in *Journal of Alloys and Compounds* and should be referenced appropriately.

Reference:

B. J. Jaques, D. D. Osterberg, G. A. Alanko, S. Tamrakar, C. R. Smith, M. F. Hurley, D. P. Butt, "*In situ* characterization of the nitridation of dysprosium during mechanochemical processing." *Journal of Alloys and Compounds.* **619** 253-261 (2015).

*This chapter includes modifications from the originally published version.

In Situ Characterization of the Nitridation of Dysprosium During Mechanochemical Processing

Brian J. Jaques[a,b]

Daniel D. Osterberg[a,b]

Gordon A. Alanko[a,b]

Sumit Tamrakar[a,b]

Cole R. Smith[a,b]

Michael F. Hurley[a,b]

Darryl P. Butt[a,b]

Accepted for publication in:

Journal of Alloys and Compounds

January 2015

[a]*Department of Materials Science and Engineering, Boise State University,*

1910 University Dr., Boise, ID 83725, USA

[b]*Center for Advanced Energy Studies,*

995 University Blvd, Idaho Falls, ID 83415.

Abstract

Processing of advanced nitride ceramics traditionally requires long durations at high temperatures and, in some cases, in hazardous atmospheres. In this study, dysprosium mononitride (DyN) was rapidly formed from elemental dysprosium in a closed system at ambient temperatures. An experimental procedure was developed to quantify the progress of the nitridation reaction during mechanochemical processing in a high energy planetary ball mill (HEBM) as a function of milling time and intensity using *in situ* temperature and pressure measurements, SEM, XRD, and particle size analysis. No intermediate phases were formed. It was found that the creation of fresh dysprosium surfaces dictates the rate of the nitridation reaction, which is a function of milling intensity and the number of milling media. These results show clearly that high purity nitrides can be synthesized with short processing times at low temperatures in a closed system requiring a relatively small processing footprint.

Keywords: Nitride materials, Rare earth alloys and compounds, Gas-solid reactions, Mechanochemical processing, Inorganic materials, Ceramics

2.1 Introduction

Interest in rare earth element production and management has increased significantly in the United States (US) in the past few years. Such “strategic materials” have substantially increased the US dependence on the Republic of China, which exported 99% of the approximately $186 million worth of rare earths to the US in 2008 for use in metallurgical applications and alloys, electronics, catalysts, and cathode ray

tubes [1]. Compared to the light rare earth metals, relatively little published literature exists for praseodymium, promethium, thulium, lutetium, and dysprosium although scientific interest in these metals is on the rise. In the next forty years, Hoenderdaal *et al.* [2] project that the demand for dysprosia (Dy_2O_3) and other dysprosium compounds will increase to between 7-25 times (to 14-50 ktons) the 2010 demand. This increase in projected demand largely stems from magnetic applications in electric motors due to dysprosium's exceptional magnetic moment of 10.6 Bohr magnetrons, which is second only to holmium, and its ability to induce coercivity as an alloying agent or dopant [3]. DyN has also been investigated as a material for ferromagnetic and semiconductor superlattice structures for spintronic applications [4-6]. Dysprosium's isotopes strongly absorb neutrons and could be applied as moderator materials in nuclear reactors. Additionally, due to its physical attributes and high vapor pressure, dysprosium mononitride (DyN) has been postulated as a suitable surrogate for americium mononitride (AmN) in studying its sintering and alloying effects in spent nuclear fuel reprocessing [7-12].

Traditional synthesis routes to advanced nitride ceramics are based on thermal treatments, which can require large amounts of infrastructure, long processing times, and can introduce excessive amounts of anion impurities. High energy ball milling (HEBM) is an alternative technique that can be used to synthesize high purity nitride ceramics in relatively short times in a sealed and controlled environment, which reduces exposure to unwanted atmospheres. HEBM is used in many processes that have been described in literature: Mechanical alloying (MA), mechanical milling (MM) and mechanical grinding (MG), mechanical disordering (MD), reactive milling (RM), reactive mechanical milling

(RMM), cryomilling, mechanically activated annealing (M2A), double mechanical alloying (dMA), and mechanically activated self-propagating high-temperature synthesis (MASHS) [13, 14]. HEBM is a versatile processing technique that has been demonstrated as useful for producing nanometer-structured materials, crystalline and amorphous materials, as well as equilibrium and metastable phases [13]. A ball milling process that is considered high energy is one that utilizes high media impact velocities and large media impact frequencies to efficiently mill the powder charge. This can be accomplished in numerous ways. Most notably, dynamic mechanical energy can be delivered to a powder charge using a few different milling techniques, including: horizontal ball milling, planetary ball milling (PBM), magneto ball milling, and shaker milling (SPEX) [13-16]. Different milling apparatuses vary in capacity, efficiency of milling, and spatial arrangements requiring each to be characterized independently when attempting to understand the mechanisms of the processes.

Mechanical alloying has been used to synthesize oxide dispersion strengthened alloys since the 1960s and, approximately a decade later, the same process was shown to be useful as a ceramic synthesis method, later noted as RM [13]. For the past 40 years, RM has been investigated for the low temperature, solid state synthesis of advanced ceramics. According to Huot *et al.* [14], RM has been demonstrated on hydrogen storage materials using various milling techniques for the past 10 years, resulting in approximately one thousand publications. However, the study of RM in the synthesis of non-oxide and non-hydride materials has not been studied as extensively; there are fewer than 50 publications on the use of RM to form nitrides and fewer than 20 that used PBM. The limited number of studies that focused on producing nitride ceramics tended to

investigate transition metals and class IIIA elements such as: Al, B, Cr, Fe, Ga, Nb, Si, Ta, Ti, V, and Zr [13, 17-33]. To the best of the authors' knowledge, the synthesis of lanthanide or actinide nitrides via RM has not been published other than the earlier work of this group [7-10]. In particular, to study nitridation reaction kinetics during RM in a PBM using *in situ* temperature and pressure data is very limited; there are no studies found in the literature on RM in a PBM to form nitrides with *in situ* temperature and pressure measuring capabilities. The only studies found that have demonstrated such capabilities during PBM are limited and stem from the research on hydrogen storage materials [34-40].

The work described here is part of a larger effort in the understanding of RM (also referred to as a mechanochemical synthesis or a mechanically induced gas-solid reaction) by high energy planetary ball milling elemental dysprosium in a nitrogen atmosphere to form dysprosium mononitride (DyN), as follows:

$$Dy + \frac{1}{2}N_2 \rightarrow DyN \quad (1)$$

The mechanochemical reaction was monitored (as a function of milling intensity and time) using *in situ* temperature and pressure measurements to calculate the extent of the reaction. A more detailed kinetics study is presented on the nitridation of dysprosium in a PBM in our concurrent publication [41], where a fundamental milling dynamics model is used to describe the behavior of the RM process.

2.2 Experimental Details

To study the RM during PBM of the nitridation reaction, milling experiments were performed in ultra-high purity (UHP) nitrogen with high purity dysprosium filings (99.9% purity, ESPI) sieved through a 40 mesh (420 μm) sieve (Figure 2.1). The filings

had a surface area of 0.196 ± 0.058 m^2g^{-1}, as determined by nitrogen adsorption Brunauer-Emmett-Teller (BET) techniques. In order to gain insight into the reaction kinetics, the internal temperature and pressure of the milling vessel were monitored during milling in a Retsch planetary ball mill (PM100) at milling intensities varying from 350 – 650 rpm. Each milling run was completed using a Retsch 250 mL hardened steel milling vessel (85Fe, 12Cr, 2.2C, 0.45Mn, 0.4Si) and 5 mm diameter, spherical yttria stabilized zirconia media (Tosoh, Tokyo, Japan). According to the respective vendors, the milling vessel and milling media had a hardness of 62 HRC and 72 HRC, respectively. The ball to powder ratio (BPR) was held constant at 14:1 with a total dysprosium mass of 5 grams (70 grams of YSZ media, which equates to 184 spheres). The temperature and pressure were monitored using a Retsch sensing lid (PM GrindControl), which has capabilities of 273 – 473 K, 0 – 500 kPa, and can wirelessly send data at 200 Hz to a remote computer. The temperature (measured by a thermistor) and pressure sensors are integrated into recessed locations in the steel sensing lid.

During each run, the milling vessels were loaded with media and dysprosium and sealed with the temperature and pressure monitoring lid in an argon atmosphere glovebox. It was then charged to approximately 450 kPa with oxygen-gettered UHP nitrogen (oxygen content less than 0.1 ppb as measured by a Neutronics OA-1 oxygen analyzer). The vessel was charged to 450 kPa and relieved (3 cycles) prior to a final charge of 450 kPa in order to ensure a pure nitrogen milling atmosphere.

The stages of the milling process were observed through mass measurements, SEM imaging, and powder X-ray diffraction (XRD) during a 500 rpm milling run. The 500 rpm milling run was periodically interrupted between 0 – 6 hours of milling. Each

time the process was halted, the milling vessel was transferred into an argon atmosphere glovebox where the lid was removed and the measurements or representative powders were taken. The same powder and media was then sealed, evacuated and charged with nitrogen, and secured to the mill for subsequent milling.

The effect of milling intensity was assessed by milling for 6 hours at different intensities from 350 – 650 rpm. After milling, the powder was separated from the milling media in the argon-filled glovebox and characterized using SEM imaging, laser-scattering particle size analysis (PSA), and XRD. Additionally, temperature and pressure data were used to assess the reaction kinetics at each milling intensity.

In each case, XRD was performed at room temperature on a Bruker D8 Discover using Cu-K_α radiation ($\lambda = 0.15418$ nm). However, some of the patterns were collected with a scintillation counter and some were collected with a 2-dimensional area detector. Due to the oxygen sensitivity of the material, the XRD samples were prepared in an argon glovebox and a semi- X-ray transparent film was placed over the powder filled sample holders in order to prevent oxidation during the XRD scans.

The particle morphology after 6 hours of milling at 350 – 650 rpm was investigated using a Hitachi (S-3400N) thermionic cathode scanning electron microscope (SEM) as well as a Horiba (LA-950) laser scattering particle size analyzer (PSA). The powders were first adhered to carbon tape prior to carbon coating in order to obtain SEM images with reduced electron charging. For PSA, the DyN powders were dispersed in an isoparaffinic fluid (Isopar V, ExxonMobil) by external ultrasonication using a 750 W sonication probe prior to loading into the mixing chamber of the Horiba analyzer. The

refractive indices used for the free powder and the Isopar V were 2.5-0.43i and 1.452, respectively.

2.3 Results

Typical *in situ* temperature and pressure data (collected at 0.2 Hz) from milling dysprosium with a BPR of 14:1 at 500 rpm in UHP nitrogen is shown in Figure 2.2. It is seen that the rate of change of both temperature and pressure reach a steady state after approximately 2.5 hours. An 8 kPa increase in the pressure was observed immediately upon starting the mill. The pressure peaked at 22 kPa above the initial pressure before decreasing and reaching a steady state decay rate (the constant decay is attributed to a slow leak in the seal between the milling vessel and sensing lid). Figure 2.2 also shows systematic effects of the milling process on the temperature and pressure in the vessel when the mill is turned off (after 6 hours of milling). The pressure immediately drops 6 kPa and decays another 8 kPa between 0 – 9 minutes after stopping the mill. Additionally, as soon as the mill turns off, the temperature decreases by 1.1 K before increasing 0.6 K and then cooling to room temperature.

The temperature and pressure data was then used to calculate the amount of nitrogen consumed throughout the RM process (as shown in the inset of Figure 2.2) using the ideal gas law:

$$n = \frac{PV}{RT} \tag{2}$$

where n is the number of moles of nitrogen gas consumed, P is the pressure, V is the volume of free space in the milling vessel, R is the ideal gas constant, and T is the temperature of the vessel. After approximately 1.5 hours of milling, the nitrogen consumption rate significantly slows, reaching steady state (with a slight leak) after

approximately 2.5 hours. As described above, the effects of the milling process (when starting and ending the mill) on the temperature and pressure directly translate into the nitrogen consumption plot.

To better understand the distribution and morphology of the products and reactants as a function of RM time, a 500 rpm milling run, similar to that shown in Figure 2.2, was periodically interrupted and the location of the powder within the mill was quantified. The bar chart in Figure 2.3 shows the distribution of dysprosium within the milling vessel. Initially, all of the powder was of course free dysprosium filings. After ten minutes of milling, approximately 30% of the dysprosium was cold welded to the media and the walls of the milling vessel. Following an additional 50 minutes, nearly 85% of the initial powder mass was recovered as free powder with the remainder still cold welded to the walls of the vessel. After 180 minutes of milling at 500 rpm, all of the dysprosium could be recovered as free powder within the milling vessel. In each case, the free powder was imaged using SEM (Figure 2.4) and was characterized for phase distribution by XRD (Figure 2.5). From the SEM images, it was seen that the free powder morphology changed with increased milling time from a large plate-like morphology to more uniform particles to a bimodal particle size after long milling times. As one might expect, XRD showed a transition from the hexagonal closed-pack (HCP) structure of dysprosium to the face-centered cubic (FCC) structure of DyN with increased milling time (Figure 2.5). The diffraction intensity of the free powder after 30 minutes was very weak and an unidentified peak appears. However, after approximately 60 minutes, the HCP diffraction pattern caused by the elemental dysprosium diminishes and the FCC diffraction pattern of DyN dominates. However, it is worth noting that the XRD is

performed on only the free powder obtained from the milling vessel and therefore the nitride conversion via XRD overestimates the actual conversion of the dysprosium charge (which is due to material (primarily elemental dysprosium) that is cold welded to the vessel walls, as depicted in Figure 2.3). As milling time was increased, there exists a slight shift in the lattice parameters, but no new phases appear to have formed.

The effect of milling intensity on the rate of nitrogen consumption after milling 5 grams of dysprosium for 6 hours is shown in Figure 2.6. As previously described, the nitrogen consumption was calculated using the ideal gas law. However, the plot was generated after three distinct steps were completed to post process the acquired temperature and pressure data to allow for better comparison between milling runs: first, a constant leak rate was subtracted from the pressure data, second, a shift was applied to the nitrogen consumption data, and third, the nitrogen consumption was normalized to the maximum amount of consumed nitrogen for each run. The leak rate between the milling vessel and the lid was determined by finding a linear fit to the constant nitrogen consumption rate (as noted above). The leak rates were determined after the mill was halted (in the 8 – 10 hour range, when the temperature had equilibrated) and were determined to be between 0.02 – 0.09 mMoles N_2 hr^{-1} for all milling runs. The shift of the nitrogen consumption data was to account for the effects of the milling process (described above) and was a simple positive linear shift to set the minimum nitrogen consumption value equal to zero (see the inset in Figure 2.2). It is worth noting that the shift increased with milling intensity from 0.598 mMoles of N_2 at 350 rpm to 1.8 mMoles of N_2 at 650 rpm, which is 4 – 12% of the total theoretical nitrogen consumption in the nitridation reaction shown in Equation 1. The third fitting step was to normalize the

reaction extent in each milling run. This was completed by normalizing nitrogen consumption to the maximum apparent nitrogen consumption for each milling run, which was 92 ± 5% of the theoretical nitrogen consumption.

The effect of milling intensity on the resultant phase(s) of the free powder is shown in the XRD patterns in Figure 2.7. From this figure, it appears to take longer than 6 hours of milling at 350 rpm to complete the dysprosium to DyN reaction, as evidenced by minor elemental HCP dysprosium peaks in the diffraction pattern. However, the reaction appeared to have reached completion at all greater milling intensities and a secondary, unidentified phase begins to appear after 6 hours of milling at 575 rpm.

The effect of milling intensity on the resultant powder morphology of the free powder is shown in the PSA and SEM images of Figure 2.8. The volume-based particle size distribution plots of powders from each milling intensity are slightly bi-modal. There exists a mode at approximately 0.2 μm with a small volume fraction of powder but the mode at 2.6 μm dominates and contains a majority of the volume of the powder. All of the particles appeared to be less than 11 μm in size. Additionally, the powder retrieved from the 650 rpm milling run had a narrower particle size distribution but is still centered at 2.6 μm. The SEM images show more irregular particle morphologies as the milling intensity is increased.

2.4 Discussion

For the first time reported in literature, the rate of a nitridation reaction through RM in a PBM has been observed via *in situ* temperature and pressure measurements. Furthermore, RM in a PBM to form a lanthanide nitride has never been published other than previous work of this group [7-10]. Of other authors that have presented *in situ*

pressure and temperature data, the ideal gas law was used to quantify the gas consumption in the milling vessel presumably because it is a robust and simple equation that is assumed to be valid with reasonable accuracies at the milling temperatures and pressures investigated [35, 37, 38, 40, 42]. To be consistent with literature, the ideal gas law was also used for the work presented here. However, Çengel and Boles [43] predict that the Benedict-Webb-Rubin equation of state (BWREoS) will have a 0.0% associated error at 200-300 K and 200-1000 kPa, similar to the parameters of the studies presented here. The BWREoS, which has 8 empirical constants, is derived from virial equations to the following equation:

$$P = \frac{R_u T}{\bar{v}} + \left(B_0 R_u T - A_0 - \frac{C_0}{T^2}\right)\frac{1}{\bar{v}} + \frac{bR_u T - a}{\bar{v}^3} + \frac{a\alpha}{\bar{v}^6} + \frac{c}{\bar{v}^3 T^2}\left(1 + \frac{\gamma}{\bar{v}^2}\right) e^{-\gamma/\bar{v}^2} \quad (3)$$

where the P is pressure, R_u is the universal gas constant, T is the temperature, $\bar{v}$ is the molar volume, and the other variables are predetermined empirical constants specific to nitrogen, as defined in Table 2.1 [43].

When the two equations of state are applied to the *in situ* temperature and pressure data from the PBM of dysprosium, a vertical shift in the calculated nitrogen consumption was observed. The maximum vertical shift, shown in Figure 2.9 for a milling intensity of 500 rpm, increases nearly linearly with milling intensity and in each case, the BWREoS predicts a greater nitrogen consumption rate than does the ideal gas law, as shown in Table 2.2.

Table 2.2 shows the time within each milling intensity that a maximum error is observed resulting from using the BWREoS versus the ideal gas law. The error is calculated as the difference between values predicted by each equation of state relative to the maximum theoretical nitrogen consumption of 5 grams of dysprosium, which is

15.4 mMoles of N_2. Table 2.2 also shows the time at which the maximum nitrogen consumption rate is observed for each milling intensity, which was found using the first derivative of the consumption data calculated using the ideal gas law. A nearly linear relationship was observed between the milling intensity, the maximum observed error, and the time where the maximum error was observed. The observations presented here suggest that the ideal gas law tends to underestimate the amount of nitrogen consumed during RM by 2 – 3%. However, when considering reaction rates, the first derivative of the moles consumed versus time is the primary factor and small linear shifts of the amount of moles consumed due to the equation of state calculations (within the temperature range observed) are inconsequential.

The peculiar temperature and pressure behavior that is observed at the beginning of the milling process (Figure 2.2), which also becomes more pronounced with milling intensity, was observed by a few authors studying the hydrogenation of magnesium and magnesium alloys [14, 35-37]. In this prior work, the temperature increase during the first 30 minutes of milling was attributed to the "mechanical action" of the mill. The initial behavior of pressure was attributed to an "incubation period," where a critical number of defects are created before the dissociation of H_2 and subsequent diffusion into the bulk magnesium can occur (marked by the onset of decreasing pressure). Doppiu *et al.* [36] present traces at hydrogen pressures ranging from 1 – 8 MPa that show a significant decrease in the "incubation period" and increase in the hydrogen absorption rate with increasing initial hydrogen pressure. The authors proposed two regions of hydrogen uptake: hydrogen absorption and nucleation of the hydride phase, with the latter of the two being much slower and only happening after a significant amount of hydrogen is

absorbed and dissolved into the magnesium. However, in the case of rare earth elements, the tendency for nitrogen dissolution is low and it has been shown that diatomic nitrogen will preferentially dissociatively chemisorb on clean dysprosium surfaces at 300 K rather than be adsorbed and subsequently dissolved into the metal [44]. It is therefore postulated that as fresh surface is created through the milling process, nitrogen will spontaneously dissociate on the dysprosium surfaces. Since it is thought that the dissolution of nitrogen in dysprosium is low, it will nearly instantaneously form DyN at a rate that is directly proportional to the creation of fresh, clean surfaces (which is a dependent on the number of media, the media impact frequency, and the media impact energy) and is further described and modeled in our concurrent publication [41]. This is a concept also discussed by Bab *et al*. [42] in the nitridation of hafnium in a vibratory mill.

To better understand the influence of the milling process on the apparent nitrogen consumption behavior, the effects observed in temperature and pressure traces during the early stages of RM were investigated. The first experiment to sort out discrepancies in the early stages of the milling process was to better understand the lag in sensing between the temperature and pressure monitors. It is assumed that a large fraction of the heat input into the milling vessel is contributed by the electrical motor and the mill itself via conduction through the bottom of the milling vessel where the mill and the vessel were in contact. Accordingly, a milling vessel that was loaded, sealed, and pressurized was placed on a hot plate preheated to 332 K while temperature and pressure data were recorded with the sensor lid. The resultant data from the sensing lid is shown in Figure 2.10 (the apparent change in nitrogen content is shown in the inset and was calculated using the ideal gas law).

The temperature sensed at the top of the vessel (where the temperature sensor is located) reached an equilibrium in 2.5 hours at a temperature of 314 K, or 18 K cooler than that of the heat source. Once the temperature and pressure were both near equilibrium, the vessel was removed from the heat source and placed on an insulated bench at room temperature, where it took an additional 4.5 hours to cool back to room temperature. From the collected data, a 5 minute lag was observed in the temperature reading compared to the pressure reading even under static conditions. The temperature discrepancy between the source and the sensor is presumed to be due to natural convective losses to the surrounding environment causing a temperature gradient from the heat source at the bottom of the vessel to the temperature sensor at the top of the vessel. Additionally, by assuming the heat source is at the bottom of the vessel and that the convection is the main source of heat loss resulting in a temperature gradient, it is reasonable to assume that the temperature gradient will increase with milling intensity. As the mill is rotating faster, a higher flow of air is passed over the milling vessel and convective cooling becomes more prominent. In any case, it is presumed that the temperature of the atmosphere within the milling vessel is at an intermediate temperature value that falls between the value at the heat source and that of the sensor.

The rise in pressure during the constant heat source experiment is the result of gas expansion with increasing temperature in a constant volume. The discrepancy in temperature (as described above and shown in the inset of Figure 2.10) between the mean temperature of the vessel and that measured by the sensor in the milling lid results in an apparent consumption of nitrogen, as calculated by the ideal gas law. This apparent

nitrogen consumption was solely the effect of non-equilibrium conditions (temperature) within the vessel.

To quantify the relative contributions of the mill, milling media impacts, and mechanical deformation of dysprosium to the heat generation measured by the pressure and temperature sensors, the milling process was duplicated with and without milling media and dysprosium. The results are shown in Table 2.3, with the error determined from the standard deviation of at least 3 milling runs. When a sealed vessel was milled with no media and no dysprosium, the average temperature and pressure increases were 11 K and 1 kPa, respectively. The temperature and pressure both increased with the addition of milling media and again with addition of dysprosium. The data collected with the YSZ media and the 5 grams of dysprosium to create the 18 K and 22 kPa increases in temperature and pressure are seen in Figure 2.2.

From these experiments, it was found that approximately 61% of the heat measured during milling is due to the mill itself balanced with the heat dissipation by convection and conduction during the milling process. The addition of media alone causes an additional 31% increase, and the addition of dysprosium to the milling process accounts for only the remaining 8% of the measured heat generation, or a statistical increase of approximately 1.5 K when 5 grams of dysprosium is added to the milling vessel. The additional heat increase from the addition of dysprosium can be explained by a decrease in coefficient of restitution of the milling media as dysprosium cold welds to the media and vessel walls in the early stages of milling, as shown in Figure 2.3 (a concept that is more thoroughly explained and modeled in a concurrent publication [41]). As the coefficient of restitution of the milling media decreases, it suggests that collisions

become less elastic and result in greater energy transfer to the milling vessel during media impact events, further increasing the temperature measured. These results indicate that, contrary to publications on hydrogenation of metals, most of the pressure and temperature increase at the beginning of a milling run may be attributed to the mill itself along with heat dissipation from milling media rather than any specific “mechanical action” on the milled material.

2.5 Conclusions

An experimental method has been developed and implemented to quantitatively assess the *in situ* nitrogen consumption during RM elemental dysprosium in a PBM to form DyN at ambient temperatures. To the best of the authors’ knowledge, *in situ* nitrogen consumption in a PBM has not been presented for *any* element in the literature to date, although there are publications that have used *in situ* monitoring to study hydrogen uptake in the synthesis of hydrogen storage materials in a PBM. This study presents an understanding of the effects of the mill on the apparent rate of nitrogen consumption at the beginning and end of the milling cycle to allow future researchers to deduce these effects from the RM process. The Dy-N system is a model system to develop an understanding of RM in a PBM due to the fact that no intermediate phases are known to exist in the Dy-N system other than stoichiometric DyN. However, the lack of thermodynamic data available in the literature for the Dy-N system complicates the assessment. From the work presented here and our concurrent publication [41], it is presumed that the rate of the nitridation reaction of dysprosium is limited by the creation of fresh, reactive surfaces that catalyze the dissociation of diatomic nitrogen and allow for the spontaneous formation of DyN. The rate of creation of such fresh surfaces can be

controlled by the milling intensity or the number of media, which are both related to the number of impacts per unit time.

The results of this investigation demonstrate that advanced nitride ceramics, which traditionally require long durations at high temperatures in hazardous atmospheres, can be synthesized in short times, at low temperatures, and in a closed system. This scalable process produces a final product that has a homogenous and fine microstructure that can be easily shaped and consolidated using conventional sintering processes.

Acknowledgements

This work was partially funded through a Nuclear Energy Research Initiative contract (NERI – DE-FC07 – 05ID14650).

Author Justification

The research presented in this publication was carried out by Brian Jaques, Daniel Osterberg, Dr. Gordon Alanko, Sumit Tamrakar, Cole Smith, Dr. Michael Hurley, and Dr. Darryl Butt. Brian coordinated much of the experimental work, collected experimental data, and authored the manuscript. Much of the experimental work was completed by Daniel under the direction of Brian, Dr. Hurley and Dr. Butt. Sumit and Cole both contributed to foundational studies as well as particle size analysis. Dr. Alanko contributed additional experimental data. Dr. Alanko, Dr. Hurley, and Dr. Butt contributed fruitful discussions and ideas. Work done by Brian Jaques was in partial fulfillment of the requirements for a Doctoral degree in Materials Science and Engineering at Boise State University, under the advisement and supervision of Dr. Darryl Butt. Dr. Butt contributed greatly in terms vision, ideas, advisement, critical review of the article throughout the writing process, and financial support.

References

[1] J.S. Thomason, R.J. Atwell, Y. Bajraktari, J.P. Bell, D.S. Barnett, N.S.J. Karvonides, M.F. Niles, E.L. Schwartz, From national defense stockpile (NDS) to strategic materials security program (SMSP): evidence and analytic support, in, Institute for Defense Analysis, 2010.

[2] S. Hoenderdaal, L.T. Espinoza, F. Marscheider-Weidemann, W. Graus, Can a dysprosium shortage threaten green energy technologies?, Energy, 49 (2013) 344-355.

[3] B.T. Kilbourn, A Lanthanide Lanthology: Part I, A-L, Molycorp, Inc., Fairfield, NJ USA, 1993.

[4] Y.K. Zhou, M.S. Kim, N. Teraguchi, A. Suzuki, Y. Nanishi, H. Asahi, Optical and magnetic properties of the DyN/GaN superlattice, Phys. Status Solidi B-Basic Res., 240 (2003) 440-442.

[5] T.B. Thiede, M. Krasnopolski, A.P. Milanov, T. de los Arcos, A. Ney, H.W. Becker, D. Rogalla, J. Winter, A. Devi, R.A. Fischeri, Evaluation of Homoleptic Guanidinate and Amidinate Complexes of Gadolinium and Dysprosium for MOCVD of Rare-Earth Nitride Thin Films, Chem. Mat., 23 (2011) 1430-1440.

[6] X.J. Li, Y.K. Zhou, M. Kim, S. Kimura, N. Teraguchi, S. Emura, S. Hasegawa, H. Asahi, Magnetic and transport properties of ferromagnetic semiconductor GaDyN thin film, Chin. Phys. Lett., 22 (2005) 463-465.

[7] D.P. Butt, B.J. Jaques, D.D. Osterberg, B.M. Marx, P.G. Callahan, A.S. Hamdy, New routes to lanthanide and actinide nitrides, in: GLOBAL 2009: The Nuclear Fuel Cylcle: Sustainable Options and Industrial Perspectives, September 6, 2009 - September 11, 2009, Paris, France, 2009.

[8] B. Jaques, D.P. Butt, B.M. Marx, A.S. Hamdy, D. Osterberg, G. Balfour, Synthesis and characterization of actinide nitrides, in: GLOBAL 2007: Advanced Nuclear Fuel Cycles and Systems, September 9, 2007 - September 13, 2007, American Nuclear Society, Boise, ID, United states, 2007, pp. 591-596.

[9] B.J. Jaques, B.M. Marx, A.S. Hamdy, D.P. Butt, Synthesis of Uranium Nitride by a Mechanically Induced Gas-Solid Reaction, Journal of Nuclear Materials, 381 (2008) 309.311.

[10] P.G. Callahan, B.J. Jaques, B.M. Marx, A.S. Hamdy, D.P. Butt, Synthesis of Dysprosium and Cerium Nitrides by a Mechanically Induced Gas-Solid Reaction, Journal of Nuclear Materials, 392 (2009) 121-124.

[11] M. Takano, A. Itoh, M. Akabori, K. Minato, Hydrolysis reactions of rare-earth and americium mononitrides, Journal of Physics and Chemistry of Solids, 66 (2005) 697-700.

[12] M. Takano, S. Tagami, K. Minato, T. Kozaki, S. Sato, Lattice thermal expansions of (Dy, Zr)N solid solutions, Journal of Alloys and Compounds, 439 (2007) 215-220.

[13] C. Suryanarayana, Mechanical alloying and milling, Progress in Materials Science, 46 (2001) 1-184.

[14] J. Huot, D.B. Ravnsbæk, J. Zhang, F. Cuevas, M. Latroche, T.R. Jensen, Mechanochemical synthesis of hydrogen storage materials, Progress in Materials Science, 58 (2013) 30-75.

[15] P. Baláz, Mechanochemistry in nanoscience and minerals engineering, in, Springer, Berlin; London, 2008.

[16] A. Calka, J.I. Nikolov, Direct synthesis of AlN and Al-AlN composites by room temperature magneto ball milling: the effect of milling condition on formation of nanostructures, Nanostructured Materials, 6 (1995) 409-412.

[17] L. Liu, L. Lu, L. Chen, Y. Qin, L.D. Zhang, Solid-gas reactions driven by mechanical alloying of niobium and tantalum in nitrogen, Metall. Mater. Trans. A-Phys. Metall. Mater. Sci., 30 (1999) 1097-1100.

[18] Y. Chen, C.P. Li, H. Chen, Y.J. Chen, One-dimensional nanomaterials synthesized using high-energy ball milling and annealing process, Sci. Technol. Adv. Mater., 7 (2006) 839-846.

[19] Y. Chen, J. Fitz Gerald, J.S. Williams, S. Bulcock, Synthesis of boron nitride nanotubes at low temperatures using reactive ball milling, Chemical Physics Letters, 299 (1999) 260.

[20] Y. Chen, T. Halstead, J.S. Williams, Influence of milling temperature and atmosphere on the synthesis of iron nitrides by ball milling, Materials Science and Engineering A (Structural Materials: Properties, Microstructure and Processing), 206 (1996) 24-29.

[21] J.F. Sun, M.Z. Wang, Y.C. Zhao, X.P. Li, B.Y. Liang, Synthesis of titanium nitride powders by reactive ball milling of titanium and urea, Journal of Alloys and Compounds, 482 (2009) L29-L31.

[22] J.F. Sun, X.P. Li, B.Y. Liang, Y.C. Zhao, M.Z. Wang, Study on reaction mechanism of reactive ball milling of Ti with urea to prepare TiN powder, Journal of Inorganic Materials, 24 (2009) 759-763.

[23] M.S. El-Eskandarany, A.H. Ashour, Mechanically induced gas-solid reaction for the synthesis of nanocrystalline ZrN powders and their subsequent consolidations, Journal of Alloys and Compounds, 313 (2000) 224-234.

[24] F.J. Gotor, M.D. Alcala, C. Real, J.M. Criado, Combustion synthesis of TiN induced by high-energy ball milling of Ti under nitrogen atmosphere, Journal of Materials Research, 17 (2002) 1655-1663.

[25] C. Real, M.A. Roldan, M.D. Alcala, A. Ortega, Synthesis of nanocrystalline chromium nitride powder by mechanical processing, Journal of the American Ceramic Society, 90 (2007) 3085-3090.

[26] M.A. Roldan, V. Lopez-Flores, M.D. Alcala, A. Ortega, C. Real, Mechanochemical synthesis of vanadium nitride, Journal of the European Ceramic Society, 30 (2010) 2099-2107.

[27] Y. Qin, L. Liu, L. Chen, Characterization of nanocrystalline tantalum nitride formed by solid-gas reaction during mechanical alloying, Journal of Alloys and Compounds, 269 (1998) 238-240.

[28] J.I. Nikolov, J.S. Williams, D.J. Llewellyn, A. Calka, Phase evolution during ball milling of Al in NH_3 and subsequent annealing, in, Mater. Res. Soc, Warrendale, PA, USA, 1998, pp. 649-654.

[29] P.-Y. Lee, C.-K. Lin, C.-L. Chang, Y. Hwu, T.-S. Chin, Preparation of Iron nitride powders through mechanical alloying and atmospheric heat treatment, in, IEEE, Kyongju, South Korea, 1999, pp. 13.

[30] M. Lee, S. Endoh, H. Iwata, Basic study on the solid-state nitriding of aluminum by mechanical alloying using a planetary ball mill, Advanced Powder Technology, 8 (1997) 291-299.

[31] Q. Yuan, Y. Zheng, H. Yu, Synthesis of nanocrystalline Ti(C,N) powders by mechanical alloying and influence of alloying elements on the reaction, International Journal of Refractory Metals and Hard Materials, 27 (2009) 121-125.

[32] J.Y. Kano, E. Kobayashi, W. Tongamp, F. Saito, Preparation of GaN powder by mechanochemical reaction between Ga_2O_3 and Li_3N, Journal of Alloys and Compounds, 464 (2008) 337-339.

[33] Y. Kameshima, M. Irie, A. Yasumori, K. Okada, Mechanochemical effect on low temperature synthesis of AlN by direct nitridation method, in: 15th International Symposium on the Reactivity of Solids (ISRS), 9-13 Nov. 2003, Elsevier, Netherlands, 2004, pp. 185-190.

[34] J. Trapp, B. Kieback, Solid-state reactions during high-energy milling of mixed powders, Acta Materialia, 61 (2013) 310-320.

[35] J.X. Zhang, F. Cuevas, W. Zaidi, J.P. Bonnet, L. Aymard, J.L. Bobet, M. Latroche, Highlighting of a Single Reaction Path during Reactive Ball Milling of Mg and

TM by Quantitative H-2 Gas Sorption Analysis To Form Ternary Complex Hydrides (TM = Fe, Co, Ni), J. Phys. Chem. C, 115 (2011) 4971-4979.

[36] S. Doppiu, L. Schultz, O. Gutfleisch, In situ pressure and temperature monitoring during the conversion of Mg into MgH_2 by high-pressure reactive ball milling, Journal of Alloys and Compounds, 427 (2007) 204-208.

[37] S. Deledda, B.C. Hauback, The formation mechanism and structural characterization of the mixed transition-metal complex hydride $Mg_2(FeH_6)_{0.5}(CoH_5)_{0.5}$ obtained by reactive milling, Nanotechnology, 20 (2009) 204010 (204017 pp.).

[38] S. Deledda, B.C. Hauback, Hydride formation in Mg-based systems processed by reactive milling, Faraday Discussions, 151 (2011) 315-326.

[39] Z. Junxian, M.A. Pilette, F. Cuevas, T. Charpentier, F. Mauri, M. Latroche, X-ray Diffraction and NMR Studies of Na_3-nLi_n AlH_6 (n = 0, 1, 2) Alanates Synthesized by High-Pressure Reactive Ball Milling, J. Phys. Chem. C, 113 (2009) 21242-21252.

[40] F. Cuevas, D. Korablov, M. Latroche, Synthesis, structural and hydrogenation properties of Mg-rich MgH_2-TiH_2 nanocomposites prepared by reactive ball milling under hydrogen gas, Physical Chemistry Chemical Physics, 14 (2012) 1200-1211.

[41] G.A. Alanko, D.D. Osterberg, B.J. Jaques, M.F. Hurley, D.P. Butt, Kinetics of the Reactive Milling of Dysprosium Nitride, Journal of Alloys and Compounds, Accepted (2014).

[42] M.A. Bab, L. Mendoza-Zelis, L.C. Damonte, Nanocrystalline HfN produced by mechanical milling: Kinetic aspects, Acta Materialia, 49 (2001) 4205-4213.

[43] Y.A. Çengel, M.A. Boles, Thermodynamics: an engineering approach, McGraw-Hill, Boston, 2002.

[44] J.A. Schreifels, J.E. Deffeyes, L.D. Neff, J.M. White, An X-ray photo-electron spectroscopic study of the adsorption of N_2, NH_3, NO, AND N_2O on dysprosium, Journal of Electron Spectroscopy and Related Phenomena, 25 (1982) 191-209.

Figures

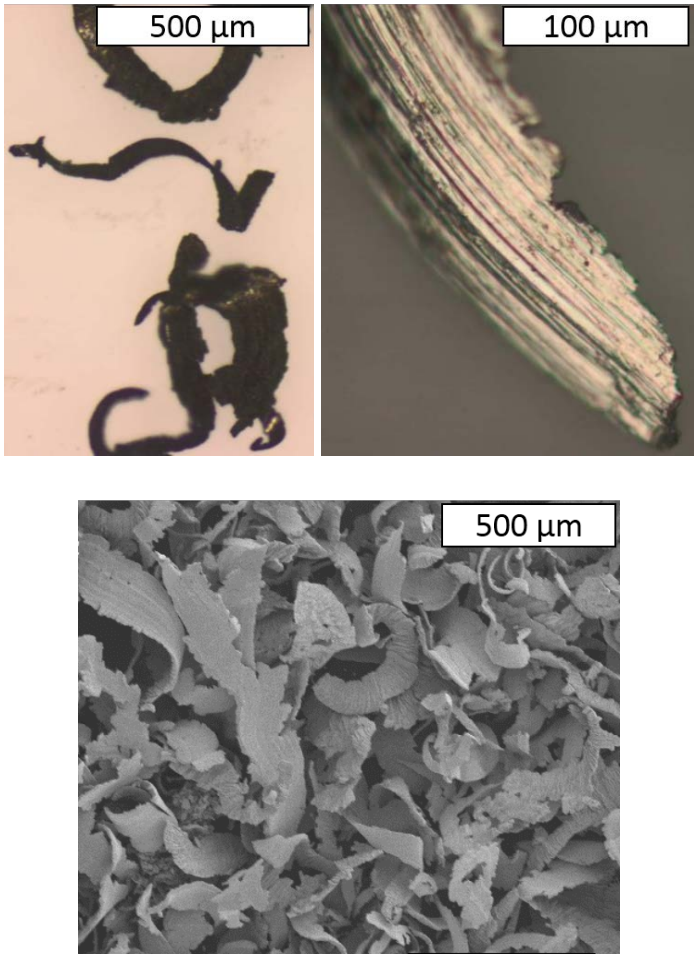

Figure 2.1 Images of the dysprosium filings used as the starting materials for the kinetics study of the nitridation reaction to form DyN using a dry planetary ball milling process in nitrogen atmosphere. The filings have a surface area of 0.196 ± 0.058 m^2/g.

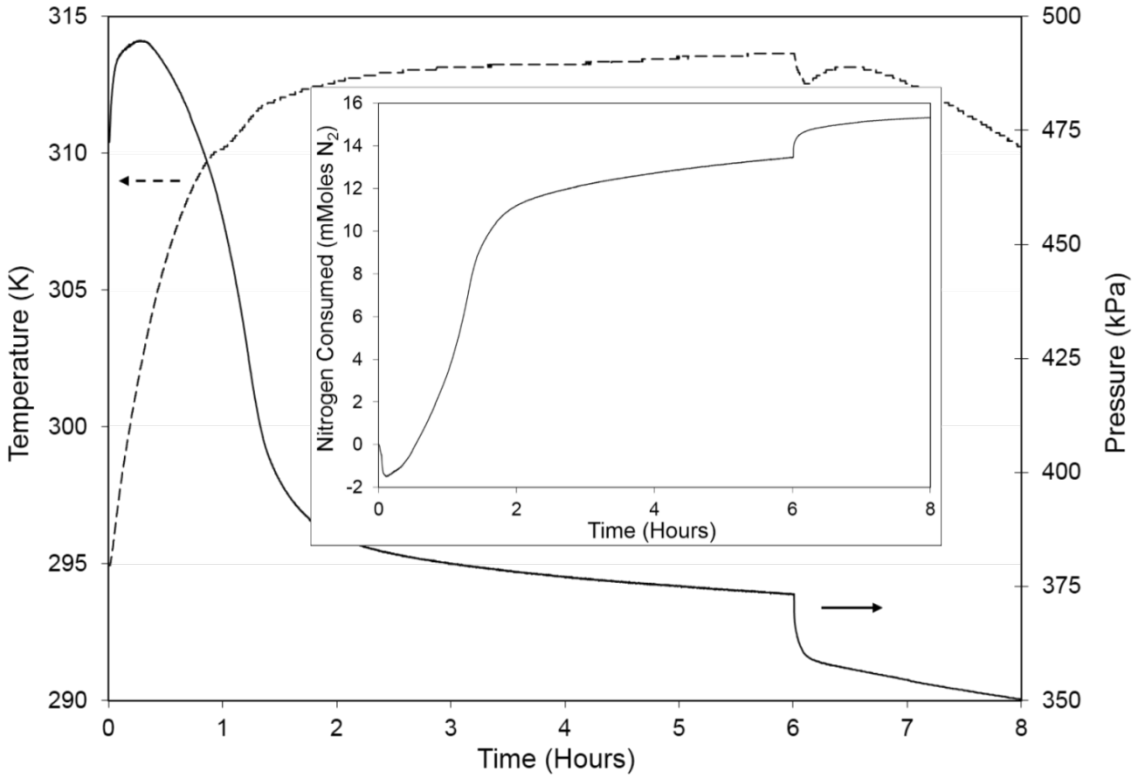

Figure 2.2 Typical temperature and pressure data as recorded *in situ* (0.2 Hz) throughout the reactive ball milling of five grams of elemental dysprosium in dry nitrogen to form DyN at 500 rpm and a BPR of 14:1. The mill was shut off after 6 hours of milling. The inset shows the nitrogen consumption calculated using the *in situ* temperature and pressure data in the ideal gas law.

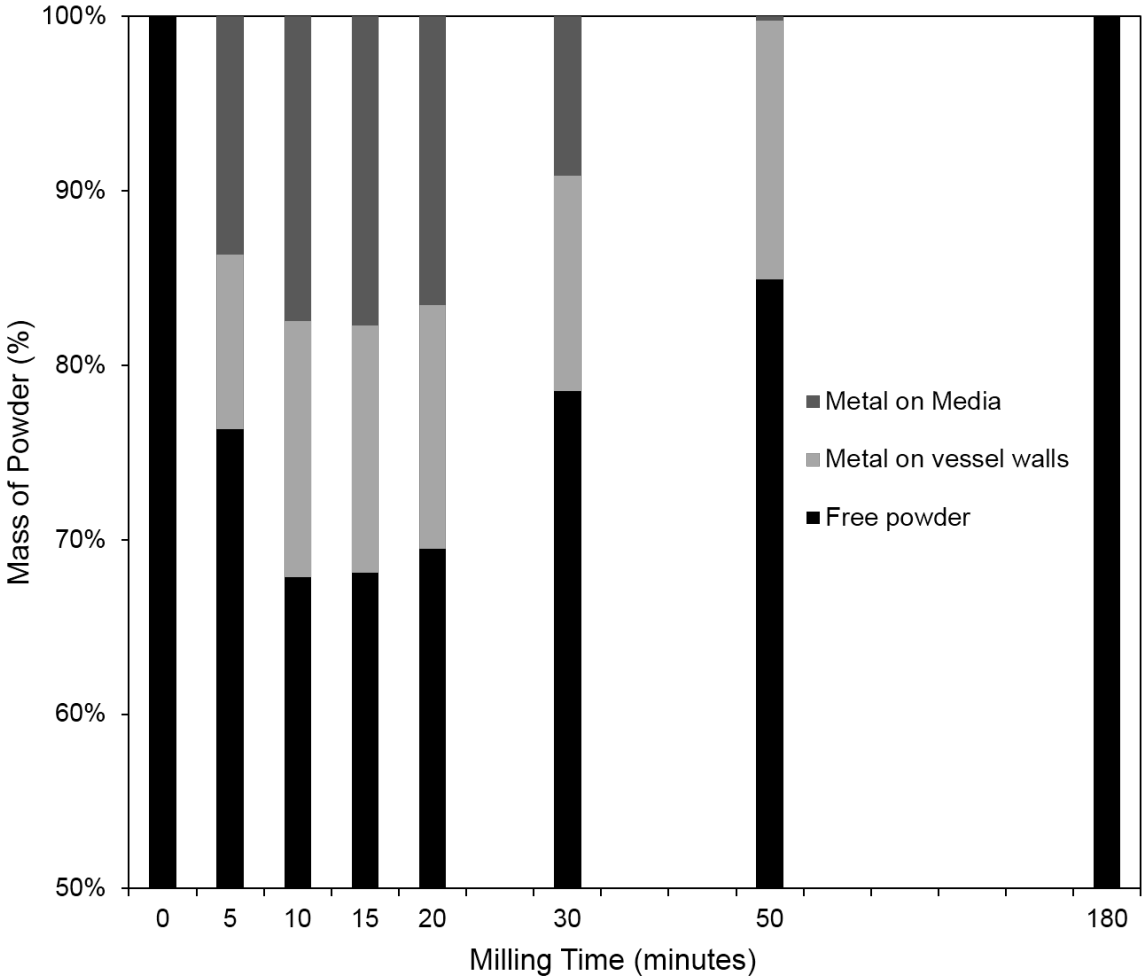

Figure 2.3 Bar chart showing the distribution of dysprosium with time throughout planetary ball milling in dry nitrogen at 500 rpm. It is seen that the dysprosium initially "cold welds" to the vessel walls and milling media but after 50 minutes, nearly 85% of the original mass is recovered and after 180 minutes, all of the powder is free from the vessel walls and media in the form of a nitride.

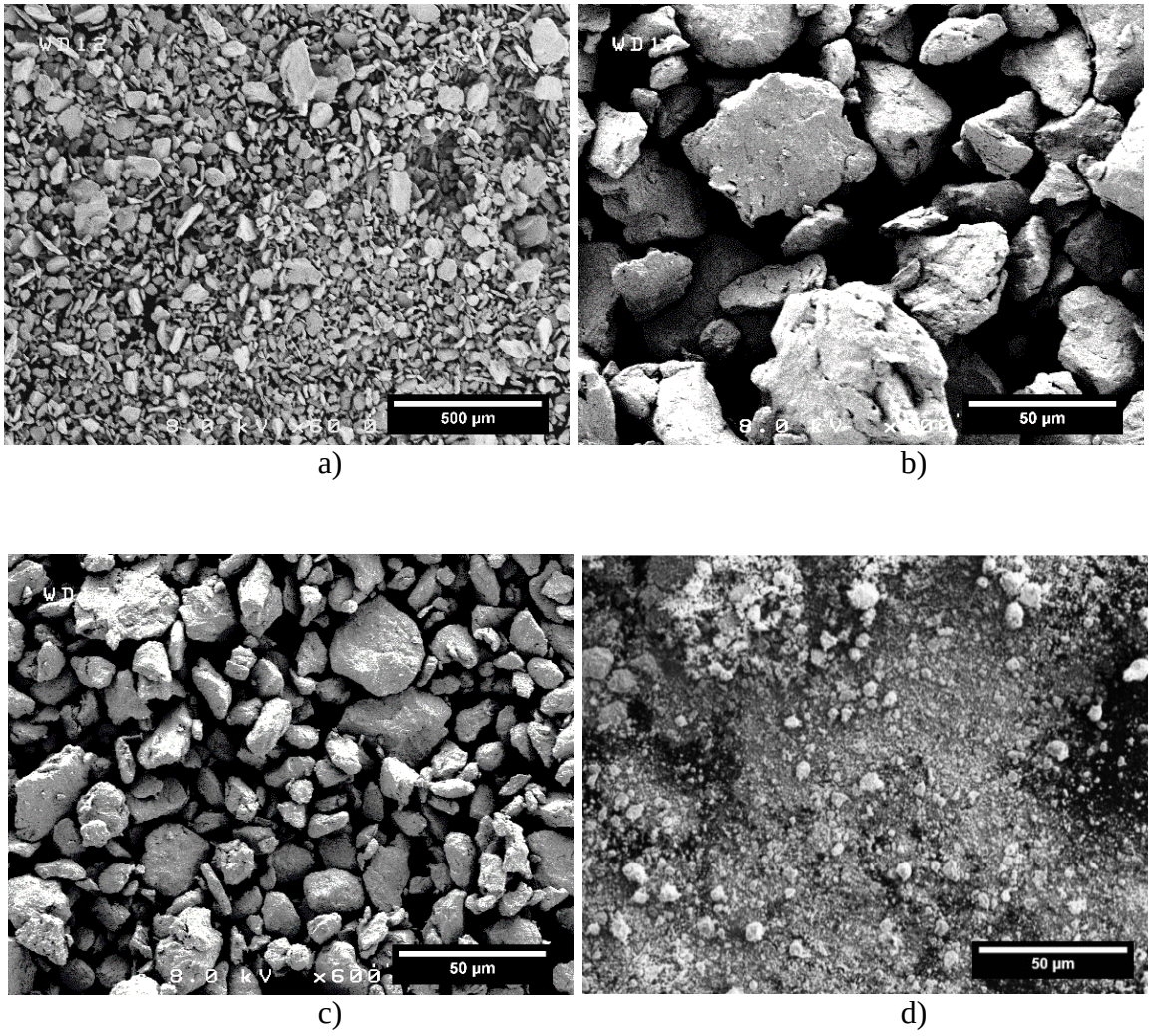

a) b)

c) d)

Figure 2.4 SEM images of the free powder recovered throughout planetary ball milling elemental dysprosium in dry nitrogen at 500 rpm for a) 10 minutes, b) 30 minutes, c) 50 minutes, and d) 24 hours.

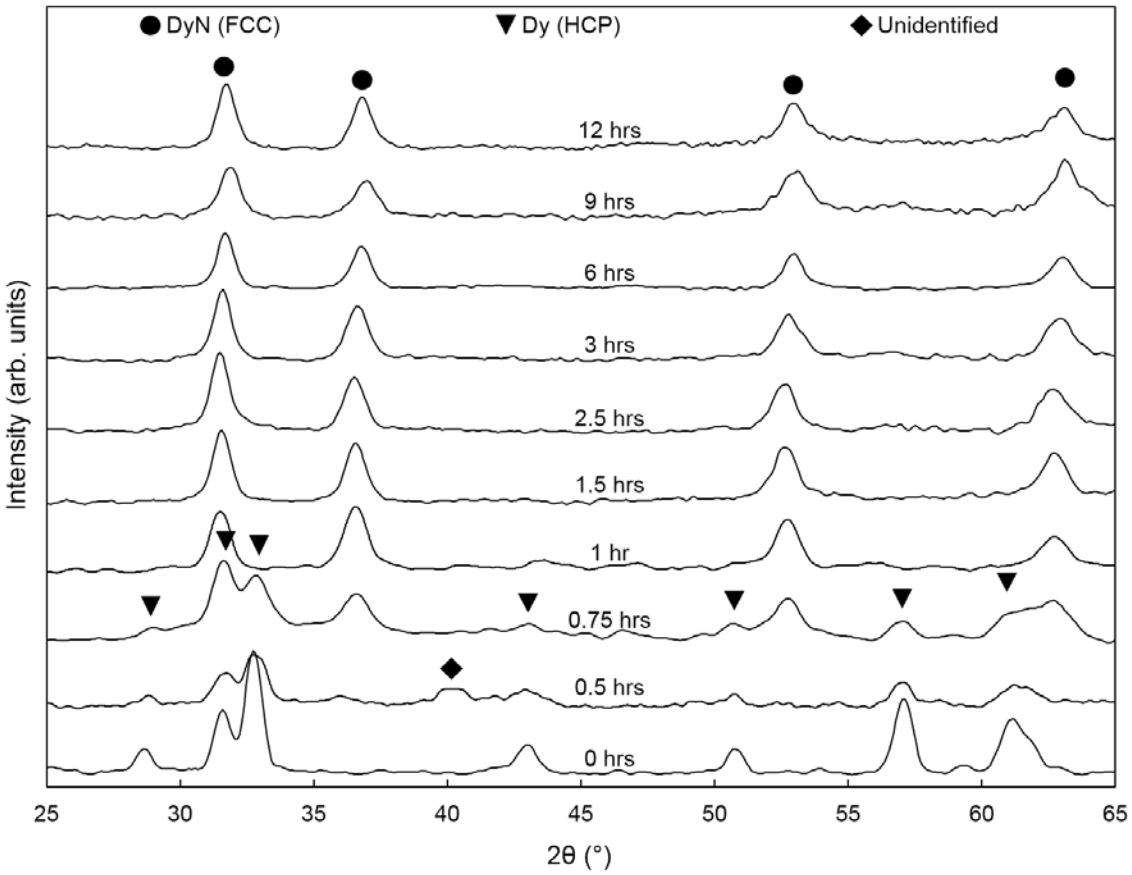

Figure 2.5 X-ray diffraction patterns of the free powders resulting from reactive milling elemental dysprosium in dry nitrogen at 500 rpm up to 12 hours. It can be seen that after approximately 1 hour of milling, the only crystalline phase of the free powder is DyN. However, as seen in Figure 2.2, the conversion was not yet complete because nearly 15% of the original mass was cold welded to the milling vessel, which was found to be primarily elemental dysprosium.

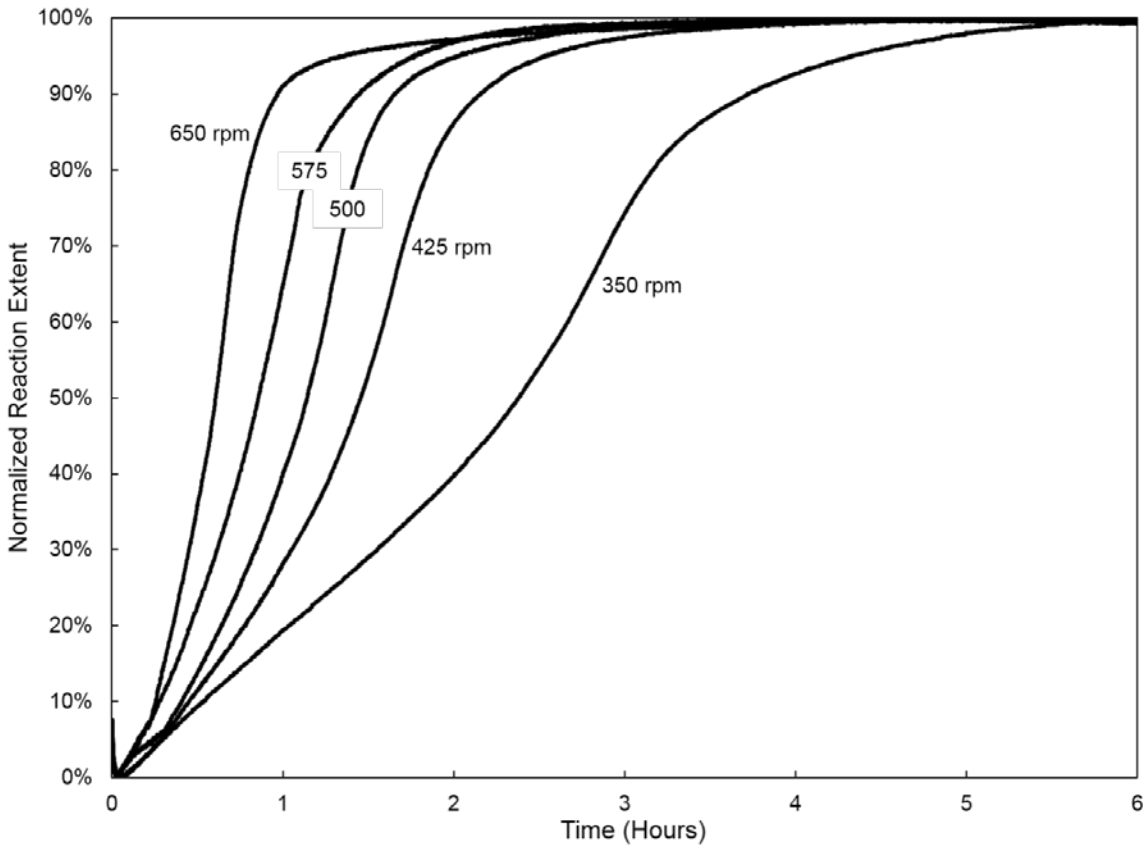

Figure 2.6 Normalized nitrogen consumption during the reactive ball milling of five grams of elemental dysprosium in dry nitrogen for six hours in a planetary ball mill at various milling intensities. The uptake was calculated using the ideal gas law and the *in situ* temperature and pressure data recorded at 0.2 Hz. It is seen that the reaction kinetics decrease with milling intensity.

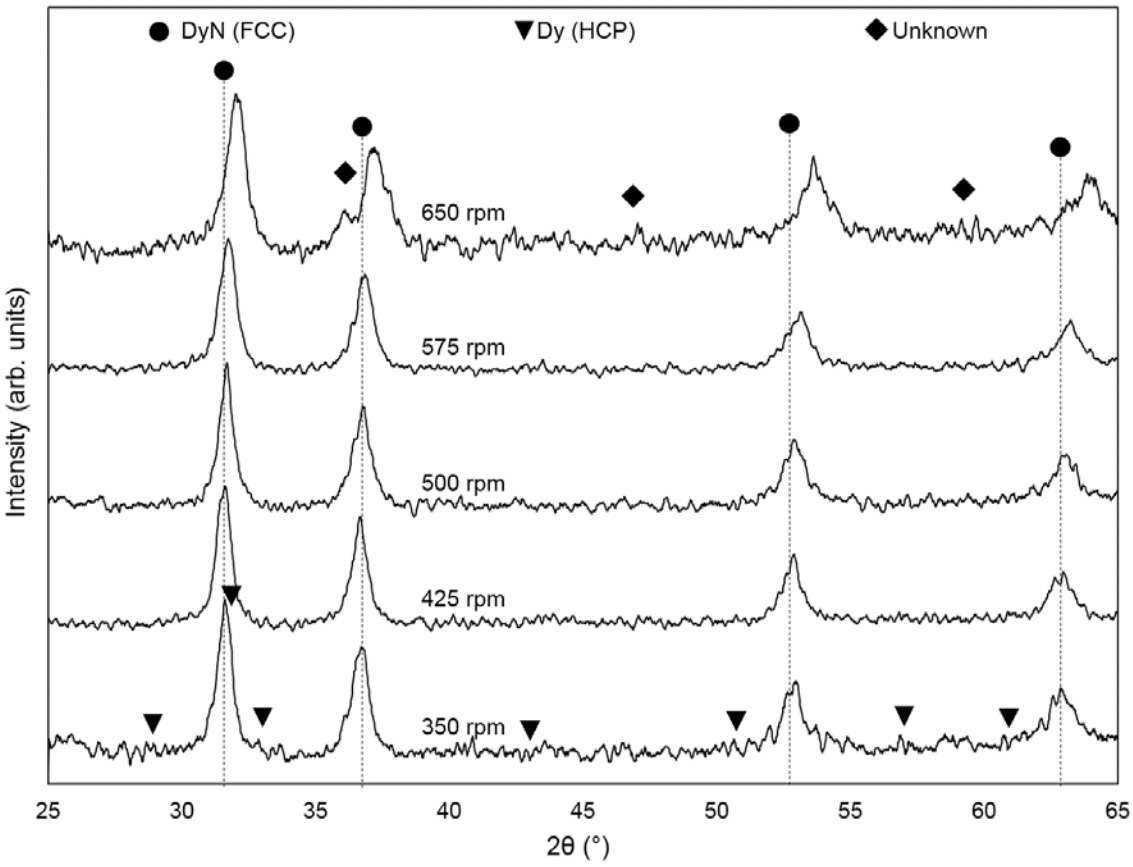

Figure 2.7 X-ray diffraction patterns of the powders resulting from reactive milling elemental dysprosium in dry nitrogen for six hours at various milling intensities. In each case, a phase pure DyN was formed.

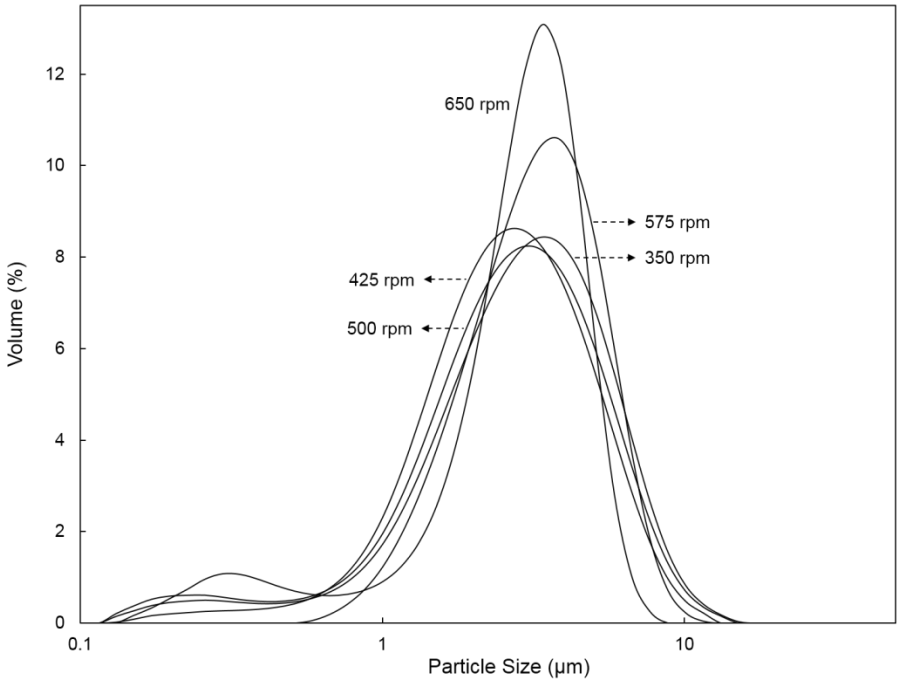

a)

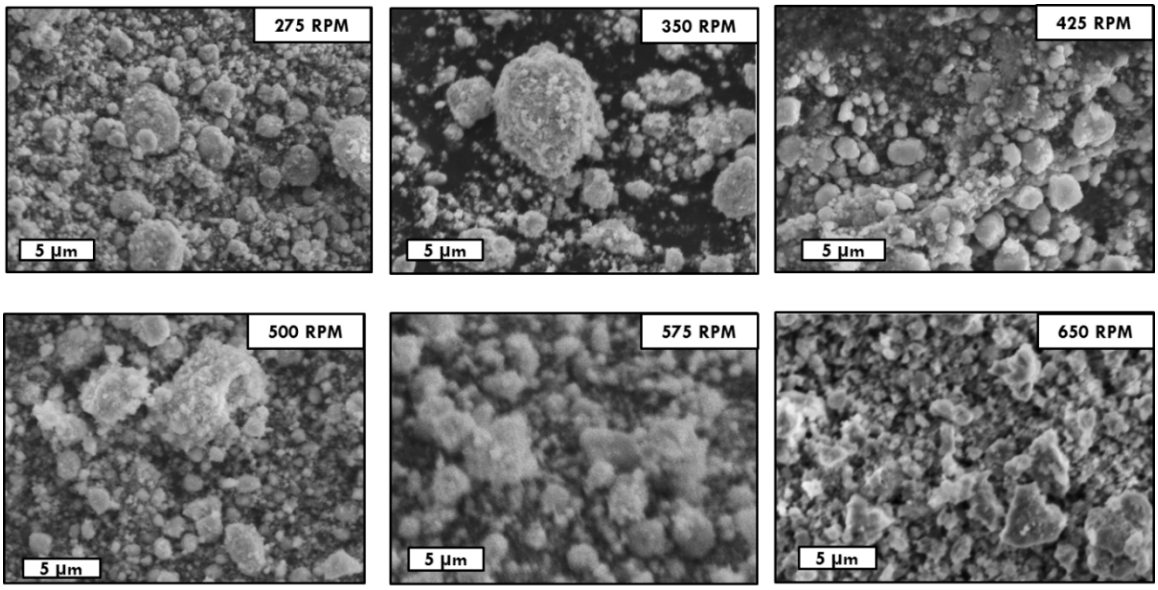

b)

Figure 2.8 The particle size distribution (a) and morphology (b) obtained from free powder resulting from reactive milling elemental dysprosium in dry nitrogen for six hours at various milling intensities. The particle size distribution suggests that, regardless of the milling intensity, the average particle size was approximately 2.6 µm, which is supported by the SEM images.

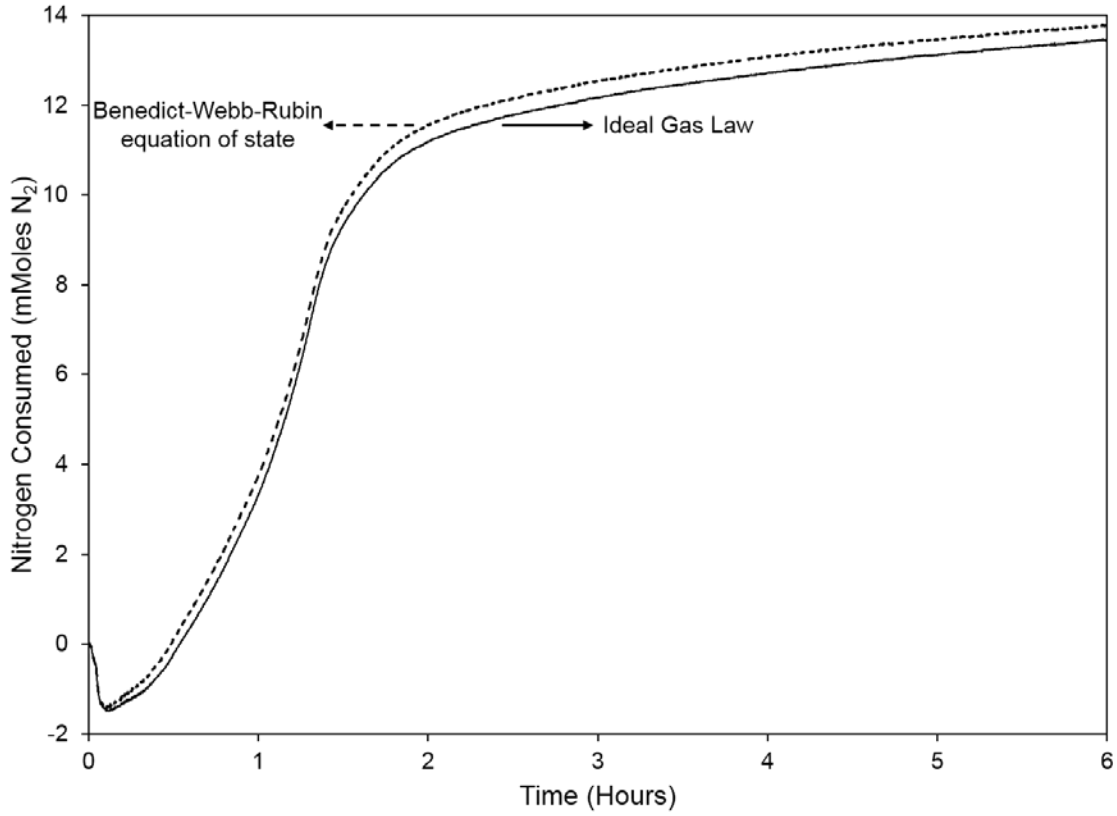

Figure 2.9 Plot showing the variance in the nitrogen consumption calculated using the ideal gas law and the Benedict-Webb-Rubin equation of state throughout the reactive ball milling of five grams of elemental dysprosium in dry nitrogen to form DyN at 500 rpm and a BPR of 14:1. The variance from the two calculations varies from 1.9% at 350 rpm to 3.5% at 650 rpm, with the ideal gas law always predicting less nitrogen consumption.

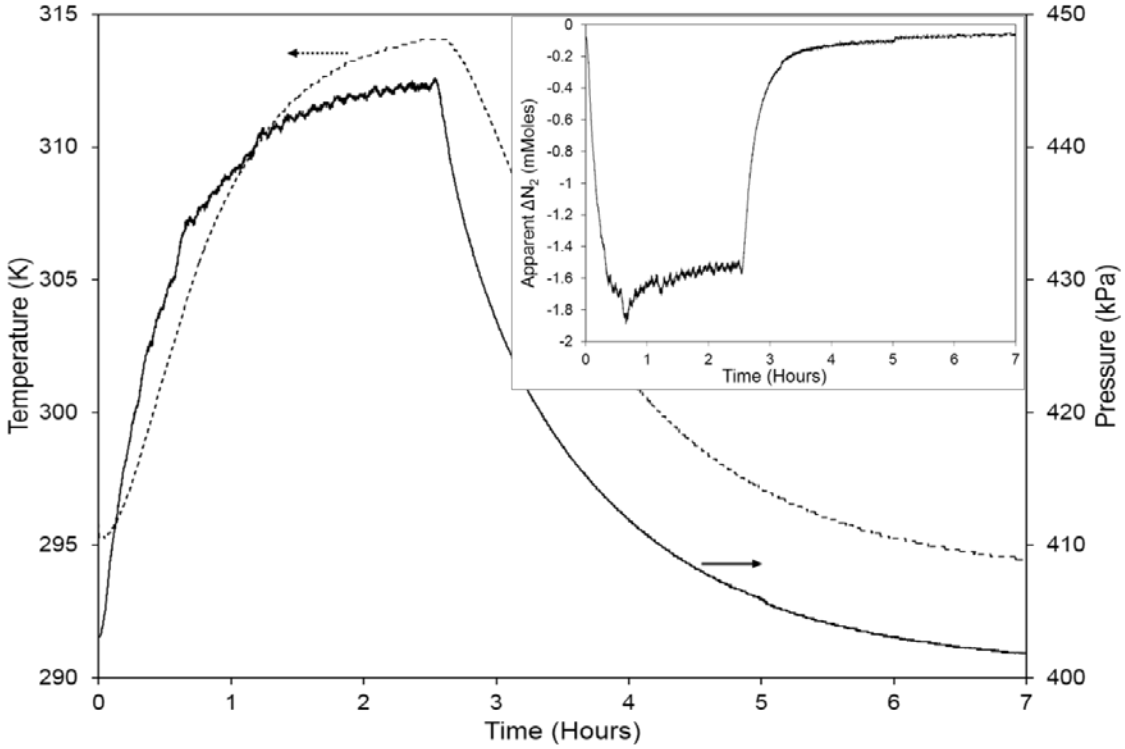

Figure 2.10 Temperature and pressure behavior sensed by the sensing lid when the milling vessel assembly is placed on a constant heat source of 332 K and removed after 2.5 hours. The inset shows the effects of the readings on the apparent change in nitrogen content as calculated using the ideal gas law. Note: The effects are an order of magnitude less than the consumption in the Dy + N_2 → DyN reaction.

Tables

Table 2.1 Empirical constants used in Benedict-Webb-Rubin equation (Equation 3) of state calculations [43] to estimate nitrogen consumption using *in situ* temperature and pressure data collected during the RM of dysprosium to form DyN.

a	A_0	b	B_0	c	C_0	α	γ
2.54	106.73	0.002328	0.04074	$7.379*10^{4}$	$8.164*10^{5}$	$1.272*10^{-4}$	0.0053

Table 2.2 Table showing the effects of calculating the nitrogen consumption using the *in situ* temperature and pressure data in the Benedict-Webb-Rubin equation of state versus the ideal gas law. It is seen that the maximum error observed between the two models occurs before the maximum nitrogen consumption rate is observed.

Milling intensity (rpm)	Time to maximum observed error (min)	Maximum error observed	Time to maximum N_2 consumption rate (min)
350	81	1.9%	175
425	66	1.8%	100
500	56	2.7%	78
575	38	3.1%	51
650	32	3.7%	39

Table 2.3 The effects of the media and dysprosium charge on the in situ temperature and pressure increase observed in the initial stages of milling dysprosium in nitrogen at 500 rpm with a 14:1 BPR of 5 mm diameter YSZ milling media (184 spheres) and dysprosium filings.

	Temperature increase (K)	Pressure increase (kPa)
Media and Dy	18 ± 1	22 ± 1
Media only	16.5 ± 0.2	16 ± 3
No charge	11 ± 1	1 ± 2

CHAPTER THREE: SYNTHESIS AND SINTERING OF UN-UO_2 FUEL COMPOSITES

This chapter has been accepted to the *Journal of Nuclear Materials*.

Synthesis and Sintering of UN-UO_2 Fuel Composites

Brian J. Jaques[a,b]

Jennifer Watkins[a,b]

Joseph R. Croteau [a,b]

Gordon A. Alanko[a,b]

Beata Tyburska-Pueschel[c]

Mitch Meyer[d]

Peng Xu[e]

Edward J. Lahoda[e]

Darryl P. Butt[a,b]

Accepted for publication in:

Journal of Nuclear Materials

March 2015

[a] *Department of Materials Science and Engineering, Boise State University, 1910 University Dr., Boise, ID 83725, USA*

[b] *Center for Advanced Energy Studies, 995 University Blvd., Idaho Falls, ID 83401, USA*

[c] *Department of Engineering Physics, University of Wisconsin-Madison, 1500 Engineering Dr., Madison, WI 53706*

[d] *Idaho National Laboratory, Idaho Falls, ID 83415, USA*

[e] *Westinghouse Electric Company LLC, Pittsburgh, PA 15235, USA*

Abstract

The design and development of an economical, accident tolerant fuel for use in the current light water reactor fleet is essential for the future of nuclear power. Uranium mononitride has been identified as an alternative fuel with higher uranium density and thermal conductivity when compared to the benchmark, UO_2, which would provide significant economic benefits. However, UN by itself reacts with water at reactor operating temperatures. In order to reduce its reactivity, the addition of UO_2 to UN has been suggested. In order to avoid carbon impurities, UN was synthesized from elemental uranium using a hydride-dehydride-nitride thermal synthesis route prior to mixing with up to 10 w% UO_2 in a planetary ball mill. UN and UN - UO_2 composite pellets were sintered in Ar - (0-1 at%) N_2 to study the effects of nitrogen concentration on the evolved phases and microstructure. UN and UN-UO_2 composite pellets were also sintered in Ar - 100 ppm N_2 to assess the effects of temperature (1700 - 2000 °C) on the final grain morphology and phase concentration.

3.1 Introduction

The United States Department of Energy (USDOE) has always emphasized safe, reliable, and economical nuclear reactor designs for sustainable operations. However, following the Fukushima-Daiichi accident in 2011, the Consolidated Appropriations Act of 2012 (report 112-75) directed the Nuclear Energy branch of the USDOE to give "special technical emphasis and funding priority to activities aimed at the development and near-term qualification of meltdown-resistant, accident tolerant nuclear fuels (ATFs) that would enhance the safety of present and future generations of light water reactors (LWRs)" [1, 2]. In the wake of this Act, ATFs have been internationally defined as fuel-

cladding systems that, when compared to traditional UO_2-zircalloy clad fuels, will provide substantially improved safety response to design basis (DB) and beyond design basis (BDB) scenarios while maintaining comparable, or improved, operational characteristics and economics during normal reactor operating conditions [1-6].

More specifically, ATFs are sought that will improve the high temperature reaction kinetics, enhance fuel and cladding thermal properties, slow hydrogen generation, and increase fission product retention as compared to the traditional uranium dioxide (UO_2)-zircalloy clad fuel [2, 7]. It is realized that researching, testing, and qualifying an ATF by 2022 [2, 8] for insertion of lead test rods into a commercial reactor with improved performance compared to UO_2 is a daunting task: UO_2 has been extensively studied and optimized over the past 60 years. An additional challenge presented by this Act is that the ATF concept should be compatible with existing LWR infrastructure, including some 400 active reactors world-wide (many of which are seeking 20+ year operation extensions) [4, 7]. Zinkle *et al.* suggest that further safety enhancements might best be achieved by a combination of fuel system innovations along with operational and/or reactor design changes [4].

High density fuels that are being considered for ATF solutions include fully ceramic microencapsulated fuels (FCM), uranium-molybdenum fuels, uranium nitride fuels, uranium carbide fuels, and uranium silicide fuels [3]. Uranium mononitride (UN) fuel forms have been demonstrated in the sodium cooled BR-10 reactor in Russia for nearly 20 years [9] as well as in the FFTF and EBR-II test reactors [3] and considered in this work due to potential advantages as a LWR fuel. According to Zakova and Wallenius [10], who modeled the neutronics behavior of UN in a BWR core, a primary advantage of

using a nitride fuel assembly in a LWR is an increased fuel cycle time. Youinou [3] predict that the fuel cycle could increase from a standard 18 month cycle (as with UO_2) to 25 month cycles based on a burnup of 50 GWd/t, calculated primarily on the increased uranium density of UN (UN contains 40% more uranium than UO_2). The increased cycle period leads to fewer refueling shut downs and is thus an economical driver for nitride fuel implementation. Although the fabrication costs are higher for UN fuels largely due to the added costs of nitrogen enrichment (greater than 90% N-15 is needed to sufficiently increase the neutron economy), the costs are offset by lower uranium enrichment requirements (3.4% U-235 in UN versus 4.2% in UO_2), and the need for a reduced number of assemblies in each reload, resulting in an estimated $5 million per year savings [3].

In addition to the economical drivers associated with nitride fuels, its desirable thermophysical properties promote its accident tolerance. A UN fuel assembly promotes large power uprates, increased cycle lengths, and allows for higher burn-up when compared to traditional UO_2 LWR fuels. These attributes are due to its high melting temperature (2762 °C), good thermal conductivity (20.5 W/m·K at 500 °C), high uranium density (13.5 g/cm^3), and lower heat capacity (230 versus 300 J/kg·K at 500 °C) [11, 12]. Zhao *et al.* [13] modeled the response of UN and UO_2 fuel behavior in SCWR accident scenarios and predicted that the larger thermal conductivity of UN (which is five times greater than UO_2) results in a significantly lower fuel centerline temperature and smaller pellet temperature gradient, resulting in lower reactor operating temperatures. Additionally, fuels with smaller heat capacities will result in a smaller peak power and stored energy release in the event of a reactivity initiated accident, such as a control rod

ejection. Since the temperature will rise faster in the UN fuel, the temperature feedback will be faster and the power pulse height will be reduced [3, 13]. The combination of both the larger thermal conductivity and lower heat capacity lead to a significantly larger safety margin in DB and BDB accident scenarios.

An additional advantage of nitride fuels are their compatibility with most potential cladding materials, their good irradiation stability, and fission product retention [3]. However, the major drawback to UN fuels are their low oxidation resistance; UN powder readily oxidizes in air and pellets in super-heated steam [14-16]. Three primary methods have been postulated to improve its oxidation resistance: Addition of USi_x to UN powder followed by liquid phase sintering, alloying UN with compounds that will increase its oxidation resistance, and coating UN with a more inert material (such as ZrC) to produce a chemical barrier [3, 9, 17]. The focus of the work presented here is to use a nitride synthesis technique that avoids excessive carbon impurities and to develop an accident tolerant fuel. The effects of adding small amounts of UO_2 (up to 10 w%) to UN fuel forms is presented. Additionally, the influence of atmosphere and temperature on the final grain morphology and stoichiometry of uranium nitride composite fuels are demonstrated.

3.2 Material and Methods

This study was completed with depleted uranium sources. UO_2 (99.8%, 50 mesh) was obtained from International Bio-Analytical Industries Incorporated (Boca Raton, FL), which was synthesized by reduction of U_3O_8 prepared via a uranyl acetate dihydrate solution route. The UN in this study was prepared from atomized elemental uranium (99.4%, 50 mesh) received from the Idaho National Laboratory (INL). The morphology

of each starting material is shown in the scanning electron microscopy (SEM) image in Figure 3.1a and b. The powders were mixed with a vacuum grease to avoid excessive oxidation during the ambient X-ray diffraction (XRD) characterization. Each of the XRD patterns were background subtracted and diffraction peaks were identified using the Inorganic Crystal Structure Database (ICSD) [18].

UN was synthesized using a thermal synthesis route in which elemental uranium was hydrided and dehydrided prior to nitridation. The thermal profile used in this work (Figure 3.2) was adapted from a series of previously published techniques [19-25]. Prior to loading into a tungsten-lined alumina crucible in an argon filled glovebox, the atomized uranium was cleaned in a 50% nitric acid solution and rinsed in methanol to remove any present oxides. A 16 gram batch was loaded into a high temperature alumina tube furnace (CM Furnaces Inc., Bloomfield, NJ, USA), which was immediately vacuum purged. As shown in Figure 3.2, the reaction was initiated by flowing ultra-high purity (UHP) hydrogen gas (H_2) over the uranium while ramping the temperature to 500 °C to "crack" the oxide barrier and form a hydride. Argon was then introduced to dehydride the powder, according to reaction 1 below. The temperature was then reduced to 225 °C and the atmosphere was switched back to UHP-H_2 where the hydrogen uptake is most rapid [25]. The hydride-dehydride process was completed 2 more times in order to remove any residual oxygen. The dehydrided uranium was then converted to nitride according to reaction 2 by introducing UHP-N_2 and ramping the temperature to 850 °C. In order to reduce the U_2N_3 to UN as described in reaction 3, argon with a reduced N_2 concentration was introduced and the temperature was briefly raised to 1200 °C before ramping to room

temperature. The resulting UN powder was characterized using SEM (Figure 3.1c) and XRD (Figure 3.3).

$$U + \frac{3}{2} H_2 \leftrightarrow UH_3 \quad (1)$$

$$2U + \frac{3}{2} N_2 \leftrightarrow U_2N_3 \quad (2)$$

$$U_2N_3 \leftrightarrow 2UN + \frac{1}{2} N_2 \quad (3)$$

Composite powders were made by mixing 5 grams of the synthesized UN with the as-received UO_2 in nominal concentrations of 5 and 10 weight percent (w%) UO_2 in an argon backfilled glovebox (maintained with less than 30 ppm O_2). Each of the three nominal compositions were mixed and milled in a planetary ball mill (Retsch PM100, Germany) in a chrome steel milling vessel. Each powder was milled for 1 hour at 400 RPM with 5 mm diameter yttria milling media in a 14:1 media:powder mass ratio. The resulting powders were characterized using SEM (Figure 3.1d) and XRD (Figure 3.4).

Prior to sintering, right cylindrical composite pellets were pressed at approximately 550 MPa in a 3.6 mm pellet die without the use of a binder or lubricant to reduce further C and O contamination. Green pellets with a geometric density of 61 ± 2 %TD were placed on a tungsten setter plate and sealed with vacuum grease and a thin polyvinylidene chloride (PVDC) film to prevent excessive oxidation while transferring into the sintering furnace. In all cases, three pellets (one of each composition) were placed on the setter together, sealed, and sintered in a tungsten refractory metal furnace (Thermal Technologies LLC., Santa Rosa, CA, USA). Once loaded into the furnace, 4 vacuum purge cycles were completed prior to ramping at 25 $^{\circ C}/_{min}$ to the desired sintering

temperature, where the temperature was held constant for 5 hours prior to ramping back to room temperature at 25 $^{\circ C}/_{min}$. Once cooled, the pellets were removed and immediately transferred into an argon glovebox.

Densities of the sintered pellets were obtained using Archimedes' principle in water at 21 °C. The measured densities of composite pellets are reported in percent theoretical density (%TD) based on the theoretical densities of UN (14.33 g/cm^{-3} [21]) and UO_2 (10.96 g/cm^{-3} [26]), respectively. The pellets were prepared for SEM and XRD by grinding approximately 1/3 of the distance through the pellet to create a cross section that was perpendicular to the two parallel faces of the right cylinder. The section face was polished with 1200 grit silicon carbide after grinding. The pellets were fixed to an aluminum sample holder using carbon tape for SEM and EDS characterization (Hitachi S-3400N-II, Japan). Following SEM, the pellets were fixed to a soda lime silica glass holder with putty and centered in the goniometer circle of an XRD (Rigaku, Miniflex 600, The Woodlands, TX, USA) equipped with a $Cu_{K\alpha}$ radiation source and a high speed linear detector.

3.3 Results and Discussion

From the SEM image shown Figure 3.1a as well as subsequent imaging not shown, it was determined that the as-received UO_2 powder possesses a bi-modal particle size distribution with a mode near 10 μm and a mode near 100 μm. XRD characterization of the UO_2 powder suggests that it is primarily a cubic UO_2 phase but does have some small percentage of a secondary phase. The secondary phase may be an off-stoichiometric U_3O_8 phase when compared to the ICSD. However, since not all of the primary diffraction peaks for U_3O_8 are present in the diffraction pattern and the peaks that are

present are shifted from published values for stoichiometric U_3O_8, the extra diffraction peaks are labeled as unknown in Figure 3.3.

The SEM image in Figure 3.1b shows that the atomized uranium is mostly spherical with the exception of a few platelets and appears to have particle size distribution with a single mode near 100 μm. By comparison with the ICSD, the XRD pattern suggests that the atomized uranium is primarily a base-centered orthorhombic α-phase uranium (α-U). Additionally, there appears to be a small fraction of a second phase, labeled as unknown in Figure 3.3, which may correspond to a slight surface oxide on the uranium spheres. However, as demonstrated in the following sections, the secondary phase has no known effects on the nitride synthesis and therefore no further analysis of the phase was conducted.

Traditionally, large quantities of high purity UN are synthesized using a carbothermic reduction of a UO_2 and carbon mixture [27, 28]. A disadvantage to the carbothermic reduction route is the unavoidable residual carbon and oxygen concentrations, which were reported as 70-670 ppm and 200-940 ppm, respectively. Accordingly, uranium monocarbide (UC) is thermodynamically predicted to form from the residual carbon, which has proven detrimental to the water corrosion resistance of uranium nitride fuels [28, 29]. It is also challenging to obtain quantitative analysis of the light elements in radioactive materials due to concerns of contamination. Previous work has shown that uranium nitride can be synthesized from elemental uranium in a high energy ball mill [30]. However, due to impurities introduced during the extensive milling process and handling of the powders, the ball milling route was not selected for UN synthesis here. In order to start with the highest purity nitride powder (especially with minimal light

element impurities), the hydride-dehydride-nitride thermal route to UN synthesis was selected as the ATF fuel fabrication route in this study.

Although difficult to scale-up to meet industry production needs, the hydride-dehydride-nitride route is a thermal synthesis route with the potential to form high purity UN with little residual oxygen and carbon, ideal for ATF applications. Many process iterations have led to the thermal profile shown in Figure 3.2. Throughout the thermal process, the atomized uranium lost its spherical shape and resulted in powder with a more irregular morphology and a significantly reduced particle size, as seen in Figure 3.1c. Further characterization via XRD suggests that the powder is a phase-pure cubic UN when compared to the ICSD, as shown in Figure 3.3.

Ball milling the nominal compositions of UN, UN - 5 w% UO_2, and UN - 10 w% UO_2 was primarily completed for two reasons: to obtain a homogenous mixture and to increase the sinterability of the green pellets. As seen in the SEM image of Figure 3.1c and d, the milling process significantly reduced the particle size from 5-10 μm to less than 1 μm, increasing the sintered density by 5% of the theoretical density (TD) at 1900 °C for 5 hours, when compared to as synthesized UN. Additionally, milling significantly reduced the crystallite size of the powder from 95 ± 10 nm down to 27 ± 5 nm, as determined using the Scherrer equation and the first two UN diffraction peaks shown in Figures 3.3 and 3.4. However, the high energy milling process reduced the crystallinity of the powder, thus reducing the amount of information that can be inferred from XRD analysis. In the diffraction pattern for pure UN in Figure 3.4, a clear second phase formed from the milling process, noted by broad diffraction peaks at approximately 29, 47.5, and 57 °2θ. Thermodynamics predict that milling a nitride in a pure argon

atmosphere would cause a portion of the nitrogen to dissociate from the uranium, resulting in an elemental uranium phase. However, the peaks do not align with an elemental uranium phase: they are more indicative of a hyper-stoichiometric UN (UN_{1+x}) phase. This very interesting but counterintuitive result will be discussed further below. As seen in the diffraction pattern for UN - 10 w% UO_2, broad diffraction peaks from the added UO_2 phase along with the broad diffraction peaks from the UN_{1+x} phase are present. Although it is not clear how much oxygen may have been picked up from handling and milling, the powder is presumed to contain more oxygen after milling than before.

Further characterization of the milled powders was completed using SEM and energy dispersive X-ray spectroscopy (EDS). Although the EDS showed that the powder was homogeneously mixed by the absence of large oxide agglomerates, an artifact from milling was detected. EDS showed that there was a 0.8 ± 0.3 at% zirconium concentration, which is an impurity due to the degradation of the zirconia milling media during milling and is a common artifact of high energy milling. It can be mitigated by careful choice of milling media and milling vessel materials. Additionally, the added handling step, along with increased surface area, will increase the residual oxygen concentration in the UN powders, as seen in the XRD.

Composite powders were pressed into green pellets of 60 ± 2 %TD in an Ar-filled glovebox (<30 ppm O_2) prior to loading into the furnace. From past experience, pellets that were not ball milled were able to be briefly exposed to air (as in the case of transferring into the sintering furnace). However, green pellets pressed from the milled powders were pyrophoric and immediately ignited when exposed to oxygen. Therefore,

oxygen exposure was minimized by sealing the sintering crucible with vacuum grease and a PVDC film prior to removal from the glovebox for insertion into the sintering furnace. Both the vacuum grease and the PVDC film were subsequently burned off in the furnace while ramping to the sintering temperature, contributing to light element impurity concentration in the final sintered product.

Although the effects of nitrogen concentration in the sintering environment have been studied for UN and (U,Pu)N in the past [28, 31-34], it has not been studied in the fabrication of UN-UO_2 composites, to the best of the authors' knowledge. It is well known that the concentration of nitrogen in the processing environment affects the final microstructure and stoichiometry of the fuel pellets. Secondary phases can be detrimental to the fuel performance; the presence of a liquid uranium phase is undesirable because if heated and irradiated it would cause the fuel to swell, creep, and react with the fuel cladding. Additionally, the presence of U_2N_3 is undesirable because, upon heating in reduced nitrogen conditions, it will dissociate according to Equation 2. Not only will the nitrogen evolution cause the fuel pin to pressurize and result in undesirable cladding embrittlement, it can also cause fuel to crack during sintering or irradiation [28].

As noted in the U-N binary equilibrium phase diagram [28], UN is a line compound at low temperatures and has a small phase field with increased temperature. However, previous work predicts that the UN phase field is much larger when considering equilibrium nitrogen concentrations. It has been estimated that the nitrogen pressure can span nine orders of magnitude during sintering within the UN phase field at 1550 °C [32, 33]. Additionally, it is stated that the nitrogen concentration during sintering is best kept in a narrow range near the UN dissociation boundary (Equation 4) to reduce the amount

of dissolved nitrogen. Tennery *et al.* [32] also found that microstructural features and density were increased when choosing a nitrogen pressure close to the UN dissociation boundary.

$$UN \rightarrow U + \frac{1}{2} N_2 \tag{4}$$

To demonstrate the effects of reduced nitrogen environments during sintering, a UN pellet was subjected to 1550 °C for 5 hours in UHP - Ar. As seen in the SEM image of the polished section of Figure 3.5, a “coring” effect was observed near the pellet surface. It is worth noting that the thickness of the dense ring decreased with increased distance from the top surface due to the increased activity at the corners of the right cylinder. The dense ring observed around the perimeter of the pellet is due to hypo-stoichiometric nitrogen conditions causing the formation of free uranium, described by Equation 4. As shown in the higher magnification images in Figure 3.5, region 1 shows a microstructure in the center of the pellet where the UN was only partially sintered to a low density, whereas region 2 shows a dense microstructure where the free uranium formed a liquid phase and accelerated the sintering kinetics. However, the density was measured as nearly 80 %TD, which is much greater than the apparent density from region 1 and much less than predicted in region 2. Therefore, the reported density is an average of the dense shell and the porous core structures.

Since the core of the pellet subjected to 1550 °C for 5 hours was only partially sintered, atmospheric sintering studies were completed at 1900 °C to provide a denser microstructure. The three gases used were UHP-Ar (<4 ppm N_2), Ar - 100 ppm N_2, and Ar - 1 at% N_2 according to the acceptable range of nitrogen pressure proposed in previous work [32, 33]. The effects of nitrogen pressure during sintering on the

microstructure and phase evolution is shown in Figures 3.6 and 3.7, respectively. Edge effects are pronounced in the pellets sintered in pure Ar; therefore, for comparison purposes, only cross sections of the pellet cores (near the middle of the pellet cross section) are compared using SEM, EDS, and XRD. EDS was used to identify the dark regions in the backscattered electron (BSE) SEM images as a U-O phase, shown in Figure 3.6 and 3.8. Further quantification of the U-O phase is not reported here because the relative error for C, N, and O concentrations using EDS is relatively large and stoichiometry can only be inferred.

EDS was primarily used to detect the presence of oxygen and nitrogen, not their concentrations. Accordingly, small oxygen concentrations were detected in the UN phase in all of the samples in this study. It is unknown if the oxygen detected was formed on the surface of the polished section or if it is dissolved oxygen but it has been shown that the oxygen solubility in pure UN can reach values in excess of 5 at% and can be determined by a slight lattice expansion in XRD [35-37]. Dissolved oxygen and surface oxides were likely detected on these samples due to the very reactive nature of the powders and green pellets after milling. Comparing Figure 3.7 with Figure 3.4 shows that the broad peaks observed in the milled powders evolved into relatively well-defined diffraction peaks after sintering. XRD shows UN as the primary phase in all cases although, as expected, there are prominent UO_2 peaks, which increase with nominal UO_2 additions. Peaks are also present which correspond slightly to hyper-stoichiometric UN (UN_{1+x}) as compared to the ICSD along with unidentified peaks in each diffraction pattern. Furthermore, the unidentified peaks are generally positioned between closely spaced UN and UO_2 peaks. Since the UN powders were milled and sintered in virtually nitrogen free environments

(Ar atmosphere of glovebox and UHP-Ar, respectively), it is unlikely that the peaks are due to a hyper-stoichiometric nitride phase. Additionally, the pellets sintered in UHP-Ar show the same peaks corresponding to a UN_{1+x} phase although thermodynamics and past experience suggest that the hyper-stoichiometric nitride phase will be reduced to UN or UN + U + N_2 when exposed to temperatures greater than 1100 °C. It seems as though the addition of UO_2 either stabilizes a hyper-stoichiometric nitride phase or a uranium oxynitride phase is being formed. The reported ICSD peak positions for α-U are indicated for the samples sintered in pure Ar since the dissociation reaction (Equation 4) was predicted to occur. Although the coring effect was observed in macro images of these samples similar to Figure 3.5, peaks for α-U have only a slight correlation with the diffraction pattern (Figure 3.7). Although not clearly identified using XRD, EDS shows distinct regions of elemental uranium on grain boundaries within the UN microstructures.

As shown in Figure 3.6, the U-O phase is uniformly distributed throughout each of the microstructures and although it is also observed in pure UN samples, its concentration increases with nominal additions of UO_2. However, a few trends are observed in the microstructures: The microstructure becomes finer with (1) increased UO_2 additions and (2) increased nitrogen concentration during sintering. These findings are in agreement with past literature that reported a decrease in grain size with increased oxygen (up to 1 w%) and finer microstructures with increased nitrogen concentrations [32, 37]. Tennery *et al.* [32] also noted that the final densities of the pellets were indicative of the resulting grain sizes rather than the sintering temperature or nitrogen pressure.

Based on the studies presented above and work presented in previously publish work [28, 32, 33], the effect of sintering temperature were studied from 1700 - 2000 °C in Ar -

100 ppm N_2. The resulting pellet microstructures and phase evolution are shown in Figures 3.8 and 3.9, respectively. As seen in the BSE SEM images in Figure 3.8, pore sizes increased with increased sintering temperature. Contrary to previously published work on sintering of pure UN [28, 32], increased sintering temperatures resulted in decreased densities. Sintering for 5 hours at 1700 °C resulted in a density of approximately 93 %TD for each composition whereas sintering at 2000 °C resulted in a density of 88 %TD. Although a coarsening effect was observed in the UN grains, the U-O grains, and the pores with increased temperature, the UN grains also appear to coarsen with increased UO_2 additions, as seen in Figure 3.8. The U-O grains remained homogeneously distributed throughout the microstructures and appeared only on grain boundaries. However, the frequency of U-O grains decreased with increasing temperature, also due to a coarsening effect. An additional note is that the pores shown in the microstructures tend to be lined with an oxide phase, as determined via EDS. The oxide present at the free surfaces is an attribute that will likely increase the accident tolerance of UN fuels.

Similar to the nitrogen concentration study presented above, XRD confirmed the presence of a UO_2 phase in each of the pellets (Figure 3.9) and EDS confirmed the presence of a surface oxide or dissolved oxygen in the bulk of the samples. The XRD also shows unidentified diffraction peaks most notably from 39-46 °2θ. An interesting observation from Figure 3.9 is that the number of unknown diffraction peaks decreases with increasing temperature as well as with increased additions of UO_2. As previously mentioned, the dissolution of oxygen into the UN structure results in a lattice expansion [35-37], which would result in lower 2θ values in the observed diffraction peaks.

However, the diffraction peaks for UN in Figure 3.9 are shifted slightly to the right of the positions provided by the ICSD, suggesting a lattice contraction and providing support for the hypothesis that the unidentified peaks represent a potential hyper-stoichiometric nitride phase or a uranium oxynitride phase.

3.4 Conclusions

A process to convert elemental uranium to high purity, carbon free uranium mononitride was demonstrated using a hydride-dehydride-nitride synthesis route. The resulting UN was blended with 0, 5, and 10 w% UO_2 in a high energy ball mill, creating a homogenous mixture with a significantly reduced particle size and a damaged structure. The powder became pyrophoric and readily picked-up oxygen, which contributed to additional oxide phases as well as dissolved oxygen in the sintered pellets. Even the consolidated, green pellets were pyrophoric and prone to rapid oxidation upon exposure to air. UN and UO_2 composite pellets were sintered at 1900 °C for 5 hours in UHP-Ar, Ar - 100 ppm N_2 and Ar - 1 at% N_2 to gain insight into the effects of nitrogen on the stability of the nitride phases and distribution of oxides. Sintering in UHP-Ar resulted in a coring effect in which UN was dissociated to elemental uranium at grain boundaries, resulting in pronounced liquid-phase sintering and increased densification around the perimeter of the UN pellet. The addition of small amounts of UO_2 as well as nominally increased nitrogen in the sintering atmosphere resulted in finer microstructure, including nitride grains, oxide grains, and pores. Further studies were performed to assess the effects of sintering temperature in Ar - 100 ppm N_2 from 1700 - 2000 °C. In each case, U-O grains were homogenously distributed throughout the pellet microstructure and existed primarily on UN grain boundaries. The pores were also lined with an oxide phase. Increasing UO_2

additions resulted in microstructural coarsening, as did the sintering temperature. Higher sintering temperatures also resulted in lower sintered densities, presumably due to a preferential formation of oxygen-stabilized nitrides or uranium oxynitrides.

The work presented here demonstrates a viable synthesis process for fabricating carbon free UN-UO_2 accident tolerant fuels for the current fleet of LWRs. Although a new fuel concept has been developed, there is a lengthy process in order to demonstrate its improved accident tolerance. Further work must be completed to determine if controlled UO_2 additions enhance the accident tolerance of UN to high temperature oxygen and steam exposures while maintaining thermophysical properties comparable or better than the benchmark LWR fuel, UO_2.

Acknowledgements

This project was supported by the Department of Energy Nuclear Energy University Program (DOE-NEUP) grant #00120690. The authors would also like to acknowledge Joshua Heuther and Daniel Osterberg from Boise State University, Todd Allen, Doug Toomer, Curtis Clark, Jason Harp, and Paul Lessing from the Idaho National Laboratory and Ken McClellan from Los Alamos National Laboratory for fruitful discussions, support, and materials procurement.

Author Justification

The research presented in this publication was carried out by Brian Jaques, Jennifer Watkins, Joseph Croteau, Dr. Gordon Alanko, and Dr. Darryl Butt. Brian coordinated the work, synthesized the materials, collected much of the experimental data, and authored the manuscript. Jennifer and Joseph assisted in materials preparation and characterization. Dr. Alanko provided foundational studies and insight. Dr. Alanko, Dr.

Beata Tyburska-Pueschel, Dr. Mitch Meyer, Dr. Peng Xu, Dr. Edward Lahoda, and Dr. Butt all contributed fruitful discussions, ideas, and vision. Work done by Brian Jaques was in partial fulfillment of the requirements for a Doctoral degree in Materials Science and Engineering at Boise State University, under the advisement and supervision of Dr. Butt. Dr. Butt contributed greatly in terms vision, ideas, advisement, critical review of the article throughout the writing process, and financial support.

References

[1] L.J. Ott, K.R. Robb, D. Wang, Journal of Nuclear Materials, 448 (2014) 520-533.

[2] F. Goldner, Development Strategy for Advanced LWR Fuels with Enhanced Accident Tolerance, in: Enhanced Accident Tolerant LWR Fuels National Metrics Workshop, Germantown, MD, 2012.

[3] G.J. Youinou, R.S. Sen, Nuclear Technology, 188 (2014) 123-138.

[4] S.J. Zinkle, K.A. Terrani, J.C. Gehin, L.J. Ott, L.L. Snead, Journal of Nuclear Materials, 448 (2014) 374-379.

[5] D.M. Wachs, N. Woolstenhulme, Transactions of the American Nuclear Society, 110 (2014) 42-46.

[6] K. Yang-Hyun, Y. Jae-Ho, P. Jeong-Yong, K. Keon-Sik, K. Hyun-Gil, K. Dong-Joo, J. Yang-Il, S. Kun-Woo, Nuclear Technology, 186 (2014) 295-304.

[7] N.R. Brown, A. Aronson, M. Todosow, R. Brito, K.J. McClellan, Nucl. Eng. Des., 275 (2014) 393-407.

[8] S. Bragg-Sitton, B. Merrill, M. Teague, L.J. Ott, K.R. Robb, M. Farmer, M. Billone, R. Montgomery, C. Stanek, M. Todosow, N.R. Brown, Advanced fuels campaign: Enhanced LWR accident tolerant fuel performance metrics, INL/LTD-13-30226, FCRD-FUEL-2013-000264, Idaho National Laboratories, 2013.

[9] P.A. Lessing, Oxidation protection of uranium nitride fuel using liquid phase sintering, INL/EXT-12-24974, Idaho National Laboratories, 2012.

[10] J. Zakova, J. Wallenius, Ann. Nucl. Energy, 47 (2012) 182-191.

[11] S.L. Hayes, J.K. Thomas, K.L. Peddicord, Journal of Nuclear Materials, 171 (1990) 289-299.

[12] S.L. Hayes, J.K. Thomas, K.L. Peddicord, Journal of Nuclear Materials, 171 (1990) 300-318.

[13] H. Zhao, D.H. Zhu, K.S. Chaudri, S.Z. Qiu, W.X. Tian, G.H. Su, Prog. Nucl. Energy, 71 (2014) 152-159.

[14] S. Sugihara, S. Imoto, J Nucl Sci Technol-T, 6 (1969) 237.

[15] S. Sunder, N.H. Miller, Journal of Alloys and Compounds, 271 (1998) 568-572.

[16] G.A.R. Rao, S.K. Mukerjee, V.N. Vaidya, V. Venugopal, D.D. Sood, Journal of Nuclear Materials, 185 (1991) 231-241.

[17] K.S. Chaudri, W.X. Tian, Y.L. Su, H. Zhao, D.H. Zhu, G.H. Su, S.Z. Qiu, Prog. Nucl. Energy, 63 (2013) 57-65.

[18] Inorganic crystal structure database, in, FIZ Karlsruhe Karlsruh, Germany.

[19] A.A. Bauer, Reactor Technology, 15 (1972) 87-104.

[20] J.M. Cleveland, G.H. Bryan, C.R. Heiple, R.J. Sironen, Nuclear Technology, 25 (1975) 541-545.

[21] H. Matzke, Science of Advanced LMFBR Fuels, Elsevier Science Publishing Company, Inc., Amsterdam, The Netherlands, 1986.

[22] N.H. Olschewski, J.-P. Glatz, H. Bokelund, M.J.-F. Leroy, Journal of Nuclear Materials, 188 (1992) 244-248.

[23] N. Oi, S. Hirayama, I. Tanabe, A. Muramatsu, T. Kawada, Journal of Nuclear Science and Technology, 9 (1972) 521-527.

[24] M. Paljevic, Z. Despotovic, Journal of Nuclear Materials, 57 (1975) 253-257.

[25] W.D. Wilkinson, Uranium Metallurgy: Uranium Process Metallurgy, Interscience Publishers, New York, 1962.

[26] D.J. Kim, Y.S. Kim, S.H. Kim, J.H. Kim, J.H. Yang, Y.W. Lee, H.S. Kim, Thermochimica Acta, 441 (2006) 127-131.

[27] T. Muromura, H. Tagawa, Journal of Nuclear Materials, 71 (1977) 65-72.

[28] R.B. Matthews, K.M. Chidester, C.W. Hoth, R.E. Mason, R.L. Petty, Journal of Nuclear Materials, 151 (1988) 334.

[29] J. Bugl, A.A. Bauer, Corrosion and oxidation characteristics of uranium mononitride, 13, Nuclear Metallurgy, Ann Arbor, MI, 1964.

[30] B.J. Jaques, B.M. Marx, A.S. Hamdy, D.P. Butt, Journal of Nuclear Materials, 381 (2008) 309.311.

[31] V.J. Tennery, E.S. Bomar, Transactions of the American Nuclear Society, 19 (1974) 101-102.

[32] V.J. Tennery, T.G. Godfrey, R.A. Potter, Journal of the American Ceramic Society, 54 (1971) 327-331.

[33] H. Matzke, Journal of the Chemical Society Faraday Transactions, 86 (1990) 1243-1256.

[34] H. Inouye, J.M. Leitnake, Journal of the American Ceramic Society, 51 (1968) 6.

[35] N.A. Javed, Journal of the Less-Common Metals, 29 (1972) 155.

[36] G.C. Jain, C. Ganguly, Journal of Nuclear Materials, 202 (1993) 245-251.

[37] Y. Arai, M. Morihira, T. Ohmichi, Journal of Nuclear Materials, 202 (1993) 70-78.

Figures

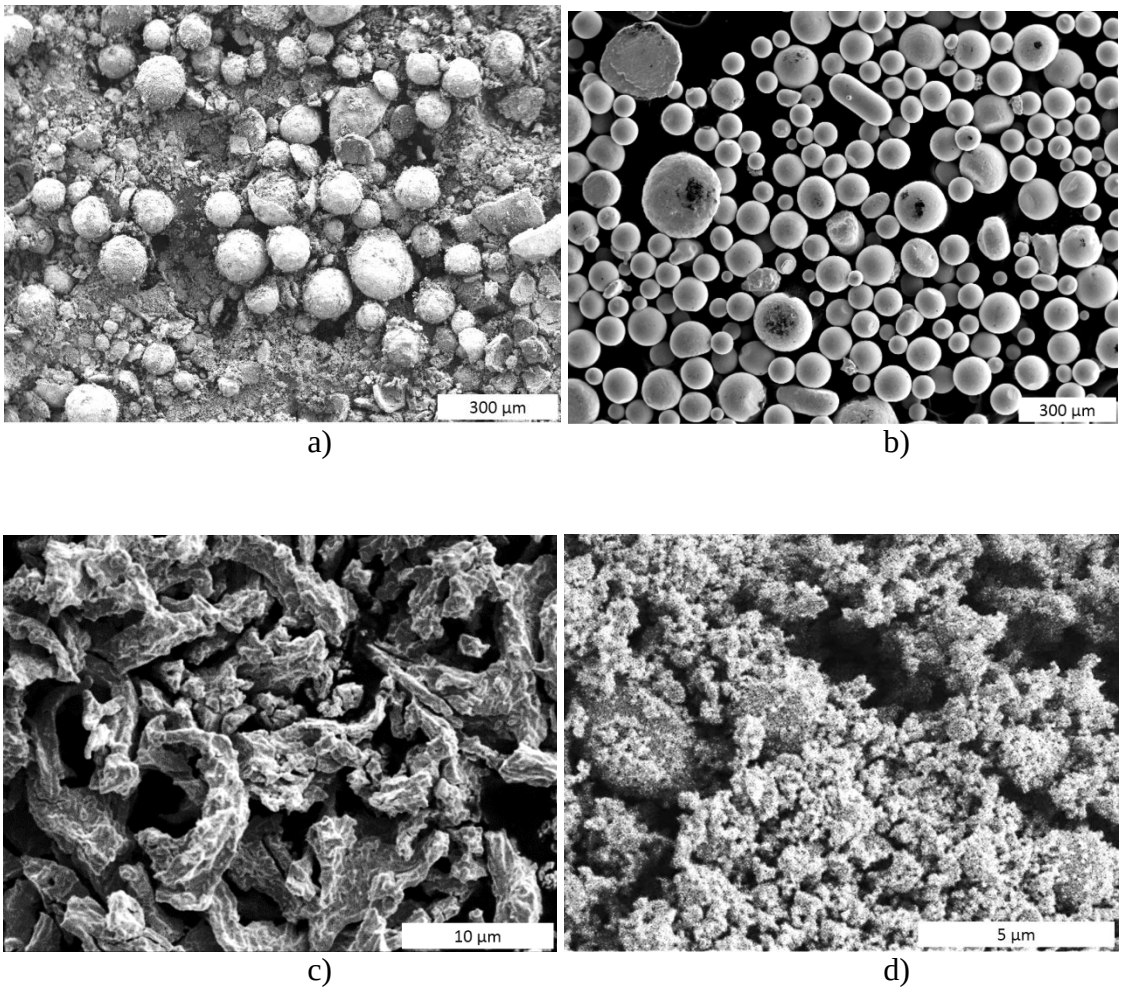

Figure 3.1 Scanning electron images of precursor powders for the nitride composite pellet fabrication: a) As-received UO_2 from bioanalytical industries, b) as-received atomized uranium, c) UN after hydriding and nitriding the atomized uranium via the thermal route shown in Figure 3.2, and d) UN-UO_2 composite powder after milling for 1 hour at 400 RPM in a planetary ball mill.

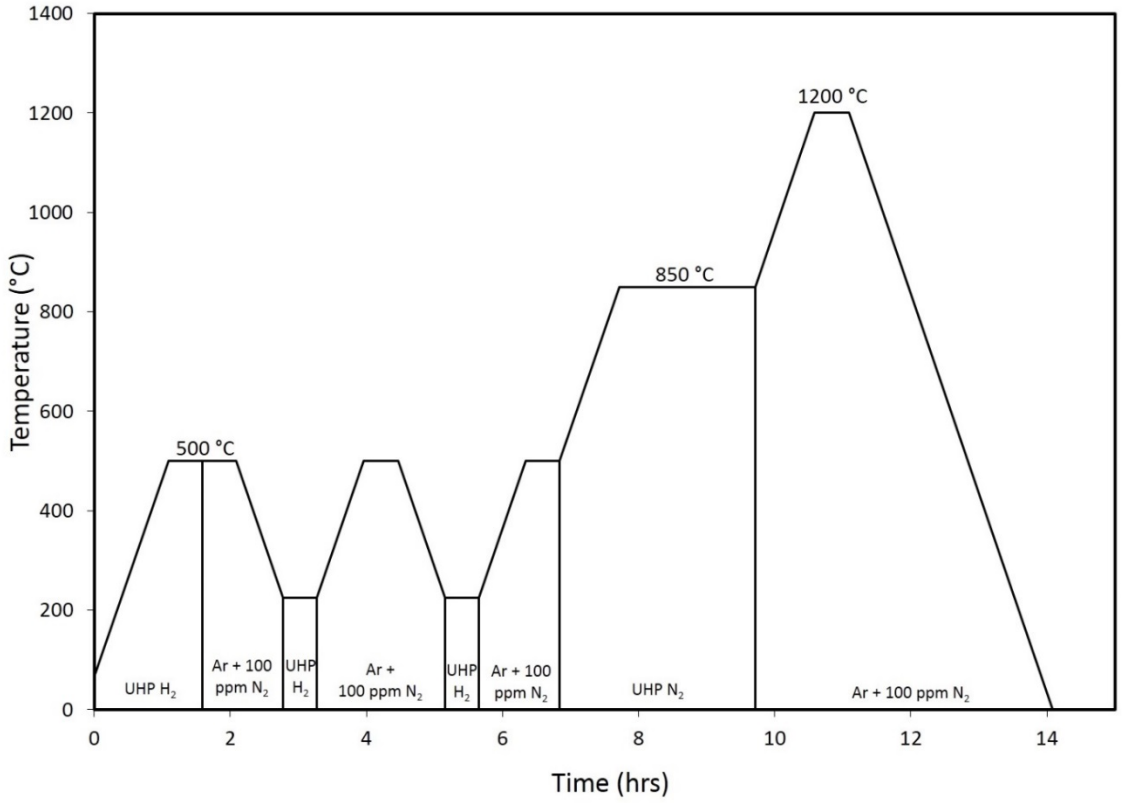

Figure 3.2 Thermal process used to hydride prior to nitride the atomized depleted uranium shown in Figure 3.1.

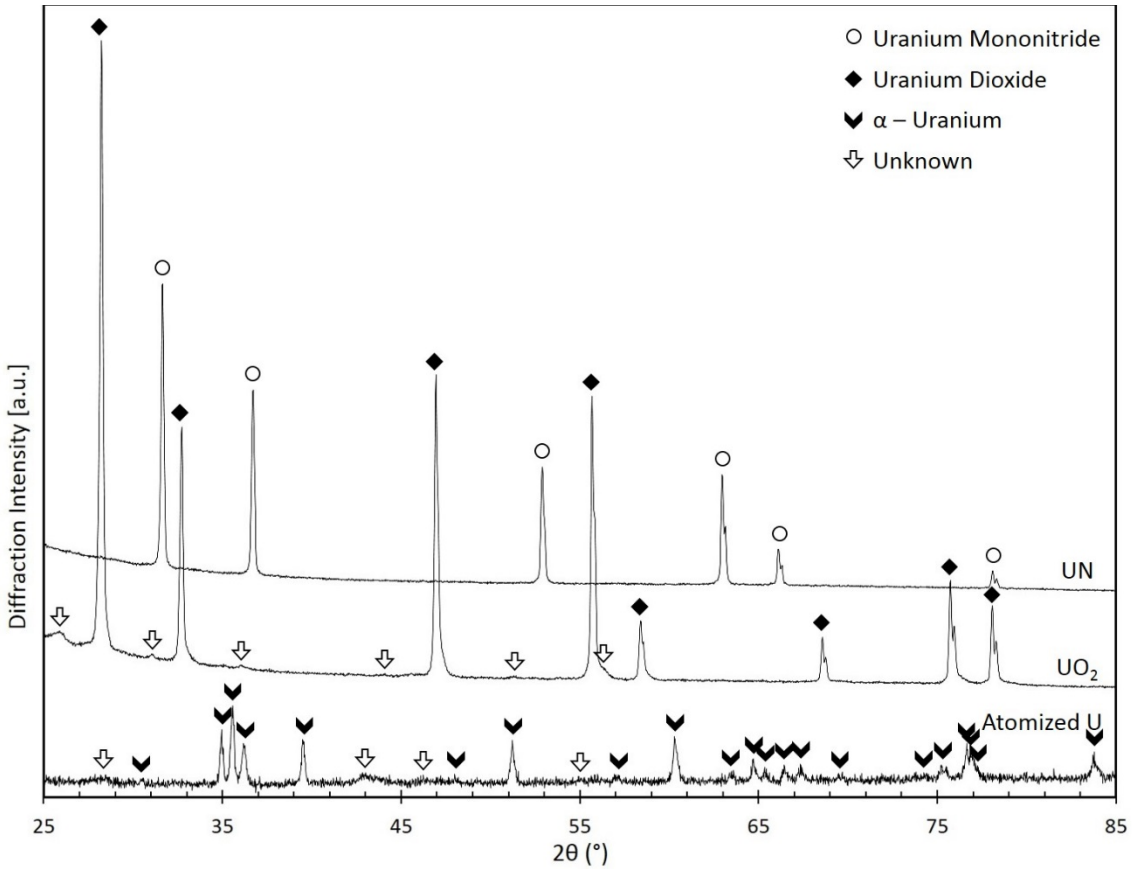

Figure 3.3 X-ray diffraction patterns of precursor powders for composite nitride fuel pellet fabrication, including the as-received atomized D-U and UO_2 as well as the UN after hydriding and nitriding D-U via the thermal route shown in Figure 3.2.

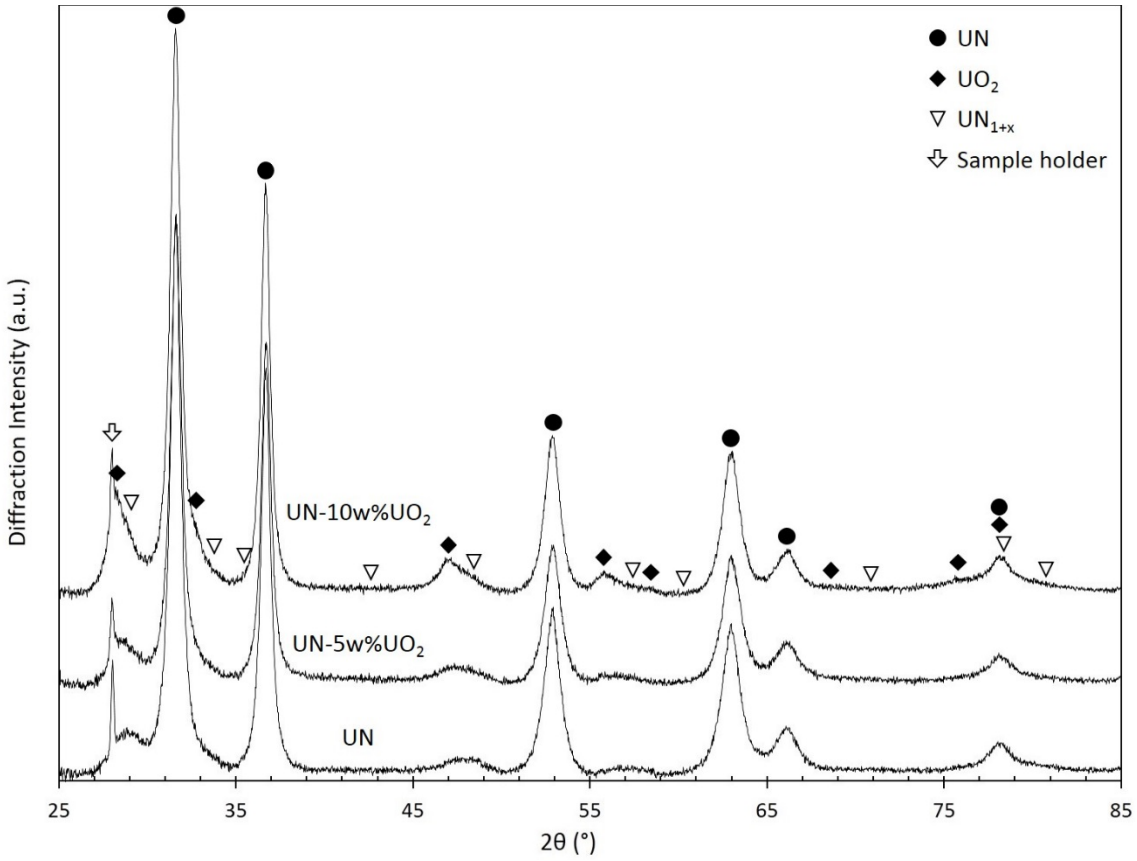

Figure 3.4 X-ray diffraction patterns of nominal compositions of UN, UN-5 w% UO_2, and UN-10 w% UO_2 after milling for 1 hour in a planetary ball mill at 400 RPM.

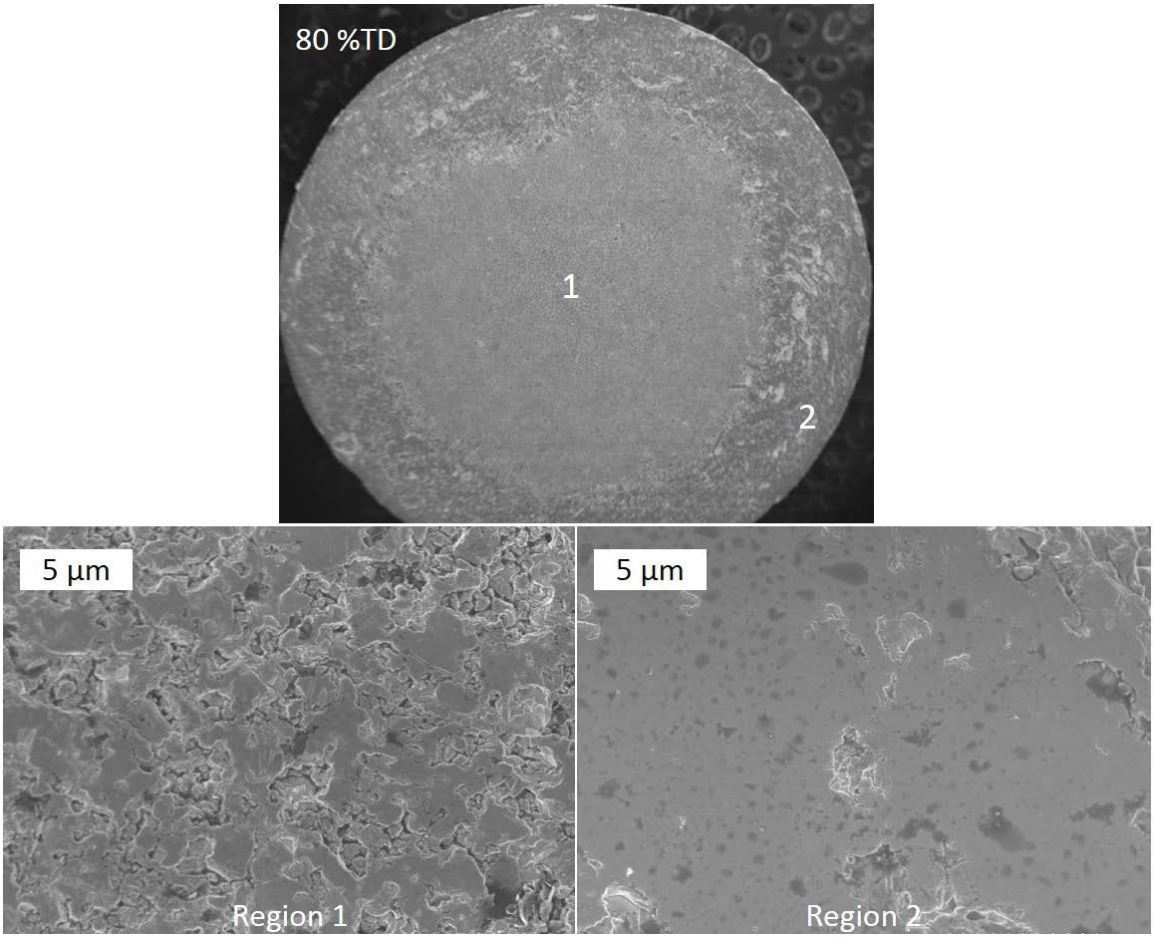

Figure 3.5 SE-SEM image of the ground surface of a UN pellet sintered at 1550 °C for 5 hours in a pure argon atmosphere showing a distinct dense layer around the circumference of the pellet. The "coring" effect is due to the low nitrogen pressure in the sintering environment, causing a dissociation of the nitrogen and uranium, leading to the formation of a liquid phase and localized densification.

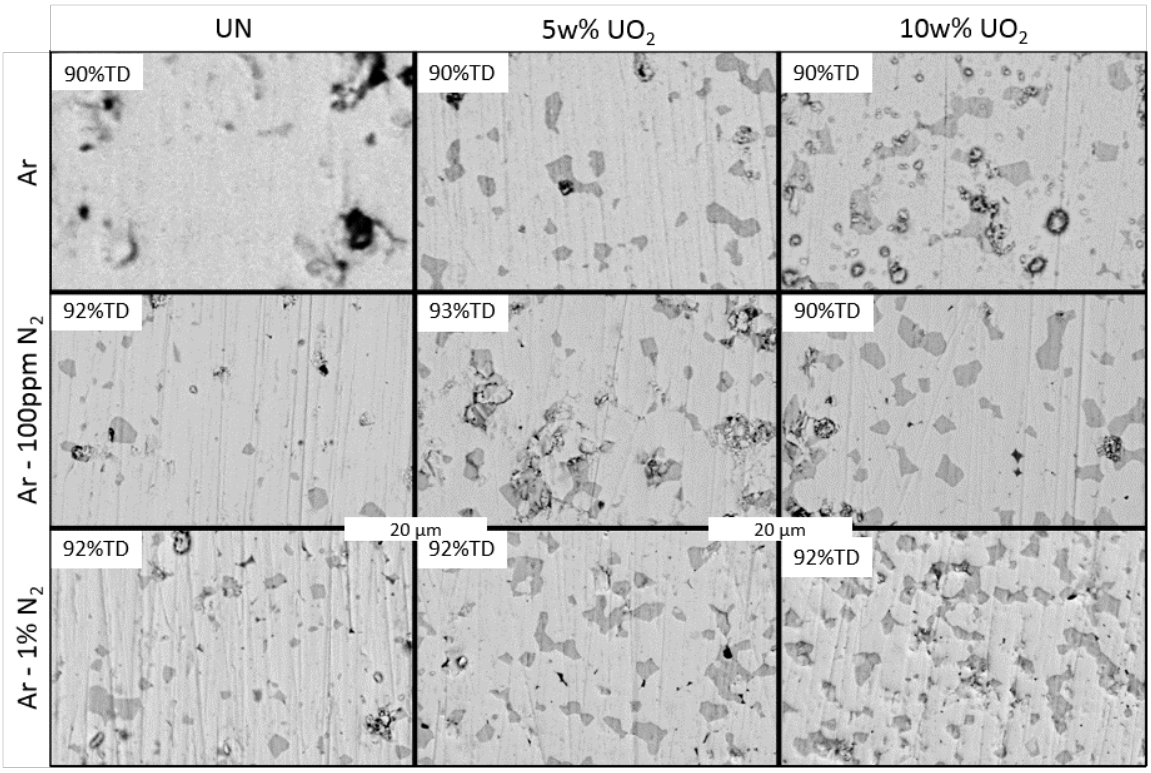

Figure 3.6 BSE SEM images of the microstructures of UN (left) and UN-UO_2 composite (center and right) pellets showing the effects of nitrogen concentration on phase formation during sintering for 5 hours at 1900 °C. In each case, the density was determined using Archimedes' principle in water.

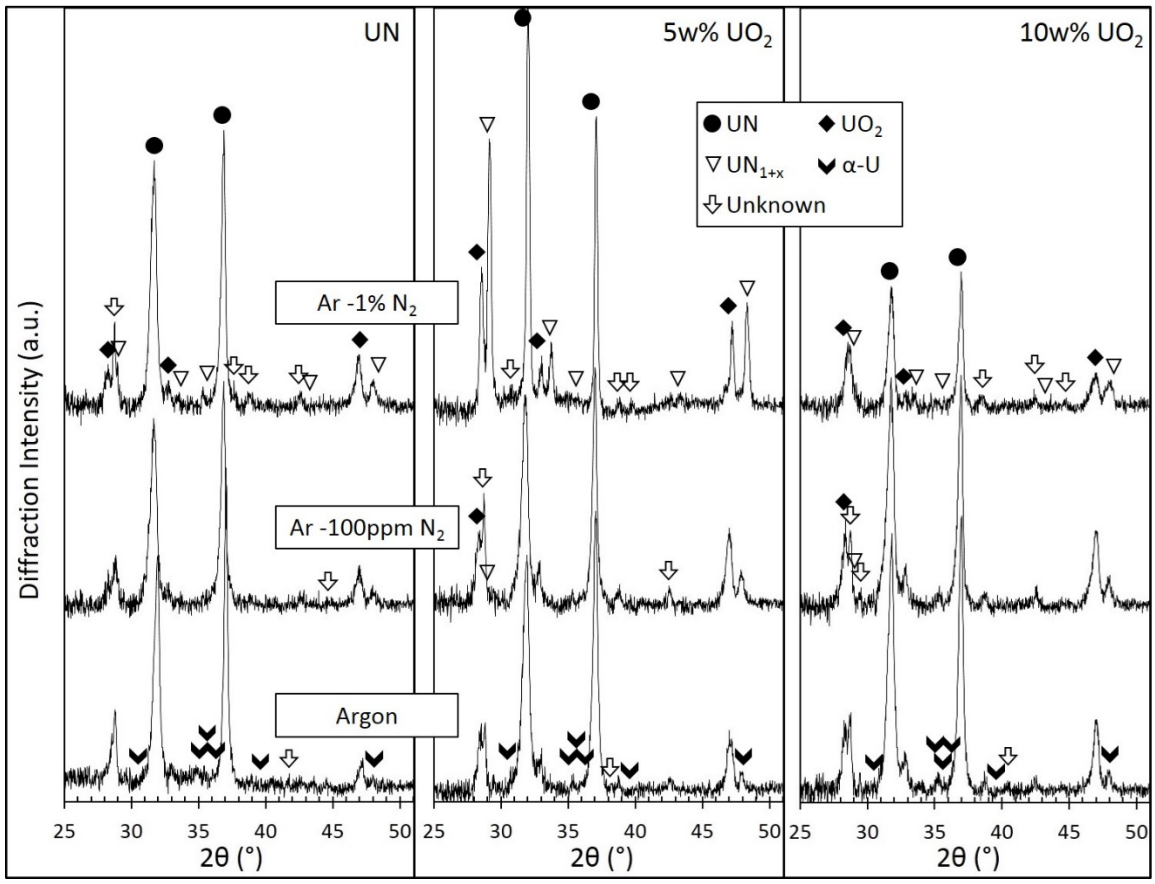

Figure 3.7 X-ray diffraction showing the effects of nitrogen concentration on phase formation after sintering UN (left) and UN-UO_2 composites (center and right) for 5 hours at 1900 °C.

Figure 3.8 BSE SEM images of the microstructures of UN (left) and UN - UO_2 composite (center and right) pellets showing the coarsening of features and increase of porosity with increasing temperature. All samples were sintered for 5 hours in Ar - 100 ppm N_2 and densities were determined using Archimedes' principle in water.

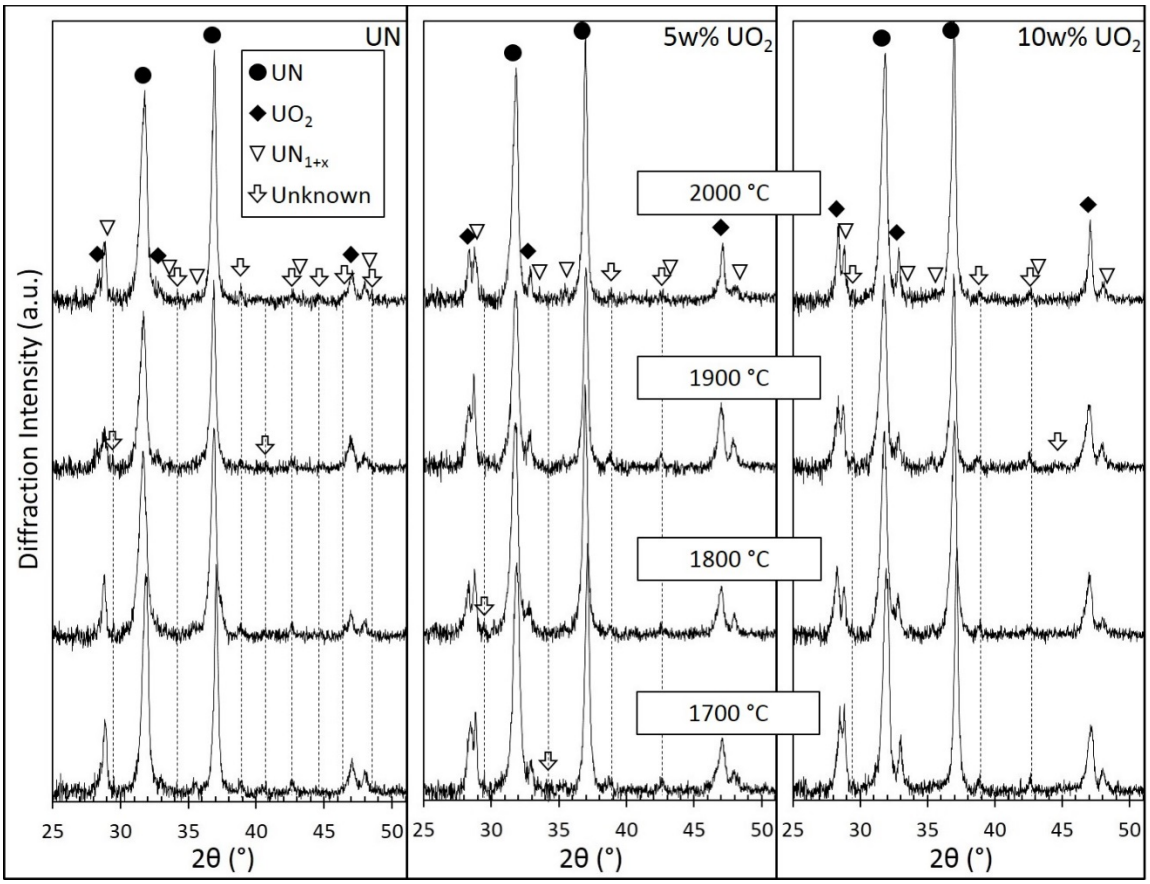

Figure 3.9 X-ray diffraction showing the effects of temperature on the phase formation after sintering UN (left) and UN-UO_2 composites (center and right) for 5 hours in Ar - 100 ppm N_2.

CHAPTER FOUR: HIGH TEMPERATURE OXIDATION KINETICS OF DYSPROSIUM PARTICLES

This chapter has been accepted to the *Journal of Alloys and Compounds*.

High Temperature Oxidation Kinetics of Dysprosium Particles

Brian J. Jaques[a,b]

Darryl P. Butt[a,b]

Accepted for publication in:

Journal of Alloys and Compounds

March 2015

[a]*Department of Materials Science and Engineering, Boise State University,*

1910 University Drive, Boise, ID 83725.

[b]*Center for Advanced Energy Studies,*

995 University Blvd, Idaho Falls, ID 83415.

Abstract

Rare earth elements have been recognized as critical materials for the advancement of green technology. Recently, the United States has invested 100s of millions of dollars to enhance, protect, and forecast their production and management. The work presented here attempts to clarify the limited and contradictory literature on the oxidation behavior of the rare earth metal, dysprosium. Dysprosium particles were isothermally oxidized from 500 - 1000 °C in N_2 - (2, 20, and 50%) O_2 and Ar - 20% O_2 using simultaneous thermal analysis techniques. Two distinct oxidation regions were identified at each isothermal temperature in each oxidizing atmosphere. Initially, the oxidation kinetics are very fast until the reaction enters a slower, intermediate region of oxidation. The two regions are defined and the kinetics of each are assessed to show an apparent activation energy of 8 - 25 $^{kJ}/_{mol}$ in the initial region and 80 - 95 $^{kJ}/_{mol}$ in the intermediate oxidation reaction region. The effects of varying the oxygen partial pressure on the reaction rate constant is used to show that dysprosium oxide (Dy_2O_3) generally acts as a p-type semiconductor in both regions of oxidation (with an exception above 750 °C in the intermediate region).

Keywords: Dysprosium, Oxidation, Kinetics, Gas-solid reactions, Rare earth alloys and compounds, Corrosion

4.1 Introduction

Global interest in rare earth element production and management has significantly increased in the past few years. In the year 2008, nearly $190 million worth of rare earth materials were imported and used in the U.S. alone. Such “strategic materials” are sought after for use in metallurgical applications and alloys, electronics, catalysts, and cathode ray tubes [1]. Compared to the light rare earth metals, relatively little published literature exists for praseodymium, promethium, thulium, lutetium, and dysprosium (also known as the heavy rare earths) although scientific interest in these metals is on the rise. In the next forty years, Hoenderdaal *et al.* [2] project that the demand for dysprosia (Dy_2O_3) and other dysprosium compounds will increase to between 7-25 times (to 14-50 ktons) from the 2010 demand. Although dysprosium was once thought to be one of the scarcer elements available in the earth’s crust, it has recently been reported to be more abundant than once thought (5.2 $^{mg}/_{kg}$, which is greater than 44 other elements [3]), making its utility more available for emerging materials technologies.

According to Hoenderdaal *et al.* [2], the proposed increase in demand is due to the future of magnetic applications (electric motors) due to dysprosium’s exceptional magnetic moment of 10.8 Bohr magnetrons, which is second only to holmium [3], and its ability to induce coercivity as an alloying agent or dopant [3, 4]. However, the demand for dysprosium has become more prevalent in other applications due to its many other interesting properties. For instance, dysprosium’s isotopes strongly absorb neutrons, which lead to its use in nuclear reactor control rod moderator materials [3, 5-7], and Dy_2O_3 has been considered as a substitute for SiO_2 in high-k dielectric applications due to its large band gap (4.9 eV) and dielectric constant (14) [8, 9]. Additionally, dysprosium

mononitride (DyN) has been postulated as a suitable surrogate for americium mononitride (AmN) due to its similar physical and chemical attributes in studying its sintering and alloying effects in spent nuclear fuel reprocessing [10-15]. DyN has also been investigated as a material for ferromagnetic and semiconductor superlattice structures for spintronic applications [16-18].

Although a few manuscripts and reports were published in the late 1950s and 1960s on the oxidation behavior of dysprosium [19-22], the experiments were performed on monolithic samples (rather than powders or particles) and the results appeared to be contradictory. Of particular interest in this study is the high temperature oxidation kinetics of elemental dysprosium in the temperature range of 450 - 1000 °C in N_2 - (2%, 20%, and 50%) O_2 and Ar - 20% O_2 using simultaneous thermal analysis techniques. An understanding of the oxidation kinetics of dysprosium has a wide range of implications ranging from semiconductor and electronics applications, to “green” energy and electric motor (magnetic) applications, to nuclear power generation applications.

4.2 Experimental Details

The starting material used to study the high temperature oxidation kinetics of dysprosium were dysprosium particles (99.7% purity, ESPI) sieved through a 40 mesh (420 μm) sieve (Figure 4.1). The particles had a surface area of 0.196 ± 0.058 m^2g^{-1}, as determined by nitrogen adsorption Brunauer-Emmett-Teller (BET) techniques. The particles were characterized using X-ray diffraction (XRD) with a $Cu_{K\alpha}$ source, as shown in Figure 4.2. Additionally, minor concentrations of iron, yttrium, terbium, and tungsten (<10 ppm total) were identified in the starting material using a Thermo XSeries II quadrupole inductively coupled plasma mass spectrometry (ICPMS).

Oxidation experiments were performed using a high resolution simultaneous thermal analyzer (Netzsch STA 449), which is capable of collecting thermogravimetric analysis (TGA) and differential scanning calorimetry (DSC) data simultaneously. Approximately 30 mg of the dysprosium particles (sealed and stored in an argon filled glovebox) were loaded into an 85 μL alumina combustion crucible, which was immediately loaded in the STA furnace. A vacuum purge cycle was started using an oxygen-gettered ultra high purity (UHP) argon gas (<1 ppb oxygen). Once the chamber was fully purged, the thermal profile was started. The four process gases used for the oxidation studies presented in this manuscript were certified mixtures of N_2 - (2%, 20%, and 50%) O_2 and Ar - 20% O_2.

Non-isothermal oxidation data were first collected to determine suitable parameters to study the isothermal oxidation behavior. In the non-isothermal experiments, the furnace was ramped at 20 $^{°C}/_{min}$ to 1100 °C in a gas flow rate of 100 $^{mL}/_{min}$ while TGA and DSC data were collected. Each data set was replicated at least twice and the results were averaged. Isothermal oxidation experiments were completed in each of the atmospheres from 500 - 1000 °C. In each case, the temperature of the furnace was allowed to equilibrate for 5 minutes at the desired temperature prior to introducing the oxidizing atmosphere and the dysprosium particles were oxidized to completion. Each isothermal oxidation experiment was repeated 3 - 4 times. The isothermal oxidation data were averaged together and then the average mass gain was normalized by subtracting the initial mass gain (which was less than 0.1% in all cases). To account for geometry, the data was then divided by the maximum mass obtained and then multiplied through by the specific surface area (where the specific surface area is equal to the initial mass

multiplied by the surface area of the particles obtained from B.E.T., as described above). This allowed for a direct comparison of data and accurate kinetics analysis using the specific mass gain with units of $\mu g/cm^2$.

4.3 Results and Discussion

Dysprosium is reported to have a hexagonal close packed (HCP) crystal structure and a melting temperature of 1412 °C [3], although there also exists two other allotropes: a low temperature (< -187 °C) orthorhombic phase (Cmcm) and a high temperature (> 1381 °C) face-centered cubic (FCC) phase ($Im\bar{3}m$) [3]. As seen in Figure 4.2, the starting material for the oxidation studies presented here is primarily a HCP dysprosium phase (P63/mmc) with a small fraction of the high temperature FCC phase. The HCP and FCC cubic phases were identified using X-ray diffraction data from the International Centre for Diffraction Data (ICDD) database provided by Spedding *et al.* [23] and Curzon and Chlebek [24], respectively. Additionally, it is important to note that the diffraction peaks were slightly shifted from the reported positions (depicted by the diamonds and circles in Figure 4.2), which is discussed in more detail later in this manuscript. Although the authors understand that the geometry and morphology of the particles are not ideal for an oxidation kinetics study, the authors were unable to identify a vendor to provide single phase dysprosium particles (with minimal oxide). However, the dysprosium particles from ESPI were nearly single phase and had a low surface area, which reduced un-wanted oxidation during handling.

Figure 4.2 also shows a typical diffraction pattern obtained from a fully oxidized dysprosium sample in each of the atmospheres and temperatures investigated. The particular diffraction pattern shown is the result of oxidizing the dysprosium particles

completely in N_2 - 20% O_2 at 800 °C, which formed a cubic Dy_2O_3 phase ($Ia\bar{3}$), as compared to data in the ICDD database provided by Swanson *et al.* [25]. Additionally, as shown by the inverted triangles, the oxide diffraction peaks agree well with the published values for Dy_2O_3. It is also worth pointing out that there are peaks in all of the oxide diffraction patterns that were not able to be indexed, as shown in Figure 4.2.

TGA and DSC data were simultaneously collected during non-isothermal oxidation of dysprosium particles in each of the atmospheres. The results are plotted in Figure 4.3. From this figure, it is seen that the oxidation behavior in N_2 - 20% O_2 and Ar - 20% O_2 is very similar throughout the entire reaction although the onset of the reaction in the nitrogen carrier gas occurs at a slightly greater temperature (approximately 20 °C). Also apparent in Figure 4.3 is that the TGA trace in the N_2 - 50% O_2 atmosphere begins very similar to the (Ar, N_2) - 20% O_2 but the kinetics slow and the TGA trace begins to deviate at a reaction percent of approximately 50% and 680 °C. The deviation increases with temperature and ultimately delays the complete oxidation of dysprosium in 50% O_2 to a temperature of 960 °C, which is approximately 100 °C greater than in 20% O_2. Additionally, the TGA trace from oxidation in N_2 - 2% O_2 follows similar behavior as the 20% O_2 atmospheres but the onset of the reaction occurs at a slightly higher temperature: the onset of oxidation in 2% O_2 occurs at 45 °C and 26 °C greater temperatures when compared to the argon and nitrogen carriers of 20% O_2, respectively. When comparing the DSC traces in each of the oxidizing atmospheres, there exists an exothermic peak at approximately 550 °C in all atmospheres except for the oxidation reaction in N_2 - 2% O_2.

The results of the non-isothermal experiments informed and subsequently lead to the region of study for the isothermal oxidation temperatures reported in the remainder of

this manuscript. As previously stated, isothermal oxidation experiments of dysprosium particles were completed 3-4 times at each temperature and atmosphere to arrive at average behaviors, which was used for the kinetics analysis. Figure 4.4 shows typical TGA data variability between duplicated oxidation experiments. In this figure, TGA data obtained from oxidizing dysprosium particles from 650 - 800 °C in N_2 - 20% O_2 are used to show the typical data variability, which is minimal. The variability that is present is due to the cumulative effects of several factors, including: irregular and non-uniform particle morphology (Figure 4.1), the presence of a slight amount of secondary phase in the starting material (Figure 4.2), the presumed presence of a native oxide and unquantified amounts of dissolved oxygen, the likelihood of residual stresses in the starting material due to vendor processing (as indicated by the slight leftward shift in the diffraction peaks when compared to the published values [23] shown in Figure 4.2), as well as the sampling technique used (i.e., a scoop sampling technique was used whereas a more effective and representative sampling technique could have been used, such as powder riffling). However, since multiple data sets were averaged for all of the analysis, the assumption is that the results are representative. It should also be noted that although the effects of particle size distribution will influence the kinetics of thermal oxidation, no effort was made in this investigation to de-convolute such effects other than to account for the starting surface area and a nominal shrinking core.

Figure 4.5 shows the isothermal oxidation behavior of dysprosium particles in N_2 - 20% O_2 from 500 - 950 °C. Two interesting observations from Figure 4.5 are that there is a distinct inflection where the oxidation kinetics slow after some reaction extent, α, and the specific mass gain that is defined by the onset of the inflection increases with

isothermal oxidation temperature. The inflection, or transition from relatively rapid to slower oxidation, is seen more clearly in Figure 4.5b, which focuses on the first two minutes of the oxidation reaction. Similarly, an inflection in the mass gain rate is observed in the TGA data of all of the oxidizing atmospheres investigated, as seen in Figure 4.6 for each of the four oxidizing atmospheres at 700 and 800 °C. Note that all of the TGA traces approximately reach the same terminal specific mass gain of $5.1 \cdot 10^{-10}$ $\mu g/cm^2$ (which is nearly 4% less than the theoretical mass gain of the oxidation reaction). The cause of the difference is likely due to varying amounts of oxygen dissolution in the dysprosium prior to thermal treatments, as predicted by [26]. Additionally, each of the TGA traces in the initial region of oxidation exhibits nearly identical mass gain rates for each atmosphere; the primary difference being that the inflection, as previously discussed, occurs at a larger reaction extent with increasing isothermal oxidation temperatures.

As seen by the inflections shown in Figure 4.5 and Figure 4.6, the mechanism for oxidation appears to change after some reaction extent, which is affected by temperature and oxidation atmosphere. Accordingly, each of the regions were defined for individual kinetics assessment in each atmosphere and temperature. The two regions of differing oxidation behavior in each of the four oxidizing atmospheres are quantified in Figure 4.7 and labeled as the initial and intermediate regions. The initial region is defined by the onset of mass gain to the onset of the inflection and the intermediate region begins immediately after the inflection through a reaction extent of 95%, or a specific mass gain of $4.85 \cdot 10^{-10}$ $\mu g/cm^2$. The data points in Figure 4.7 correspond to the average reaction

extent defined at the end of the initial region to the beginning of the intermediate region and are nearly centered on the inflection in the mass gain data.

An interesting observation from Figure 4.7 is that the change in oxidation kinetics occurs at lower reaction extents (i.e., the initial oxidation region is a smaller percentage of the overall reaction) in the Ar - 20% O_2 oxidizing atmosphere when compared to the nitrogen carrier gases. Additionally, the oxidation reaction is nearly fully defined by the initial reaction region at temperatures equal to and greater than 900, 950, and 1000 °C in N_2 - 2% O_2, N_2 - 50% O_2, N_2 - 20% O_2, respectively, whereas the initial reaction region comprises only 30-40% of the oxidation reaction at the same temperatures in Ar - 20% O_2.

As previously stated, the published literature on the oxidation kinetics of dysprosium is limited; very few publications were found that describe the oxidation kinetics of bulk materials and none were found describing the behavior of powders or finely distributed particles. Of the literature found, the mechanism of the oxidation reaction is presumed to remain constant over the entire reaction at each temperature, contrary to the results presented here. In a report written by Love [20] in 1959, the rate of dysprosium oxidation was best fit to linear kinetics from 200 - 600 °C in clean air (nearly 20% O_2). However, in the late 1960s Pethe *et al.* [21] and Greene and Hodge [22] reported that the oxidation kinetics follow a parabolic model. Greene and Hodge present dysprosium oxidation in temperatures of 300 - 800 °C in clean air (N_2 - 20% O_2) and Pethe *et al.* from 500 - 800 °C in an atmosphere with an oxygen pressure of 100 Torr (13% O_2 at 1 atm total pressure).

In the work presented here, the isothermal oxidation (TGA) data in the initial and intermediate oxidation regions (as defined in Figure 4.7) at each temperature and atmosphere were individually fit to many different kinetic models to best determine the kinetics rate constant (*k*). The models considered included various nucleation models, geometric contraction models, diffusion models, and reaction order models; many of which are described by Khawam and Flanagan [27]. Each of the data sets were fit with each model and the model that best fit the majority of the isothermal oxidation data sets (as determined by a coefficient of determination, or R-squared parameter) was used for the kinetics analysis.

The initial regions of oxidation in each atmosphere was best fit using a contracting area model (also known as a contracting cylinder model), described by:

$$k_p t = 1 - (1 - \alpha)^{\frac{1}{2}} \quad (1)$$

where k_p is the parabolic rate constant in μg/s·cm^2, t is the isothermal oxidation time in seconds, and α is the reaction extent. As previously discussed, the reaction extent (α) was normalized to the maximum value observed after converting to a specific mass gain value with units of μg/cm^2. The contracting area model assumes that nucleation occurs rapidly at the surface of the dysprosium particles and the rate of oxidation is controlled by the resulting reaction interface progressing towards the center of the assumed cylinder [27]. This is a significant assumption considering the morphology of the starting material, as shown in Figure 4.1.

As seen in Figures 4.5, 4.6, and 4.7, the initial region of the oxidation reaction is confined to a relatively short time period, early in the progression of the overall reaction (less than 1 minute in all but the 2% O_2 atmosphere). Since the kinetics in this region are

fast, some of the models could only be fit to a few data points, whereas other models (especially in the intermediate region) are defined by many thousands of data points. As seen in Table 4.1, this fact does not seem to effect the correlation coefficient in the 2 and 50% oxygen containing gases, but the correlation coefficient begins to decrease below 700 °C in the N_2 - 20% O_2 atmosphere and above 700 °C in the Ar - 20% O_2 atmosphere. This may suggest a breakdown of the contracting area kinetics model that was empirically chosen, as previously discussed. In the case of the initial region (below 700 °C) of oxidation in the N_2 - 20% O_2 atmosphere, the model that best fits the TGA data was a nucleation model (the Avrami-Erofeyev (AE2) [27]). However, in the case of the initial region (above 700 °C) of oxidation in the Ar - 20% O_2, a better fit was not found.

In a similar manner as described above for the initial region kinetics, the best fit kinetics model in the intermediate region of the oxidation reaction in each of the atmospheres is the Ginstling-Brounshtein diffusion model (a deviation of the Jander model [27]), described by:

$$k_p t = 1 - \frac{2}{3}\alpha - (1-\alpha)^{\frac{2}{3}} \quad (2)$$

As seen in Table 4.2, the Ginstling-Brounshtein model correlates well to the oxidation data (TGA) in all atmospheres except for N_2 - 2% O_2, where geometric contraction models (in particular, a contracting area model) best fit the data.

Similar to the contracting area model used to describe the initial region of oxidation, the Ginstling-Brounshtein model is also a deceleratory model, suggesting that the rate of reaction slows as the reaction extent increases or the available area for reaction decreases. The reaction rate decreases due to the fact that the product layer increases with

reaction extent and results in an increasing diffusion distance for cations and/or anions, and thus, slowing the reaction.

In each case, the parabolic rate constant (k_p) was determined by plotting the kinetics model (equations 1 and 2) versus the isothermal reaction time and extracting the slope from a linear relation. As noted previously, the parabolic rate constants for each temperature and atmosphere are listed in Table 4.1 for the initial oxidation region kinetics and Table 4.2 for the intermediate oxidation region kinetics.

In order to determine an activation energy for the oxidation reaction in each of the oxidizing atmospheres, the rate constants were plotted using the Arrhenius relation:

$$k_p = Ae^{-\frac{E_a}{RT}} \tag{3}$$

where A is a pre-exponential factor, E_a is the activation energy for the rate limiting mechanism(s) of the oxidation reaction, R is the universal gas constant (8.3145 $^{J}/_{mol\text{-}K}$), and T is the absolute temperature in Kelvin. The Arrhenius behavior describing the oxidation of dysprosium particles in the four atmospheres investigated is shown in Figure 4.8 for the initial region of oxidation and in Figure 4.9 for the intermediate region. As shown in Figure 4.9b, unusual oxidation behavior was observed in the N_2 - 50% O_2 oxidation atmosphere where there exists a discontinuity in the reaction kinetics between 650 and 800 °C.

The oxidation rate constants in the initial region of the oxidation reaction were found to be much greater (5-6 orders of magnitude) with a lower apparent activation energy than those found for the intermediate region in each atmosphere. The activation energies in the initial region of oxidation for all of the atmospheres (except the N_2 - 2% O_2 atmosphere) were found to be approximately 24 $^{kJ}/_{mol}$ (Figure 4.8). The value might be

compared to the 38 $^{kJ}/_{mol}$ reported by Greene and Hodge [22], who reported the oxidation of monolithic dysprosium between 300 - 550 °C, but experimental details are lacking, which make comparisons difficult. Another interesting trend in Figure 4.8 is that samples in the N_2 - 50% O_2 atmosphere have a rate constant that is nearly twice that of those oxidized in the (Ar, N_2) - 20% O_2 atmospheres and more than 10 times that of those oxidized in the N_2 - 2% O_2 atmosphere. However, the activation energy in the initial reaction region in the 2% oxygen atmosphere was significantly lower, at 8 $^{kJ}/_{mol}$.

Additionally, the oxidation kinetics in the intermediate region of the oxidation reaction were all found to have an apparent activation energy between 80-90 $^{kJ}/_{mol}$ over the temperature range studied, with the exception of the discontinuity observed in the 50% oxygen atmosphere (Figure 4.9). The fact that the activation energy in the 2% oxygen atmosphere is slightly higher (90 $^{kJ}/_{mol}$ versus 80 $^{kJ}/_{mol}$) suggests that the mechanism for oxidation requires slightly more energy (e.g., temperature) than the higher oxygen concentration environments. In any case, these values are fairly similar to those presented by Greene and Hodge [22] and Pethe *et al.* [28] who described the overall kinetics of dysprosium oxidation using parabolic kinetics and determined an activation energy of approximately 105 $^{kJ}/_{mol}$. The discontinuity observed in the 50% oxygen atmosphere, which suggests an apparent activation energy of zero, is indicative of a spontaneous oxidation reaction but is suspected to be anomalous, but repeated, behavior.

In both of the initial and intermediate regions of the isothermal oxidation reaction, it appears that the carrier gas (containing 20% O_2) has minimal effects on the oxidation rate of dysprosium based on similar oxidation rate constants (argon results in a rate constant nearly double that observed in nitrogen) and apparent activation energies.

However, by comparing the non-isothermal oxidation behavior (Figure 4.3) and the selected isothermal behavior (Figure 4.6), it is clear that the argon carrier gas promotes more rapid overall oxidation kinetics. This is likely due to the fact that the argon carrier gas induces a transition into the intermediate stage of oxidation at an earlier reaction extent (Figure 4.7) than nitrogen atmospheres. Being that the transition occurs at a lower reaction extent suggests that the initial oxidation layer is thinner, reducing the diffusion length of the oxygen ions, and resulting in faster kinetics in the intermediate region, as observed in Table 4.2.

A brief, additional study investigating the effects of gas flow rate on the oxidation reaction was performed. In the study, the gas flow rate was increased from 100-250 $^{mL}/_{min}$ in an isothermal oxidation temperature range of 650-850 °C. The intermediate region reaction rate and the transition reaction extent (Figure 4.7) remained constant, but an effect on the initial region oxidation rate was observed. Although the trends were similar for the initial region oxidation rates, the reaction onset occurred more quickly and the rate of oxidation reaction increased with increased gas flow rate. The findings suggest that there is a time delay for the furnace reaction chamber to reach the nominal oxygen concentration of the gas stream. However, the fact that the transition reaction extent remained constant suggests that a critical volume or surface area must be consumed in order for the reaction mechanism to change.

To gain insight into the mechanism of dysprosium oxidation, it is helpful to understand the type of defects present in the oxide. Accordingly, Brouwer diagrams (also referred to as Kroeger-Vink plots [29]) were constructed in each of the identified oxidation regions using the three partial pressures of oxygen used to oxidize dysprosium.

As seen in Figure 4.10a, the log-log plot in the initial region of oxidation shows a nearly linear dependence of oxygen partial pressure on the rate constant for each temperature studied (600 - 800 °C). The slope gradually changes from +3/4 to +1 with increasing temperature. Due to the positive slopes over the entire range of temperatures, it is presumed that the oxide behaves as a p-type semiconductor and suggests that the oxidation mechanism is either due to diffusion of oxygen through interstitial sites or dysprosium through vacancies. However, the effects of oxygen pressure on the rate constant in the intermediate region of oxidation is more complicated. As seen in Figure 4.10b, which also shows nearly linear correlations, the slope changes from +1/5 to -1/5 from 550 - 850 °C, respectively, with a near zero slope at 750 °C. As was observed in the initial oxidation region, the positive slope suggests that the oxide acts as a p-type semiconductor in the lower temperature range and as an n-type semiconductor in the high temperature range, with competing defects counteracting each other's charge near 750 °C. An n-type semiconductor suggests that the oxidation mechanism is either due to diffusion of dysprosium through interstitial sites or oxygen through vacancies. Oxygen diffusion is more likely due to the very large size of the dysprosium ions. The n-type behavior was also observed by Tare and Schmalzried [30] from 667 - 860 °C while a later report by Lal and Gaur [31] suggests that Dy_2O_3 is a p-type semiconductor at 627 °C with a 0.011 $cm^{-2}V^{-1}s^{-1}$ hole mobility and 0.010 $cm^{-2}V^{-1}s^{-1}$ electron mobility. Pethe *et al.* [21] also notes that the parabolic rate constant remains constant (within the experimental error) from 1-13% O_2 at 600 °C. However, it is known that minor concentrations of impurities in the starting materials can significantly alter the semiconducting behavior of the oxide. Since impurity concentrations were neither identified nor quantified in

previously reported oxidation behavior, comparisons with the work presented here may not be valid. Further work in this area needs to be completed.

To provide further insight into the mechanism of oxidation, an inert marker experiment was performed. A thin gold wire was fixed to a monolithic dysprosium sample, which was subsequently oxidized in N_2 - 20% O_2 at 650 °C for 45 hours. The gold marker remained at the oxide/gas interface after oxidation, suggesting that growth occurs at the metal/oxide interface. This observation is consistent with the work of Pethe *et al.* who found similar behavior via an inert (silver) marker experiment at 800 °C. The results of the marker experiments suggest that when the oxide behaves as a p-type semiconductor, the primary defect mechanism is most likely the diffusion of oxygen via dysprosium vacancies in the oxide and when the oxide behaves as an n-type semiconductor, the primary defect mechanism is likely oxygen diffusion through oxygen vacancies in the oxide.

4.4 Conclusions

The high temperature oxidation of dysprosium particles in 2 - 50% oxygen atmospheres in both nitrogen and argon carrier gases was studied from 450 - 1000 °C using both non-isothermal and isothermal techniques. The results of this study have identified two distinct regions of oxidation in each of the four atmospheres investigated, termed the initial and intermediate stages. The reaction rates at 800 °C in the initial oxidation region in N_2 - 2% O_2, N_2 - 20% O_2, Ar - 20% O_2, and N_2 - 50% O_2, were found using a contracting area model as 10^{-7}*(3.77, 32.8, 31, and 60.2 g^2/cm^4s), respectively. The reaction rates at 800 °C in the intermediate oxidation region in N_2 - 2% O_2, N_2 - 20% O_2, Ar - 20% O_2, and N_2 - 50% O_2, were found using the Ginstling-Brounshtein diffusion

model as 10^{-11}*(15.5, 17.2, 33.2, and 9.87) g^2/cm^4s, respectively. The apparent activation energy was found to be much lower in the initial stages (8 $^{kJ}/_{mol}$ in 2% oxygen and 25 $^{kJ}/_{mol}$ in the 20 and 50% oxygen atmospheres) than in the intermediate stages (80 - 90 $^{kJ}/_{mol}$).

Insight into the defect mechanism limiting the kinetics of the oxidation reaction was provided by an inert marker experiment as well as identifying the effects of oxygen pressure on the kinetics rate constant via Kroeger-Vink diagrams. It was determined that oxide growth occurs at the metal/oxide interface, most likely via oxygen diffusion. With the exception of above 750 °C in the intermediate oxidation region, the oxide behaves as a p-type semiconductor. The conclusion drawn from the evidence provided is that the rate limiting oxidation mechanism is oxygen diffusion via dysprosium vacancies to grow at the Dy/Dy_2O_3 interface. In the cases where the oxide behaves as an n-type semiconductor, oxidation is primarily rate limited by oxygen ion diffusion via oxygen vacancies to the Dy/Dy_2O_3 interface. However, further studies are needed to better understand the effects of impurity types and concentrations on the semiconducting properties of the oxide layer.

Acknowledgements

The authors would also like to acknowledge Nicole Leraas and Kelci Lester for their contributions and helpful discussions.

References

[1] J.S. Thomason, R.J. Atwell, Y. Bajraktari, J.P. Bell, D.S. Barnett, N.S.J. Karvonides, M.F. Niles, E.L. Schwartz, From national defense stockpile (NDS) to strategic materials security program (SMSP): evidence and analytic support, in, Institute for Defense Analysis, 2010.

[2] S. Hoenderdaal, L.T. Espinoza, F. Marscheider-Weidemann, W. Graus, Can a dysprosium shortage threaten green energy technologies?, Energy, 49 (2013) 344-355.

[3] CRC Handbook of Chemistry and Physics, in: W.M. Haynes (Ed.), CRC Press/Taylor and Francis, Boca Raton, FL, 2014.

[4] B.T. Kilbourn, A Lanthanide Lanthology: Part I, A-L, Molycorp, Inc., Fairfield, NJ USA, 1993.

[5] H. Il Kim, M. Herman, S.F. Mughabghab, P. Oblozinsky, Y.O. Lee, Evaluation of neutron cross sections for a complete set of Dy isotopes, Nucl. Instrum. Methods Phys. Res. Sect. B-Beam Interact. Mater. Atoms, 266 (2008) 3513-3528.

[6] N. Dzysiuk, A. Kadenko, I. Kadenko, G. Primenko, Measurement and systematic study of (n,x) cross sections for dysprosium (Dy), erbium (Er), and ytterbium (Yb) isotopes at 14.7 MeV neutron energy, Phys. Rev. C, 86 (2012) 10.

[7] O.S. Youl, G.C. Sup, J. Chang, Evaluation of neutron cross sections of Dy isotopes in the resonance region, Journal of the Korean Nuclear Society, 33 (2001) 46-61.

[8] H. Saghrouni, S. Jomni, W. Belgacem, N. Hamdaoui, L. Beji, Physical and electrical characteristics of metal/Dy_2O_3/p-GaAs structure, Physica B-Condensed Matter, 444 (2014) 58-64.

[9] A. Cherif, S. Jomni, W. Belgacem, R. Hannachi, N. Mliki, L. Beji, Investigation of structural properties, electrical and dielectrical characteristics of A1/Dy_2O_3/porous Si heterostructure, Superlattices Microstruct., 68 (2014) 76-89.

[10] D.P. Butt, B.J. Jaques, D.D. Osterberg, B.M. Marx, P.G. Callahan, A.S. Hamdy, New routes to lanthanide and actinide nitrides, in: GLOBAL 2009: The Nuclear Fuel Cylcle: Sustainable Options and Industrial Perspectives, September 6, 2009 - September 11, 2009, Paris, France, 2009.

[11] B.J. Jaques, D.P. Butt, B.M. Marx, A.S. Hamdy, D. Osterberg, G. Balfour, Synthesis and characterization of actinide nitrides, in: GLOBAL 2007: Advanced Nuclear Fuel Cycles and Systems, September 9, 2007 - September 13, 2007, American Nuclear Society, Boise, ID, United states, 2007, pp. 591-596.

[12] B.J. Jaques, B.M. Marx, A.S. Hamdy, D.P. Butt, Synthesis of uranium nitride by a mechanically induced gas-solid reaction, Journal of Nuclear Materials, 381 (2008) 309.311.

[13] P.G. Callahan, B.J. Jaques, B.M. Marx, A.S. Hamdy, D.P. Butt, Synthesis of Dysprosium and Cerium Nitrides by a Mechanically Induced Gas-Solid Reaction, Journal of Nuclear Materials, 392 (2009) 121-124.

[14] M. Takano, A. Itoh, M. Akabori, K. Minato, Hydrolysis reactions of rare-earth and americium mononitrides, J. Phys. Chem. Solids, 66 (2005) 697-700.

[15] M. Takano, S. Tagami, K. Minato, T. Kozaki, S. Sato, Lattice thermal expansions of (Dy, Zr)N solid solutions, Journal of Alloys and Compounds, 439 (2007) 215-220.

[16] Y.K. Zhou, M.S. Kim, N. Teraguchi, A. Suzuki, Y. Nanishi, H. Asahi, Optical and magnetic properties of the DyN/GaN superlattice, Phys. Status Solidi B-Basic Res., 240 (2003) 440-442.

[17] T.B. Thiede, M. Krasnopolski, A.P. Milanov, T. de los Arcos, A. Ney, H.W. Becker, D. Rogalla, J. Winter, A. Devi, R.A. Fischeri, Evaluation of homoleptic guanidinate and amidinate complexes of gadolinium and dysprosium for MOCVD of rare-earth nitride thin films, Chem. Mat., 23 (2011) 1430-1440.

[18] X.J. Li, Y.K. Zhou, M. Kim, S. Kimura, N. Teraguchi, S. Emura, S. Hasegawa, H. Asahi, Magnetic and transport properties of ferromagnetic semiconductor GaDyN thin film, Chin. Phys. Lett., 22 (2005) 463-465.

[19] B. Love, Selection and evaluation of rare or unusual metals for application to advanced weapons systems. Part I: A literature survey, in, Wright Air Development Center, 1958.

[20] B. Love, Selection and evaluation of rare or unusual metals for application to advanced weapons systems. Part II: The metallurgy of yttrium and the rare earth metals, in, Wright Air Development Center, 1959.

[21] L.D. Pethe, H.B. Mathur, A.B. Biswas, Kinetics of oxidation of dysprosium metal in the temperature region 500-800 C, Indian Journal of Chemistry, 6 (1968) 156-158.

[22] N.D. Greene, F.G. Hodge, Oxidation characteristics of the lanthanide metals, Corrosion, 22 (1966) 206-216.

[23] F.H. Spedding, J.J. Hanak, A.H. Daane, High temperature allotropy and thermal expansion of the rare-earth metals, Journal of the Less-Common Metals, 3 (1961) 110-124.

[24] A.E. Curzon, H.G. Chlebek, The observation of face centred cubic Gd, Tb, Dy, Ho, Er and Tm in the form of thin films and their oxidation, Journal of Physics F (Metal Physics), 3 (1973) 1-5.

[25] H.E. Swanson, M.I. Cook, T. Isaacs, E.H. Evans, Standard X-ray diffraction powder patterns, in, U.S. Dept. of Commerce, National Bureau of Standards circular 539, Washington, DC, 1959.

[26] T.H. Okabe, K. Hirota, E. Kasai, F. Saito, Y. Waseda, K.T. Jacob, Thermodynamic properties of oxygen in RE-O (RE=Gd, Tb, Dy, Er) solid solutions, Journal of Alloys and Compounds, 279 (1998) 184-191.

[27] A. Khawam, D.R. Flanagan, Solid-state kinetic models: Basics and mathematical fundamentals, J. Phys. Chem. B, 110 (2006) 17315-17328.

[28] L.D. Pethe, H.B. Mathur, A.B. Biswas, High temperature oxidation kinetics of lanthanum metal, Indian Journal of Chemistry, 5 (1967) 427-429.

[29] A.S. Khanna, Introduction to high temperature oxidation and corrosion, ASM International, Materials Park, OH, 2002.

[30] V.B. Tare, H. Schmalzried, Ionic and electronic conductivity in some rare earth oxides, Zeitschrift fur Physikalische Chemie, Neue Folge, 43 (1964) 30-32.

[31] H.B. Lal, K. Gaur, Electrical conduction in non-metallic rare-earth solids, Journal of Materials Science, 23 (1988) 919-923.

Figures

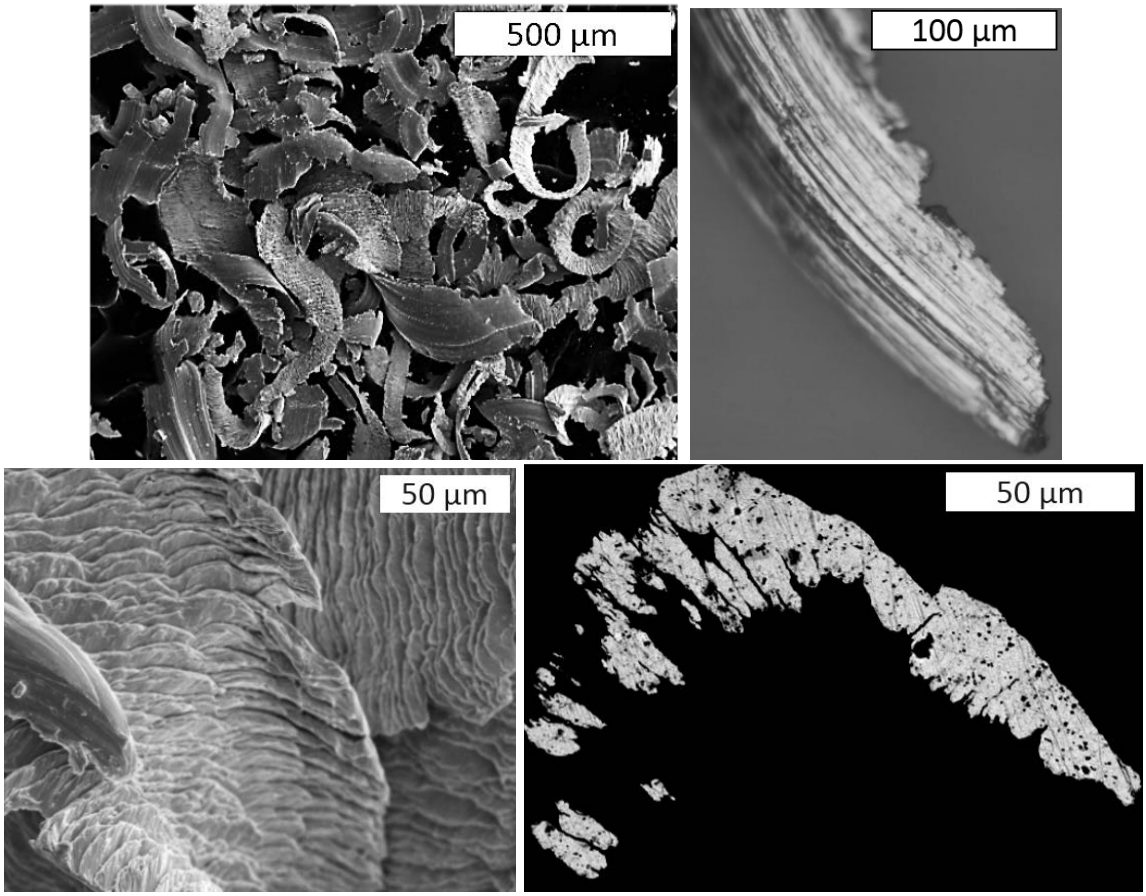

Figure 4.1 Images of the dysprosium particles used as the starting materials for the high temperature oxidation reaction study. The particles have a surface area of 0.196 ± 0.058 m^2g^{-1} as determined via gas adsorption techniques.

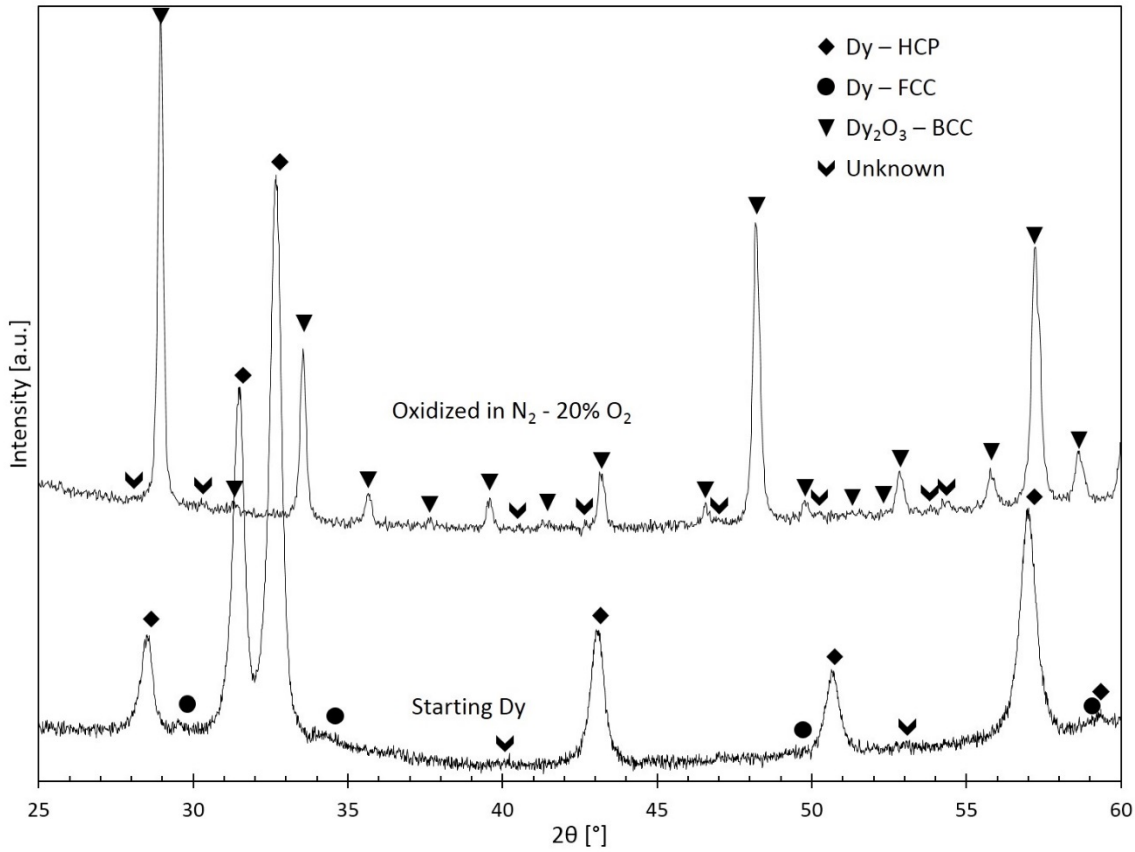

Figure 4.2 X-ray diffraction patterns of the dysprosium particles used as the starting material for the high temperature oxidation study and of a sample that was isothermally oxidized in N_2 - 20% O_2. As seen in the figure, the starting material is primarily a HCP dysprosium phase although there does exist a very small fraction of the FCC phase. The oxidized sample is a cubic Dy_2O_3 phase and is representative of all of the oxidized powder diffraction patterns (including all environments investigated here).

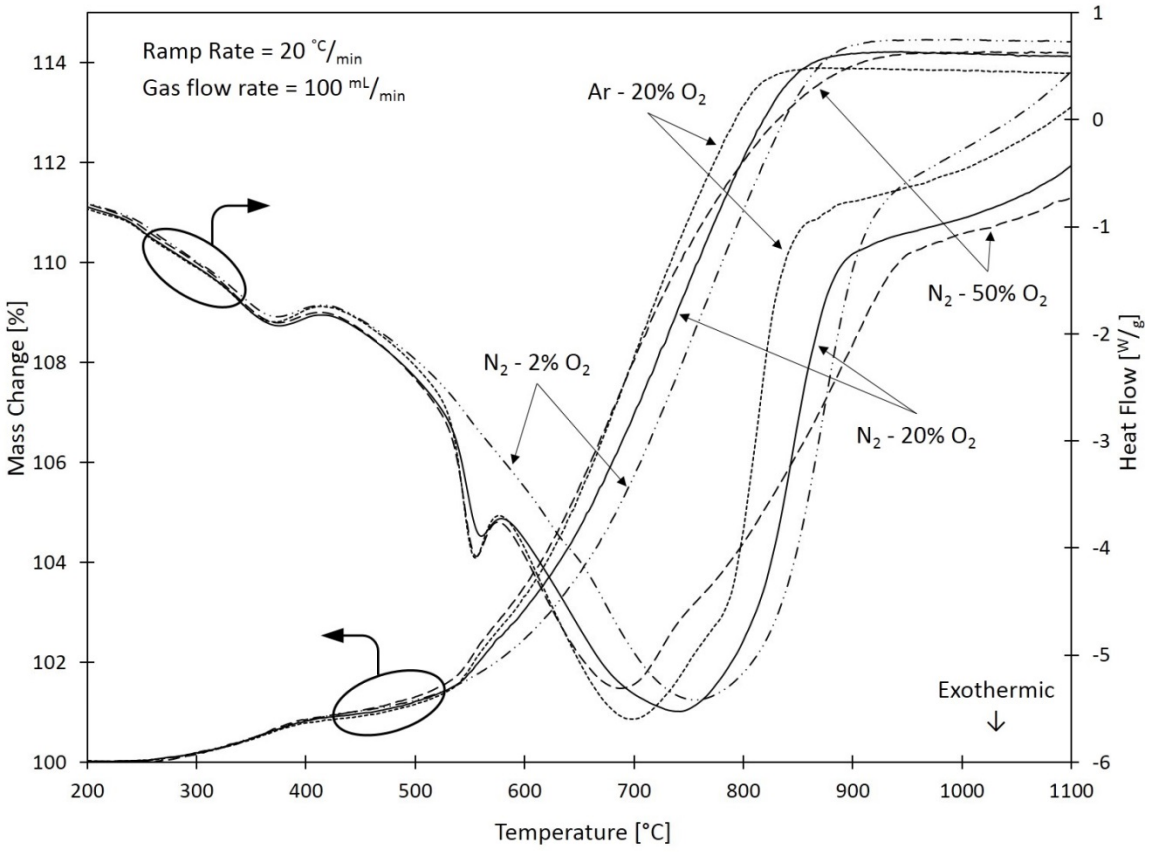

Figure 4.3 Non-isothermal oxidation traces of the oxidation of dysprosium particles. The simultaneous TGA and DSC behavior is shown for each of the oxidation atmospheres investigated (N_2 - (2, 20, or 50%) O_2 and Ar - 20% O_2).

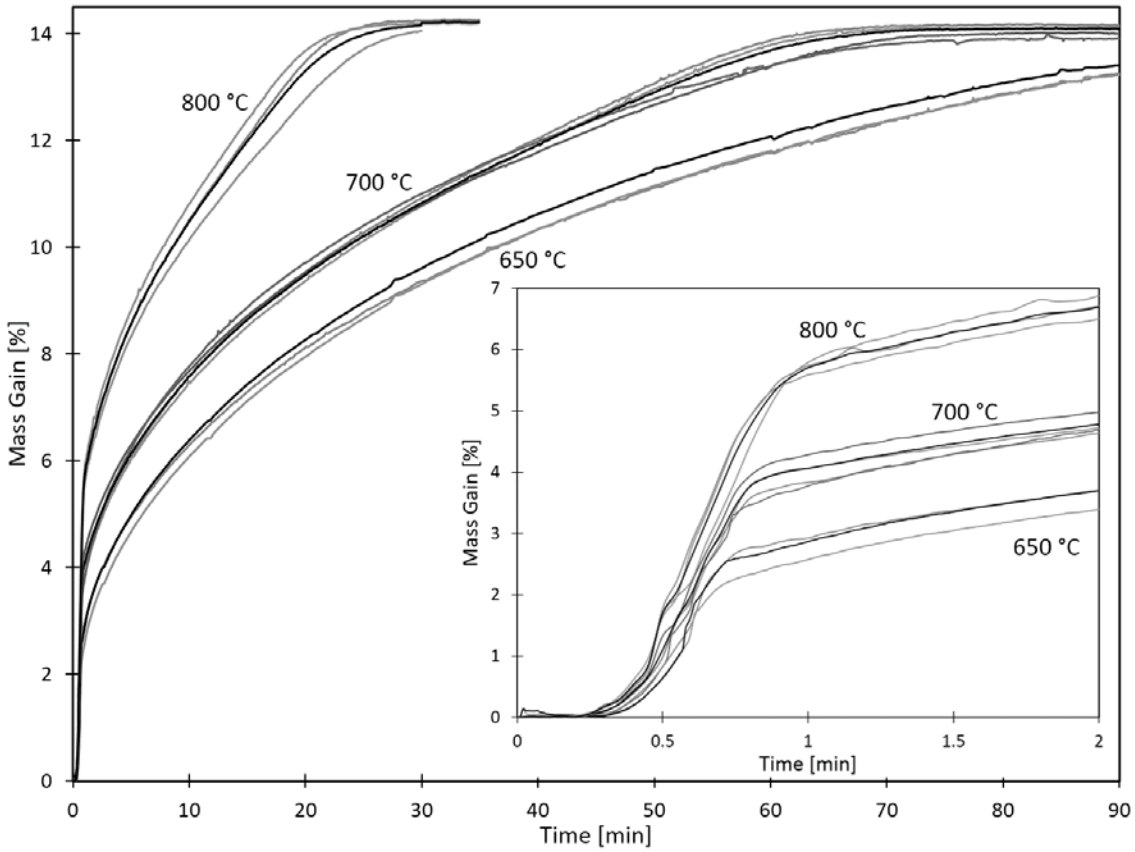

Figure 4.4 Typical isothermal TGA traces used for the kinetics assessment of the oxidation of dysprosium particles. The traces shown are of multiple runs at the indicated temperatures to show the variability of the data. Average curves were calculated and used for the subsequent kinetics assessment.

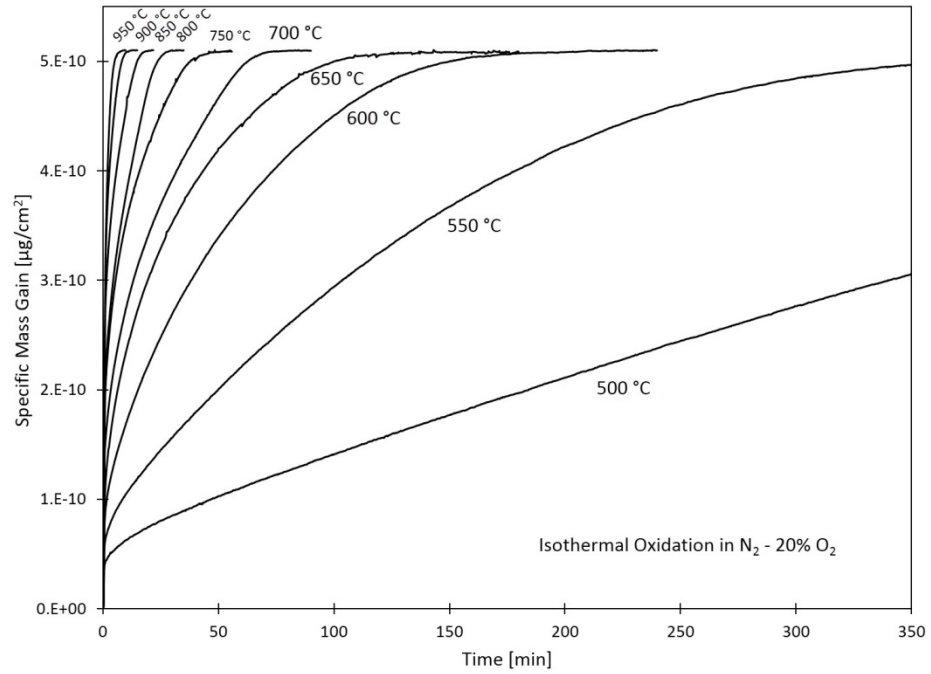

a)

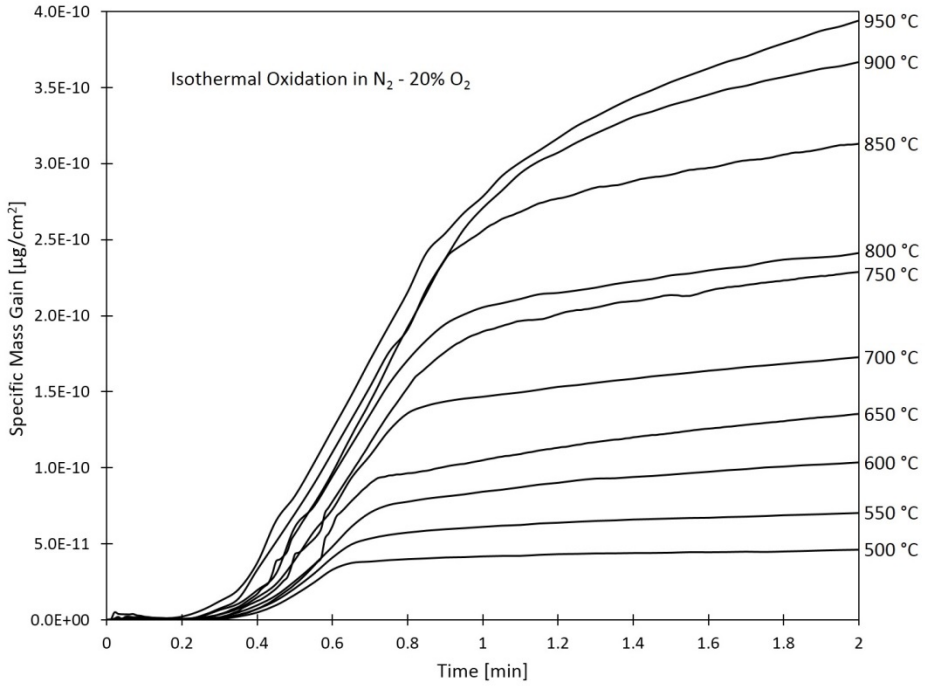

b)

Figure 4.5 Isothermal TGA traces describing the oxidation of dysprosium particles in clean air (N_2 - 20% O_2) from 500-950 °C. An inflection is observed in each data set at the beginning of the reaction (b) after an initial region of oxidation where the mechanism is presumed to change into an intermediate region of oxidation. Similar behavior occurs in each of the oxidation atmospheres investigated, as demonstrated in Figure 5.6.

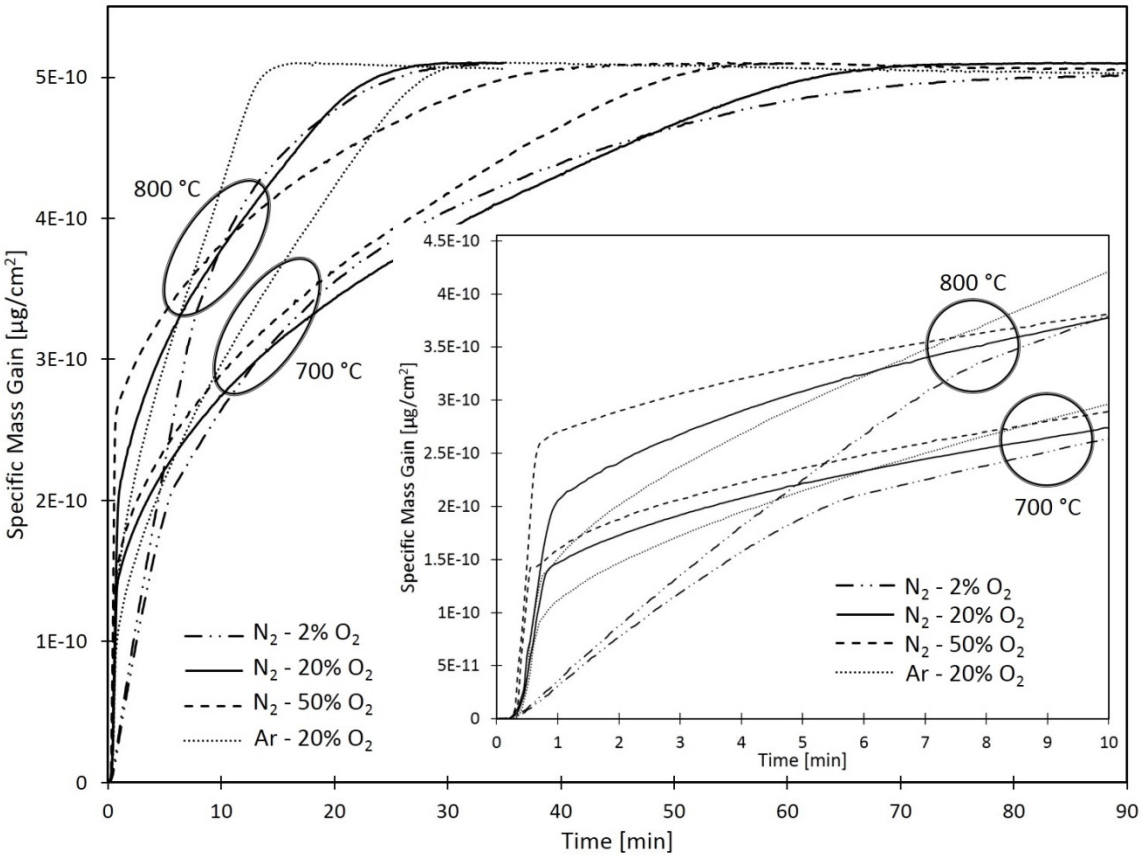

Figure 4.6 Isothermal thermogravimetric traces describing the oxidation of dysprosium particles at 700 and 800 °C in each of the atmospheres investigated (N_2 - (2, 20, or 50%) O_2 and Ar - 20% O_2).

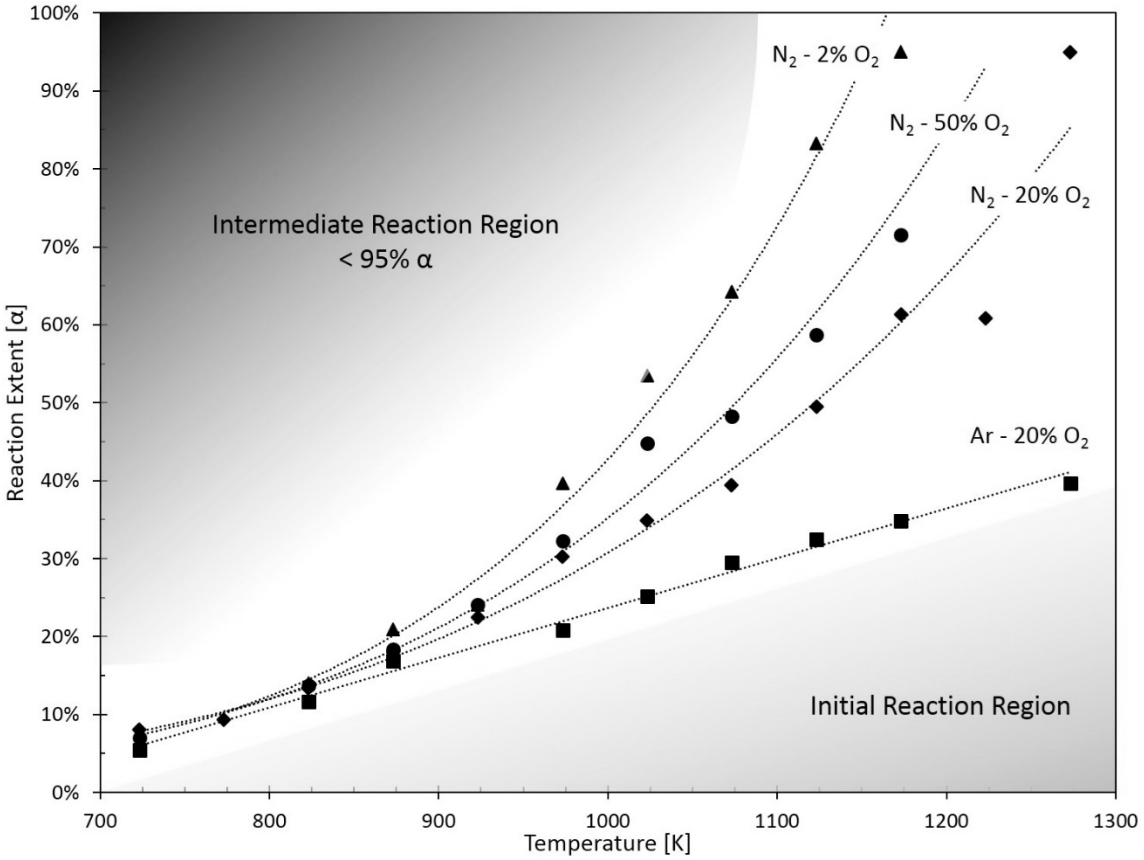

Figure 4.7 Plot showing the effect of isothermal oxidation temperature on the extent of reaction where the initial oxidation kinetics change to the intermediate kinetics of the oxidation reaction for each of the oxidation atmospheres investigated (N_2 - (2, 20, or 50%) O_2 and Ar - 20% O_2).

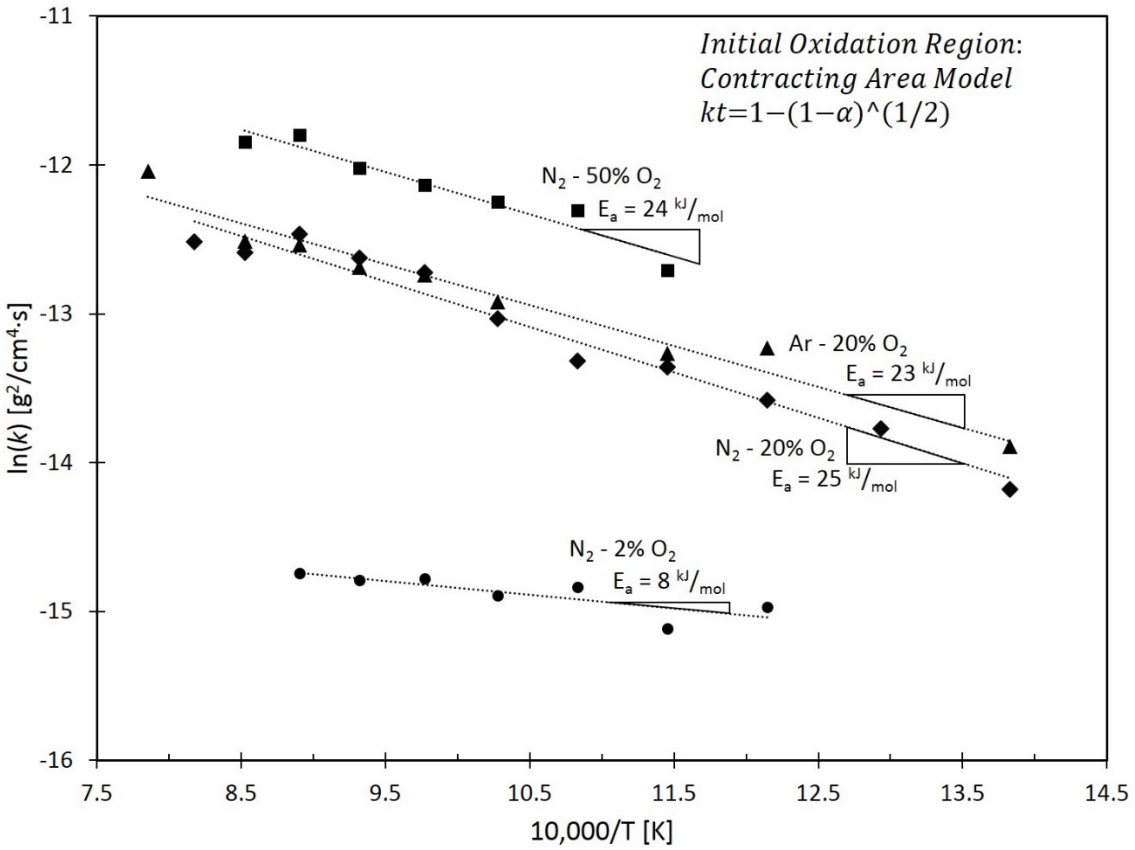

Figure 4.8 Arrhenius plot for the initial isothermal oxidation region of dysprosium particles in each of the atmospheres investigated using a contracting area kinetics model. The apparent activation energy is calculated from the linear relation and is labeled for each atmosphere.

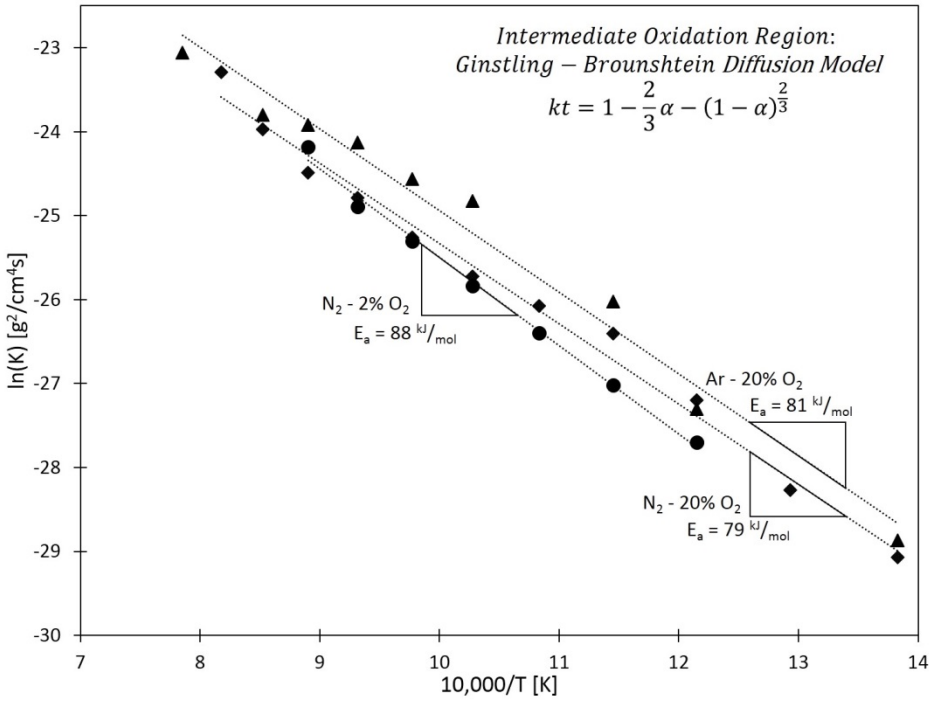

a)

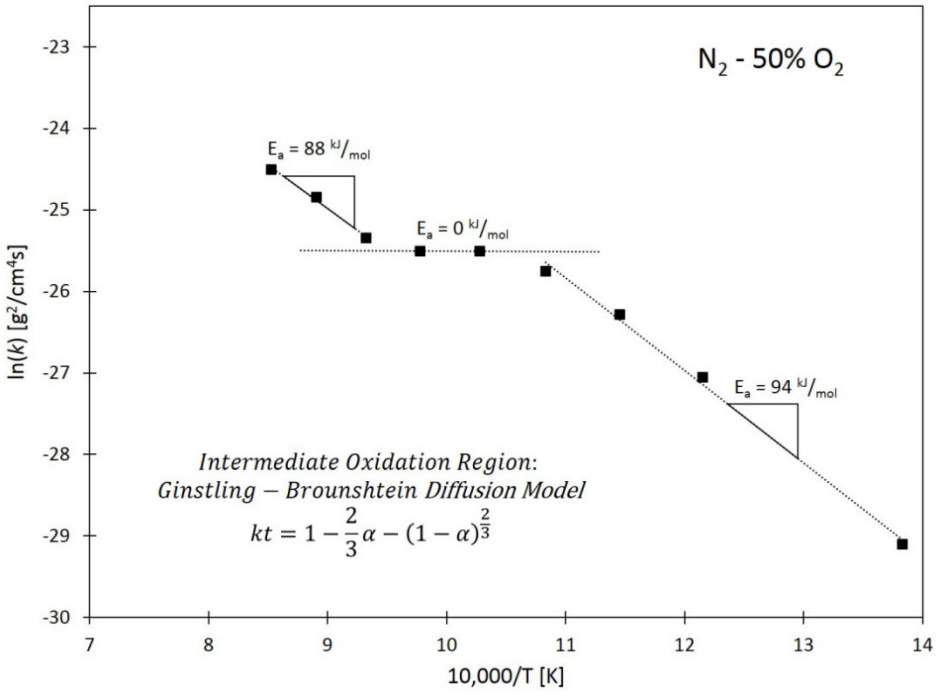

b)

Figure 4.9 Arrhenius plots for the intermediate isothermal oxidation region of dysprosium particles in each of the atmospheres investigated using Ginstling-Brounshtein diffusion model. The intermediate region of oxidation of dysprosium in N_2 - 50% O_2 was isolated from the others due to its interesting behavior, as seen in (b). In each case, the apparent activation energy is calculated from the linear relation and is labeled on each fit.

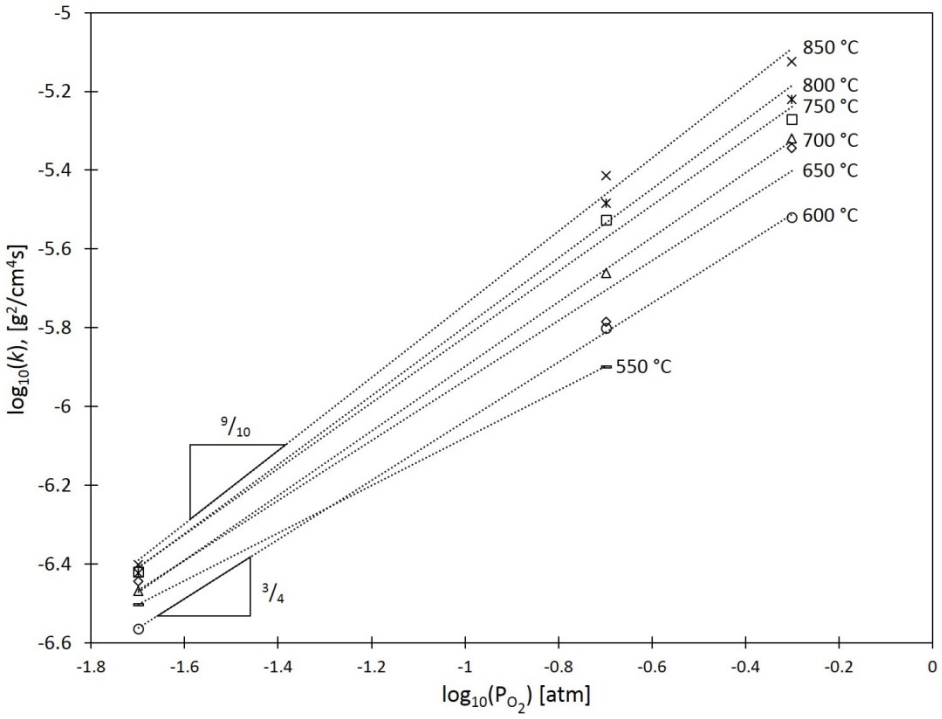

a)

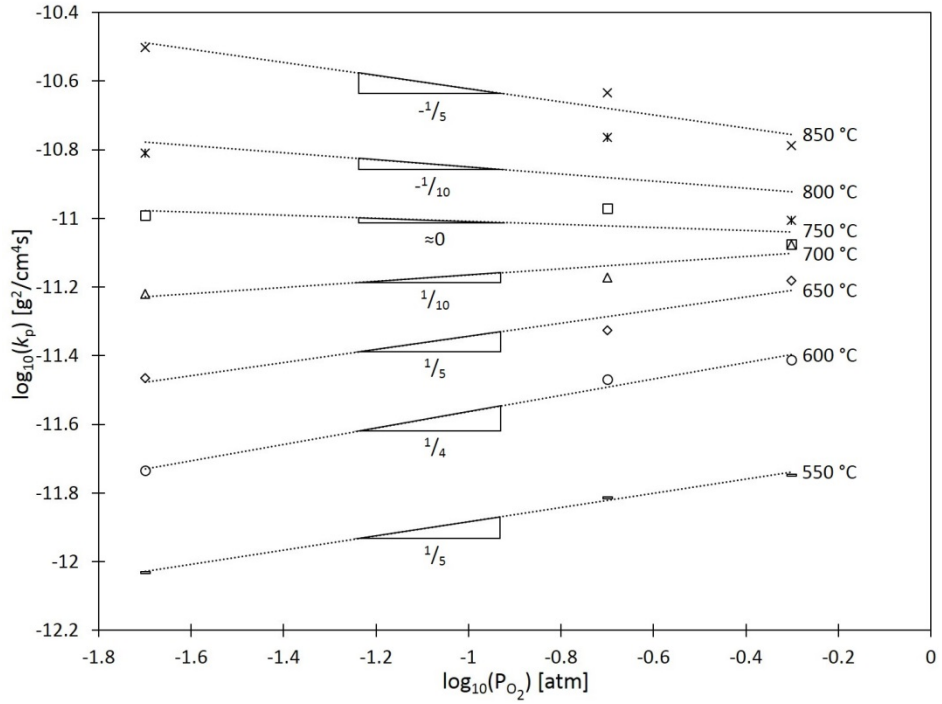

b)

Figure 4.10 Kroeger-Vink diagram of the isothermal oxidation of the dysprosium particles showing the dependence of oxygen partial pressure (with a nitrogen carrier gas) on the rate constant in the initial (a) and intermediate (b) regions of oxidation, as described in Figure 5.7. The slopes for each linear fit are identified and provide insight into the oxidation mechanism.

Tables

Table 4.1 Parabolic rate constants and correlation coefficients (R-squared values) for the fits of the oxidation kinetics in the initial oxidation region for all atmospheres using a contracting area model.

	N_2 - 2% O_2		N_2 - 20% O_2		N_2 - 50% O_2		Ar - 20% O_2	
Temp (°C)	k_p $*10^{-7}$ g^2/cm^4s	R^2	k_p $*10^{-7}$ g^2/cm^4s	R^2	k_p $*10^{-7}$ g^2/cm^4s	R^2	k_p $*10^{-7}$ g^2/cm^4s	R^2
1000	-		-		-		58.9	0.982
950	-		36.6	0.999	-		-	
900	55.1	0.994	34.0	0.999	71.7	0.991	36.9	0.987
850	3.96	0.997	38.6	0.999	75.1	0.990	35.9	0.980
800	3.77	0.999	32.8	0.996	60.2	0.994	31.0	0.973
750	3.81	0.998	29.8	0.988	53.6	0.998	29.3	0.957
700	3.40	0.997	21.8	0.956	48.0	0.998	24.5	0.988
650	3.60	1.000	16.4	0.986	45.2	1.000	-	
600	2.72	0.998	15.8	0.976	30.2	0.990	17.3	0.992
550	3.15	0.998	12.6	0.970	-		17.9	0.993
500	-		10.5	0.969	-		-	
450	-		6.96	0.979	-		9.27	0.985

Table 4.2 Parabolic rate constants and correlation coefficients (R-squared values) for the fits of the oxidation kinetics in the intermediate oxidation region for all atmospheres using the Ginstling-Brounshtein diffusion model.

	N_2 - 2% O_2		N_2 - 20% O_2		N_2 - 50% O_2		Ar - 20% O_2	
Temp (°C)	k_p $*10^{-12}$ g^2/cm^4s	R^2	k_p $*10^{-12}$ g^2/cm^4s	R^2	k_p $*10^{-12}$ g^2/cm^4s	R^2	k_p $*10^{-12}$ g^2/cm^4s	R^2
1000	-		-		-		96.8	0.992
950	-		76.8	0.982	-		-	
900	-		38.8	0.989	22.9	0.970	46.0	1.000
850	31.5	0.978	23.2	0.990	16.3	0.971	41.0	0.995
800	15.5	0.972	17.2	0.997	9.87	0.980	33.2	0.995
750	1.02	0.975	10.7	0.977	8.40	0.988	21.5	0.995
700	6.04	0.959	6.73	0.992	8.37	0.997	16.6	0.999
650	3.42	0.966	4.72	0.976	6.59	0.996	-	
600	1.84	0.984	3.40	0.992	3.87	0.995	5.00	0.995
550	0.93	0.994	1.54	0.992	1.79	0.995	1.39	0.991
500	-		0.528	0.990	-		-	
450	-		0.237	0.996	0.231	0.993	0.290	0.998

CHAPTER FIVE: CONCLUSIONS

Unlike traditional Materials Science and Engineering dissertations, the work presented in the preceding chapters encompasses diverse reactions in multiple materials systems; however, the commonality between each chapter is a discussion and understanding of a form of chemical reaction kinetics. This dissertation displays a broad understanding of the effects of atmosphere, time, and energy input (thermal and mechanical) in various gas-solid and solid-solid reactions. Accordingly, Chapter Two presents work in which mechanical energy is used to synthesize a high temperature ceramic, DyN and Chapters Three and Four both present work in which thermal energy is used to form high temperature ceramics (UN and Dy_2O_3, respectively). Additionally in Chapter Three, the effects of thermal energy and atmosphere on solid-solid reaction kinetics in the sintering UN and UN-UO_2 composites were investigated. The perceived understanding of gas-solid and solid-solid reaction kinetics presented in each chapter were also noteworthy contributions to the scientific community and warranted communication in peer-reviewed journal publications. Although each chapter (and publication) presents inclusive conclusions, this section is aimed to demonstrate commonality.

Chapters Two and Four both present gas-solid interactions between dysprosium and a non-metal, nitrogen and oxygen, respectively. Although possessing desirable attributes for many industrial applications, the behavior of dysprosium and dysprosium

compounds in any environment is not well documented in the literature and very limited thermodynamic data is available. Not only is the behavior of dysprosium in the presence of nitrogen investigated in Chapter Two, but the kinetics of a novel gas-solid synthesis technique is presented. Unlike traditional gas-solid reaction studies, mechanical energy was provided by a planetary ball mill to allow the reaction to proceed. The kinetics of the reaction were monitored using *in situ* temperature and pressure data to calculate the nitrogen consumption, which to the best of the author's knowledge has never been presented for *any* element in the literature to date. Additionally, the dysprosium-nitrogen system is an excellent system to deduce milling effects during reactive milling since no known intermediate phases to DyN exist. From the work presented in Chapter Two and the Appendix, the rate of the nitridation reaction of dysprosium is presumed to be limited by the creation of fresh, reactive surfaces that catalyze the dissociation of diatomic nitrogen and allow for the spontaneous formation of DyN. The rate of creation of such fresh surfaces can be controlled by the milling intensity or the number of media, which are both related to the number of impacts per unit time.

Similar to Chapter Two, Chapter Four focuses on the behavior of dysprosium in the presence a non-metal. However, Chapter Four uses thermal energy to allow the oxidation reaction to proceed rather than mechanical energy. The high temperature oxidation of dysprosium was studied in 2 - 50% oxygen atmospheres in both nitrogen and argon carrier gases at temperatures ranging from 450 - 1000 °C. The gas-solid reaction kinetics were monitored using *in situ* mass changes collected by a simultaneous thermal analzyer. The results of this study have identified two distinct regions of oxidation in each of the four atmospheres investigated, termed the initial and intermediate stages. The

kinetics of the gas-solid reaction in the initial and intermediate oxidation regions were best described using a contracting area model and a Ginstling-Brounshtein diffusion model, respectively. The parabolic rate constants were extracted and used to find apparent activation energies to be much lower in the initial regions (8 - 25 $^{kJ}/_{mol}$) than in the intermediate regions (80 - 90 $^{kJ}/_{mol}$). Additionally, insight into the defect mechanism limiting the kinetics of the oxidation reaction was inferred from the combination of an inert marker experiment and the dependence of oxide growth rate on oxygen pressure (Kroger-Vink plots). It was determined that oxide growth occurs at the metal/oxide interface, most likely via oxygen diffusion. With the exception of above 750 °C in the intermediate oxidation region, the oxide behaves as a p-type semiconductor. The conclusion drawn from the evidence provided is that the rate limiting oxidation mechanism is oxygen diffusion via dysprosium vacancies to grow at the Dy/Dy_2O_3 interface. In the cases where the oxide behaves as an n-type semiconductor, oxidation is primarily rate limited by oxygen ion diffusion via oxygen vacancies to the Dy/Dy_2O_3 interface. However, further studies are needed to better understand the effects of impurity types and concentrations on the semiconducting properties of the oxide layer.

Similar to Chapters Two and Four, Chapter Three presents a reaction between a metal and non-metal in a gas-solid reaction resulting in a ceramic powder. However, the difference being that thermal energy (rather than mechanical energy) is used to form a nitride (rather than an oxide). Accordingly, Chapter Three presents a reaction between uranium and nitrogen, forming UN, prior to sintering into a dense accident-tolerant fuel pellet. Although the thermal treatment was more complicated than that presented in Chapter Four, the overall reaction was similar. High purity UN was synthesized using a

hydride-dehydride-nitride synthesis route at high temperatures in various atmospheres consisting of hydrogen and nitrogen. The resulting UN powder was blended with 0, 5, and 10 w% UO_2 in a planetary ball mill creating a homogeneous and pyrophoric composite powder. Even the consolidated, green pellets were pyrophoric and prone to rapid oxidation upon exposure to air. UN and UO_2 composite pellets were sintered at 1900 °C for 5 hours in UHP-Ar, Ar - 100 ppm N_2 and Ar - 1 at% N_2 to gain insight into the effects of nitrogen on the stability of the nitride phases and distribution of oxides. Sintering in UHP-Ar resulted in a coring effect in which UN was dissociated to elemental uranium at grain boundaries, resulting in pronounced liquid-phase sintering and increased densification around the perimeter of the UN pellet. The addition of small amounts of UO_2 as well as nominally increased nitrogen in the sintering atmosphere resulted in finer microstructure, including nitride grains, oxide grains, and pores. Further studies were performed to assess the effects of sintering temperature in Ar - 100 ppm N_2 from 1700 - 2000 °C. In each case, U-O grains were homogenously distributed throughout the pellet microstructure and existed primarily on UN grain boundaries. Increasing UO_2 additions resulted in microstructure coarsening, as did the sintering temperature. Higher sintering temperatures also resulted in lower sintered densities, presumably due to a preferential formation of oxygen-stabilized nitrides or uranium oxynitrides. The work presented in Chapter Three demonstrates a viable synthesis process for fabricating carbon free UN-UO_2 accident tolerant fuels for the current fleet of LWRs. Although a new fuel concept has been developed, there is a lengthy process in order to demonstrate its improved accident tolerance. Further work must be completed to determine if controlled UO_2 additions enhance the accident tolerance of UN to high temperature oxygen and steam

exposures while maintaining thermophysical properties comparable or better than the benchmark LWR fuel, UO_2.

APPENDIX

Kinetics of the Nitridation of Dysprosium during Mechanochemical Processing

Kinetics of the Nitridation of Dysprosium during Mechanochemical Processing

This Appendix is published by Elsevier in *Journal of Alloys and Compounds* and should be referenced appropriately.

Reference:

G. A. Alanko. D. D. Osterberg, B. J. Jaques, M. F. Hurley, D. P. Butt, “Kinetics of the nitridation of dysprosium during mechanochemical processing.” *Journal of Alloys and Compounds.* **620** 413-420 (2015).

*This chapter includes modifications from the originally published version.

Kinetics of the Nitridation of Dysprosium During Mechanochemical Processing

Gordon A. Alanko[a]

Daniel D. Osterberg[a]

Brian J. Jaques[a]

Michael F. Hurley[a,b]

Darryl P. Butt[a,b]

Accepted for publication in:

Journal of Alloys and Compounds

January 2015

[a]*Department of Materials Science and Engineering, Boise State University, 1910 University Drive, Boise, ID 83725.*

[b]*Center for Advanced Energy Studies, 995 University Blvd, Idaho Falls, ID 83415.*

Abstract

Dysprosium nitride was synthesized by the reactive milling of the rare earth metal under 400 kPa nitrogen gas in a planetary ball mill. The nitrogen consumption rate was calculated from in situ temperature and pressure measurements to find the reaction extent as a function of milling time at milling speeds from 350-650 rpm. The results are analyzed in terms of a fundamental milling dynamics model in which the input milling energy is the primary driving force for reaction and the rate limiting step of the nitridation kinetics is the formation of chemically active surfaces. The model differs from traditional gas-solid reactions, which are often limited by diffusion of a species through a surface layer or by dissociation of the gas molecule. These results give fresh insight into reactive gas-solid milling kinetics.

Keywords: mechanochemistry; nitrides; rare earths; high energy ball milling; reaction kinetics

A.1 Introduction

Reactive milling is an adaptation of the high-energy ball milling techniques that have been used for materials processing for some 50 years [1]. In reactive milling, sometimes termed mechanochemical synthesis, the system is designed to use the energy imparted by the milling tools to assist in driving a chemical reaction. The reaction may be solid-solid, solid-liquid, or solid-gas. The latter is often applied in studies of hydrogen storage materials [2-4]. There has been some work done describing the kinetics of gas-solid reactions during reactive milling, in which observed kinetics have included nucleation accelerated by grain refinement in transition metal-doped MgH2 [3], autocatalysis/self-propagation in Zr and Hf hydrides [4], and nucleation and growth in HfN [5], ZrN [6], and ZrO2/ZrC [7, 8]. While many closed-form analytical models have been developed to describe the mechanical energy imparted during high energy milling [9-14], very few reactive milling investigations explicitly consider this energy while discussing reaction kinetics, and to the best of the author's knowledge no investigation has analyzed how the rate of energy transfer could change during reactive milling.

Reactive milling is interesting from both a fundamental standpoint and with a view to applications, as the self-contained, low temperature nature of the process could enable the synthesis of many materials that are difficult or hazardous to prepare [15-17] as well as reducing the environmental impact of synthesis [18].

A.1.1 Dysprosium and Dysprosium Nitride

Dysprosium, like the other rare earth metals, displays extreme reactivity on fresh surfaces with most gasses [19, 20]. An X-ray photoelectron spectroscopy study of the

reaction of nitrogen on clean dysprosium demonstrated that nitrogen dissociatively chemisorbs with the formation of one or two monolayers of nitride at 300 K [21]. Gas phase reactions arrested in frozen argon provide evidence for direct scisson of the N≡N bond by adjacent dysprosium atoms and do not indicate high complexation of the nitride by molecular nitrogen [22]. Similar behavior is observed for the early lanthanides [23] in contrast to the higher tendency of light transition [24] and some actinide [25] metals and nitrides to complex molecular nitrogen. Although the kinetics of the dysprosium nitridation reaction have not yet been reported in any detail, the demonstrated tendency for dissociative chemisorption over physisorption or dissolution of nitrogen suggests that the rate limiting step in the nitridation process will be either gas transport to the metal or through the nitride. This makes DyN an interesting model system for a reactive milling study: since milling is widely understood to break up and disperse surface films, nitride formation during reactive milling under a high nitrogen pressure might be expected to be kinetically limited by the formation of fresh chemically active surfaces rather than by transport mechanisms or nitrogen dissociation. A schematic of this proposed process is found in Fig. A.1a-c. The impact event diagrammed in Fig. A.1d is analyzed in terms of a kinematic model in order to determine the energy available for material refinement.

A.1.2 Ball Milling Modeling

The planetary ball milling model developed by Chattopadhay *et al.* [14] was used as a starting point for analysis of milling mechanics. The model includes assumptions that limit the applicability to the stochastic process of ball milling. Modeled media move in a no-slip condition, being governed by the normal force while “attached” to the vessel wall, by rigid body mechanics while not attached, and stick without slip on impact. Modeled

impact is described by Hertzian mechanics [26] and assumes perfectly elastic impacts rather than the elastic-plastic behavior found in real milling systems. Even considering these limitations, the milling model provides a helpful point of reference and was employed to extract the angular frequency dependencies of various process variables. The physical constants of the planetary ball mill and milling media used are provided in Table A.1, and the dependencies of impact conditions on milling speed are summarized in Table A.2. The kinetics analysis considered here is specific to counterrevolving planetary ball mills, although the analysis could be extended to other high-energy mill geometries by modifying the model.

Table A.1 Mill and Media Physical Constants

Mill parameters:			
Constant	**Symbol**	**Value**	**Units**
Vial/Disk speed	ω_v/ω_d	-2.00	
Disk radius	r_d	70.5	mm
Vial radius	r_v	37.5	mm
Corrected rv	$r_v' = r_v - r_b$	35.0	mm
Vial/Disk radius	r_v'/r_d	0.496	
Media parameters:			
Constant	**Symbol**	**Value**	**Units**
Radius	r_b	2.5	mm
Density	ρ_b	5.89	g/cm^3
Mass	m_b	0.3855	g
Poisson's ratio	υ_b	0.31	
Elastic modulus	E_b	234.8	GPa

Table A.2 Conditions At Media Impact (Modeled):

Angular Frequency Dependencies				
Variable	**Symbol**	**Coefficient**	**v^x**	**Units**
Deflection	δ_h	1.267	$v^{0.8}$	µm
Hertz radius	a_h	0.056	$v^{0.4}$	µm
Net velocity	V	0.286	v^1	$^m/_s$
Impact Energy	$E_b(v)$	0.056	v^2	$^{mJ}/_{hit}$

A.1.3 Energy Requirements for Surface Formation

The continual input of energy during milling media impacts leads to crystallite size reduction. The exact mechanism is debated and probably varies from system to system. In brittle materials, fracture is assumed to be dominant, while in ductile materials there is probably dislocation coalescence leading to dynamic recrystallization of new subgrains [27] that asymptotically approach a limiting size of 10-20 nm. This limit condition is different for each material and thought to be related to the cohesive strength and to the maximum dislocation stacking density [28]. Unfortunately, very few studies on ball milling of pure metals have reported the crystallite size as a function of milling time

[29, 30], while most studies report only ending crystallite size. The reduction of dimension with increasing milling energy dose is a well known relationship in mineral processing typically represented by the empirical laws of Rittinger, Kick, or Bond, which were proposed by Hukki [31] to be approximations to a size-dependent energy consumption of the general form:

$$dE = -C\frac{dx}{x^{f(x)}} \quad (1)$$

where x is the critical dimension of a comminuted material, C is a material constant, and f(x) describes some dependence of dE on the current size. Rittinger's law makes the approximation f(x) = 2 in Eq. 1 and predicts the energy required for size reduction in very small (< 10 μm) particles to be proportional to the area of new surface created. Fractal analysis has suggested f(x) = 2.3 + x ln(x) with x measured in micrometers [32]. Thus, reactions in milled systems that are kinetically limited by surface formation or surface reactions should be expected to display a linear or nearly linear dependence on the mechanical energy imparted to the reacting material.

Closed form milling theory based on Hertzian contact solutions generally assumes completely elastic impacts, although the obtained solutions are sometimes modified by a constant scalar to correct for an assumed value of the coefficient of restitution CR. In the case of normal impact with negligible spin, the energy state of the media after impact may be described solely by CR = vf/vi, $0 \leq CR \leq 1$. A value of 1 indicates a completely elastic impact as described by Hertzian impact theory, while a value of 0 represents completely plastic impact. In high energy milling, both theory and experiment call for values in the range 0.5-0.9. In general, the value of CR for a given media at a given moment depends on the thickness of material coating the media (and thus the volume

available for plastic deformation). In any attempt to accurately describe the kinetics of a reaction during high energy milling, it is imperative to quantify if and how the coefficient of restitution changes throughout the milling process.

A.2 Materials and Methods

A.2.1 Gas-Solid Reactive Milling Experiments

Milling experiments were conducted on a planetary ball mill (Retsch PM100, Haan, Germany) in a hardened steel vessel with a 250 mL nominal volume. The actual volume of the vessel + lid was measured to be 269.7 mL by measuring the amount of deionized water required to completely fill the vessel along with the gas ports in the milling lid. In a typical experiment, 5 g of dysprosium filings were added to the milling jar along with 184 yttria-stabilized zirconia 5 mm diameter milling media, resulting in a ball-to-powder charge of 14:1. The vessel was then sealed and purged with ultra-high purity nitrogen, purified further by by copper gettering, before pressurizing to 400 kPa nitrogen, which is greatly in excess of the 140 kPa required to fully convert 5g of Dy to DyN under the given experimental conditions. In a few experiments, the starting pressure was varied in the range 300-600 kPa without a noticeable effect on the reaction rate. Milling was conducted at speeds ranging from 350-650 rpm for 6 hr and at 500 rpm for between 15 min – 24 hr. Nitrogen consumption was monitored by pressure and temperature sensors mounted in the milling lid. As-milled powders were checked for phase purity by x-ray diffraction (Rigaku Miniflex, Tokyo, Japan). Full details of these experiments are currently being published in a concurrent manuscript by Jaques *et al.* [33].

A.2.2 Milling Media Energetics

Two experiments were performed on milling media coated by pure metals milled under argon for 0-24 hours and for media coated by metal-metal nitride composites formed by milling metal under nitrogen for 0-1 hours. The coefficient of restitution C_R was measured by removing media from the milling vial and dropping media 40 cm onto a milling jar lid, resulting in a maximum impact velocity of approximately 2 m/s. Vacuum tweezers were used to hold the media before dropping to avoid imparting spin. The rebound height was measured and the coefficient of restitution calculated by assuming that the relationship $mgh = 0.5mv^2$ held such that $C_R = (H_i / H_f)^{0.5}$. At least 20 trials were performed for each combination of material system and milling time. In addition, the amount of material coating the media and vessel walls was calculated for each system and milling time by weighing the free powder in the vessel, weighing the media, and calculating the quantities adhered to the media and vessel walls. The calculated mass of adhered dysprosium was then converted into an average thickness adhered to the media. The average thickness and surface roughness of the starting and coated media was verified by laser micrometery.

A.3 Results and Discussion

Reactive milling for a period of 6 hours at all milling speeds from 350-650 rpm was found to be sufficient for complete reaction of dysprosium with nitrogen to form DyN. Faster milling speeds required considerably less time. Representative XRD data is shown in Fig. A.2, showing the increasing formation of DyN with milling time and phase pure DyN after 6 hours of milling to within the detection limit of the XRD. The DyN crystal size calculated by the Scherrer equation is extremely small, ranging from 11 nm

down to 6 nm with increasing milling time as seen in Fig. A.2, inset. Similar to the HfN system, dysprosium metal was found to quickly adhere to the vessel walls and media after the start of milling, rendering calculation of the reaction extent from powder XRD data suspect [5]. X-ray diffraction analysis of the partially nitrided powders showed that the free powder at any point was primarily DyN with some dysprosium, and the material adhered to the media and vessel walls was primarily Dy with slight DyN. During reactive milling with nitrogen, adhered metal is reacted and breaks off as powder, as shown in Fig. A.3.

The coefficient of restitution is 0.90-0.94 for fresh 5 mm yttria-stabilized zirconia balls when impacting a hardened steel plate at approximately 2 m/s. When media were coated with dysprosium, the coefficient of restitution was found to decrease to 0.60-0.65. The exact value was found to depend on the thickness of the dysprosium layer, and with prolonged milling under argon the media were found to transfer significant quantities of dysprosium to the vessel walls and lid, resulting in an increase in C_R towards a limiting value of 0.82-0.85 for less than 20 μm thickness of metal. No effect of grain size or induced strain was found within the experimental error induced by adhered metal surface roughness. A similar behavior was found when milling dysprosium in nitrogen as shown in Fig. A.4, except that in this case metal was consumed to form nitride and the coefficient of restitution increased more rapidly during milling. As the metal was consumed, the media mass decreased to the starting media mass as shown in Fig. A.4. The measurements in this study do not account for the possibility of DyN becoming trapped between the media and impact surface, which would be expected to lower the coefficient of restitution.

The ideal gas law was applied to the in situ pressure and temperature data to calculate the amount of nitrogen contained within the milling vessel and the consumption of nitrogen during milling. A slight gas leak rate was observed during milling for times longer than those required for the complete formation of nitride as verified by XRD. In addition, there are discontinuous jumps in pressure at the beginning and end of every milling run. This is caused by mechanical heating from media impact and friction resulting in a fast rise in the gas temperature and consequently the measured pressure. The temperature sensor takes longer to equilibrate, resulting in an apparent increase of moles of nitrogen within the milling vessel. The calculated consumption data must be corrected for the leak rate as well as for the temperature/pressure equilibration lag. The details of these corrections are described in more detail in a complementary work by Jaques *et al*. [33].

Finally, the theoretical moles of nitrogen required to form stoichiometric nitrides was calculated for each milling run and used to normalize the moles consumed data as a measure of the reaction extent, α. The adhesion of unreacted metal to the milling tools makes x-ray diffraction or chemical verification of the reaction extent calculated from gas consumption data unreliable [5], though a recent detailed study on milled non-adhering $Mg(Fe,Co,Ni)H_2$ systems found the calculated reaction extent to agree within 5% of that measured by refined XRD [3].

During milling experiments both under pure argon and under nitrogen, it was observed that dysprosium had a slight tendency to segregate to the vessel lid during milling where it was infrequently struck by media. This results in a pronounced knee in the plot of nitrogen consumption during milling. This material is still converted into

nitride eventually, but the processes is much slower as a result of the infrequent media impacts. In addition, initiation effects such as fracturing existing oxide films and coating the milling tools with ductile dysprosium are expected. Since these effects are both difficult to observe and of little relevance to the steady-state milling kinetics, only the range intermediate range of reaction extent, $0.05 < \alpha < 0.6$, was considered. Above and below this range, the fundamental assumption that the milling tools are coated by reactive metal cannot be justified.

To begin a discussion of milling kinetics, a summary of the key experimental milling results is helpful.

When a milling run begins, elemental dysprosium quickly coats the milling media, increasing their mass as well as decreasing their coefficient of restitution. The increase in mass makes media impacts more energetic, while the decrease in coefficient of restitution increases the energy transfer during an impact. As milling progresses, nitrogen reacts with the dysprosium coated on the media and vessel to form DyN powder that is not adhered to either the media or the vessel. The reaction rate increases with milling speed and appears to accelerate during milling at least up to 70% of theoretical completion as shown in Fig. A.6. After several hours of reactive milling, high purity DyN is the only compound detected by XRD.

The nitrogen consumption data calculated from *in situ* temperature and pressure monitoring of the experiments described above is expressed as a function of time for each milling speed, and the kinetics effects of the milling energy are extracted by analogy to thermal kinetics.

A.4 Kinetics Analysis

In a traditional approach to kinetics analysis, one often begins by parameterizing the functional dependence of α on the experimental conditions in terms of separated variables [34]:

$$\frac{d\alpha}{dt} = f(\alpha)h(P)\,k(T) \tag{2}$$

Here $f(\alpha)$ describes the geometry of the reaction, $k(T)$ is the familiar Arrhenius temperature dependence of the kinetics determined by some activation energy, E_A, and the prexponential k, and $h(P)$ denotes the possible effect of partial pressure in reactions involving gasses. Separating and integrating Eq. 2 yields the integral form, $g(\alpha)$:

$$\int_0^{\alpha} \frac{d\alpha}{f(\alpha)} = g(\alpha) = h(P)\,k(T)t \tag{3}$$

In Eq. 3, $g(\alpha)$ describes the manner in which changing the extent of reaction affects the continuing propagation of the reaction. In classic kinetics, $g(\alpha)$ is often termed the "geometric reaction model."

In the present analysis, the gas-solid reaction is assumed to be primarily driven by milling media impacts with a rate related to the energy of an impact instead of being driven by thermal energy, similar to previous investigations [6, 35]. In addition, the experimental work presented here holds the nitrogen pressure P_{N2} in large excess, which limits pressure effects. The average milling temperature varies over only a small range in which thermally activated diffusion is assumed to be small. Thus, Eq. 3 is rewritten to reduce the effects of pressure $h(P_{N2})$ and temperature $k(T)$ to a constant, A, and to accommodate the temperature-analogous effects of mechanical work, $M(E_b)$. The impact energy, E_b, will depend on the angular frequency, v, of the mill, the mass of the media, m_b, and the elasticity of the impact, C_R [14, 26]:

$$g(\alpha) = A\,M(E)\,t \qquad A(T, P_{N_2}),\ E(\nu, m_b, C_R) \tag{4}$$

The apparent mechanical rate constant, *M(E),* describes the effect of the mechanical milling energy on the reaction rate. The geometric reaction model, *g(α)*takes into account the time-independent effects of the extent of reaction. In a milling system, the progression of the reaction may change the mechanical properties of the milled material, and *g(α)* must therefore also account for the changes in milling energetics. Therefore, *g(α)* in Eq. 4 is rewritten as *g'(α)* to explicitly account for a yet to be determined effect of reaction extent on energy transfer, *E(α)*:

$$g'(\alpha) = A\,M(E)\,E(\alpha)t \tag{5}$$

In the following sections, *g'(α)* and *M(E)* will be obtained by fitting nitrogen consumption data from milling runs conducted at speeds of 350-650 rpm. The variation of impact energy transfer *E(α)* will be determined from media mass data and drop tests. Finally, the obtained expressions for *g'(α)* and *E(α)* will be employed to determine the reaction model *g(α).*

A.4.1 Reaction Model Development

A.4.1.1Empirical Reaction Model

The reaction extent versus milling time at various speeds, calculated from the gas consumption data, is shown in Fig. A.6. The data clearly shows an accelerating rate over the range of interest $0.05 < \alpha < 0.6$. Kinetics data of unknown form but accelerating rate is often fit by a power law model, usually given as [36]:

$$\alpha(t) = (kt)^n \ \leftrightarrow\ \alpha^{1/n} = (kt) \tag{6}$$

where on the right side of Eq. 6 the expression has been rearranged into an expression for the reaction extent as a function of time. In the present case of reaction kinetics that

accelerate with increasing milling time, a power law expression analogous to Eq. 6 was used to derive fitting parameters:

$$\alpha(t) = Bt^m \tag{7}$$

This empirical model is not assumed to have physical meaning in the milling system. Rather, Eq. 7 is used to separate the reaction rate dependence on the milling parameters from the milling-time independent effects such as reaction geometry. Fits to the data are shown as dashed red lines in Fig. A.6, and obtained values of B and m are summarized in Table A.3. Rearranging Eq. 7 as in Eq. 6:

$$\alpha^{1/m} \cong \left(B^{1/m}\, t\right) \tag{8}$$

Since this study is concerned with the effects of mechanical energy on milling reaction rate, the apparent thermal rate constant, k, is replaced in Eq. 6 by the apparent *mechanical* rate constant, M_a. Substituting Eq. 7 into Eq. 4 produces the empirical reaction model:

$$g'(\alpha) \cong \alpha^{\frac{1}{m}} = A\, M_a(E)\, E(\alpha) t \tag{9}$$

Eq. 9 allows the graphical evaluation of the mechanical rate dependence of the reactive milling kinetics by plotting $B^{1/m} = A\, M_a$ versus milling speed as shown in Fig. A.7.

A.4.1.2 Dependence of Reaction Rate on Milling Energy

The values of *m* and *B* obtained from the data fitting shown in Fig. A.6 are both plotted versus the angular frequency of the mill in Fig. A.7 along with best fit lines. From Fig. A.7, it can be seen that the value of *m* decreases slightly with increasing milling speed, while M_a depends on the cube of the angular frequency:

$$M_a(E) = M_0\, \nu^3 \tag{10}$$

Relationships linear in v^3 have been previously observed in high energy ball milling [35]. Together with the angular frequency dependence found by dimensional analysis presented in Table A.2, the data suggest that the mechanical rate constant for nitridation is directly proportional to the milling intensity $I = vE_b$ *(J/s)*. A plot of this relationship is shown in Fig. A.8, which gives a value of M_0 = 9.16±0.31 (s/mJ N), where N is the total number of media. This M_0 is the mechanical rate of the process, analogous to the rate constant, k, in the traditional thermal kinetics of Eq. 6. Since the progress of the reaction has a linear dependence on milling intensity, vE_b, the assumption in Eq. 8 and Eq. 9 that $B^{1/m} = M_a$ is justified, and it is appropriate to consider the effects that changing reaction extent could have on the impact energy, E_b. In turn, this will allow separating the effects of reaction extent on milling energetics from the geometric reaction model, $g'(\alpha)$, on the left side of Eq. 9.

A.4.1.3Effects of Reaction Extent on Coefficient of Restitution

As shown in Fig. A.4 and A.5, the thickness of material coating the media decreases with increasing reaction extent. Almost immediately after the start of milling, dysprosium adheres to the media and the mass of each media is increased by the amount of metal Δm_{Dy} adhered to them. This adhered mass may be approximated by considering the available mass of metal and media surface area:

$$\Delta m_{Dy} \cong \frac{m_c}{N_b} \frac{A_b}{A_v + A_b} \tag{11}$$

where A_b is the cumulative media surface, A_v the area of the vessel wall, m_c the mass of the milled charge of metal, and N_b the total number of media. As shown in Fig. A.5, the dysprosium milled under the present experimental conditions has $\Delta m = 0.044\ m_b$, where m_b is the clean media mass. As metal reacts during milling, the media mass decreases

from $m_b + \Delta m$ down to the original value of m_b, which in turn linearly decreases the impact energy:

$$E_b'(\alpha) = E_b \left[1 + \frac{\Delta m}{m_b}(1 - \alpha)\right] \quad (12)$$

The kinetic energy of a milling media at impact, E_b, may be calculated by considering the milling kinematics [14].

A.4.1.4 Effects of Reaction Extent on Media Mass

The data in Fig. A.5 demonstrate that C_R depends nearly linearly on the thickness of the media coating. As discussed previously, dysprosium is the major component of the material adhered to the media during reactive milling, while the nitride is the primary component of the free powder. Thus, to a reasonable approximation, the value of C_R during reactive milling of dysprosium in nitrogen linearly increases with reaction extent. The effective energy transferred to the milled material during an impact event, E_b, depends on the elasticity of the impact:

$$E(C_R) = E_b(1 - C_R) \quad (13)$$

The fit of C_R vs α from Fig. A.4 is found to be:

$$C_R(\alpha) = (0.6 + 0.3\alpha) \quad (14)$$

A.4.1.5 Combined Effects of Reaction Extent on Milling Energy Transfer

Now Eq. 14 may be substituted into Eq. 13 to describe the dependence of the energy transferred during impact on the reaction extent:

$$E(\alpha) = E_b'(0.4 - 0.3\alpha) \quad (15)$$

Eq. 15 describes an increase in the elasticity of media impacts with increasing reaction extent and the corresponding decrease in energy transferred to the impacted material. Substituting Eq. 11 and Eq. 12 into Eq. 15 gives the change in energy transferred as a function of α:

$$\frac{E(\alpha)}{E_b} = \left[1 + \frac{m_c}{N_b\, m_b}\, \frac{A_b}{A_v + A_b}\, (1-\alpha)\right](0.4 - 0.3\alpha) \quad (16)$$

A.4.2 Analytical Reaction Model

Having calculated the effects of changing reaction extent on the energetic of milling media impacts, an analytical reaction model may be found that accounts for both media energetics and reactant geometry. Combining Eq. 5 and Eq. 8 gives an expression for the true geometric reaction model g(α):

$$g(\alpha) = \frac{g'(\alpha)}{E(\alpha)} \cong \frac{\alpha^{\frac{1}{m}}}{E(\alpha)} \quad (17)$$

In Fig. A.9, $\alpha^{1/m}$ is plotted vs. 1/E(α) for all milling speeds. This allows the graphical determination of the full geometric model, *g(α)*, in terms of the experimental reaction extent and the calculated dependence of milling media energetic on the extent of reaction. The inset plot in Fig. A.9 shows the geometrical model exponent, *n*, for various milling speeds. It is clear that *n* is close to 2 at all milling speeds and decreases slightly with increasing milling speed. Thus, a reaction kinetics model based on nucleation on a surface geometry [36, 37] is suggested:

$$g(\alpha) = \alpha^{1/n} = A\, M(E_b)\, t \quad (18)$$

Substituting Eq. 10, Eq. 16, and Eq. 17 into Eq. 18:

$$\alpha^{1/n} = A\, M_0 v^3 m_b t \quad (19)$$

Fig. A.10 shows that the experimental data input into the reaction model of Eq. 18 results in linear fits, supporting the possibility that Eq. 19 is a valid kinetic model for the reaction of nitrogen with dysprosium during high energy ball milling. The reaction rate depends explicitly on the energy input, which acts on the Hertzian area of impact to

create fresh surfaces as described in Section A.1.2 above. These results may be interpreted as describing a reactive milling process in which ductile metal, adhered to the milling tools, is gradually consumed to form a powdered nitride.

Table A.3 Power fits for apparent (Fig. A.6) and energy-corrected (Fig. A.9) geometric models

	Apparent Model $g'(a)=\alpha^{1/m}$			Energy-corrected Model $g(a) = \alpha^{1/n}$		
RPM	B	m	R^2	G	n	R^2
350	0.047	1.790	0.997	3.912	2.436	0.997
425	0.238	1.641	0.996	3.947	2.250	0.997
425	0.133	1.661	0.997	4.129	2.458	0.998
500	0.373	1.777	0.998	3.965	2.447	0.997
500	0.224	1.785	0.999	3.953	2.448	0.997
575	0.872	1.449	0.999	3.991	2.007	0.997
575	0.565	1.582	0.999	3.995	2.188	0.997
650	1.335	1.365	0.981	4.016	1.901	0.997
650	0.983	1.437	0.998	3.991	1.988	0.996

A.4.2.1 Limitations of the model

The milling model of Eq. 18 depends on the assumption that the milling tools are quickly coated by an adherent layer of dysprosium metal, and that the tools remain coated throughout the reaction. This assumption was validated in the intermediate range by opening the milling jar and measuring the mass, thickness, and phase content of the adhered material. However, the coating process is not instantaneous, so the derived model is not representative of the initial reaction behavior.

The analysis of the coefficient of restitution was performed for only one milling speed, 500 rpm, and the bounce test apparatus used was capable of achieving velocities of only up to approximately 2 m/s rather than the 4-5 m/s predicted to occur during milling. The coefficient of restitution is relatively insensitive to changes in velocity when the pressure at impact is higher than the yield stress [26], which is satisfied in the present

case, but the work presented here is necessarily an approximation. Variation in the true value of CR with milling speed may account for the change seen in the reaction order, *n*, in Fig. A.9 and Eq. 18.

Reactive milling should be expected to constantly disrupt the reacting surface by comminuting surface films. However, as the $2Dy + N_2 \rightarrow 2DyN$ reaction progresses, increasing amounts of DyN will be trapped in media impacts. This will result in some impact energy dissipation by the trapped nitride powder and reduce the effective metal surface refinement. The potential for energy dissipation by nitride products increasing with reaction extent is not considered in the model.

Finally, at high reaction extents, the adherent metal coating will be consumed and eventually wear through, reducing the number of media-dysprosium-wall impacts in favor of direct media-wall or media-nitride-wall impacts. This apparent slowing of reaction rate should be properly understood as a decrease in the number of effective impacts and thus a decrease in reactive milling dose, rather than as indicative of a process controlled by the growth of nuclei or similar decelerating process.

A.5 Conclusions

The reaction of dysprosium metal during high energy milling under nitrogen atmosphere has been quantified by monitoring the temperature and pressure *in situ*. A model of reactive milling kinetics for the formation of dysprosium nitride has been developed that predicts the rate of nitride formation in reactive milling to be limited by the areal energy input of media impacts. This novel result is explained in terms of generation of atomically rough chemically active sites within the hertzian impact area followed by dissociative chemisorbtion of nitrogen on the active surface with consequent

formation of nitride. Equivalently, impacts could be seen as comminuting thin films of nitride within the impact area to allow for fast diffusion to the surface. Gas-solid reactions during reactive milling of other rare earths are predicted to follow the model so long as the following conditions are met:

a. The solid is ductile and coats the milling tools
b. There is a low activation energy barrier for dissociative chemisorbtion on the solid
c. There is low solubility of the gas in the solid

These conditions should be met by many if not all of the lanthanides. These results help to demonstrate the reactive milling as a viable approach to synthesis of the rare earth and actinide nitrides. In addition, the demonstrated importance of considering the coefficient of restitution variability during mechanochemical synthesis provides a foundation for further study of the gas-solid reactions during high energy milling.

References

[1] C. Suryanarayana, Mechanical alloying and milling, Prog. Mater. Sci. 46[1-2] (2001) 1-184.

[2] J. M. Bellosta von Colbe, M. Felderhoff, B. Bogdanovic, F. Schuth, and C. Weidenthaler, One step direct synthesis of a Ti-doped sodium alanate hydrogen storage material, Chem. Comm. [37] (2005) 4732-34.

[3] J. Zhang, F. Cuevas, W. Zaïdi, J. Bonnet, L. Aymard, J. Bobet, and M. Latroche, Highlighting of a single reaction path during reactive ball milling of Mg and TM by quantitative H2 gas sorption analysis to form ternary complex hydrides (TM = Fe, Co, Ni), J. Phys. Chem. C, 115 [11] (2011) 4971–4979

[4] M. A. Bab, L. A. Baum, and L. Mendoza-Zelis, Autocatalytic effects in the mechanically induced hydriding of refractory metals, Physica. B. 389[1] (2007) 193-97.

[5] M.A. Bab, L. Mendoza-Zelis, and L.C. Damonte, Nanocrystalline HfN produced by mechanical milling: Kinetic aspects, Acta Mater. 49 [20] (2001) 4205-4213.

[6] M. A. Bab and L. Mendoza-Zelis, A model for the kinetics of mechanically assisted gas-solid reactions, Scripta Mater. 50[1] (2004) 99-104.

[7] A. N. Streletskii, P. Y. Butyagin, and A. V. Leonov, Mechanochemical solid-gas reactions: Kinetics and products of interaction between Zr and CO, Colloid J. 58[2] (1996) 238-45.

[8] A. N. Streletskii, A. V. Leonov, and P. Y. Butyagin, On the role of intergrain boundaries in solid/gas mechanochemical synthesis, Ismanam-96, 235[2] (1997) 181-86.

[9] A. Yazdani, M. J. Hadianfard, and E. Salahinejad, A system dynamics model to estimate energy, temperature, and particle size in planetary ball milling, J. Alloy. Compds. 555 (2013) 108-11.

[10] A. Iasonna and M. Magini, Power measurements during mechanical milling. An experimental way to investigate the energy transfer phenomena, Acta Mater. 44[3] (1996) 1109-17.

[11] M. Magini, A. Iasonna, and F. Padella, Ball milling: An experimental support to the energy transfer evaluated by the collision model, Scripta Mater. 34[1] (1996) 13-19.

[12] P. Bellon and R. S. Averback, "Nonequilibrium Roughening of Interfaces in Crystals Under Shear – Application to Ball-milling, Phys. Rev. Lett. 74[10] (1995) 1819-22.

[13] M. Magini, C. Colella, A. Iasonna, and F. Padella, Power measurements during mechanical milling - II. The case of "single path cumulative" solid state reaction, Acta Mater. 46[8] (1998) 2841-50.

[14] P. P. Chattopadhyay, I. Manna, S. Talapatra, and S. K. Pabi, A mathematical analysis of milling mechanics in a planetary ball mill, Mater. Chem. Phys. 68[1-3] (2001) 85-94.

[15] B. J. Jaques, B. M. Marx, A. S. Hamdy, and D. P. Butt, Synthesis of uranium nitride by a mechanically induced gas-solid reaction, J. Nucl. Mater. 381[3] (2008) 309-11.

[16] P. G. Callahan, B. J. Jaques, B. M. Marx, A. S. Hamdy, D. D. Osterberg, and D. P. Butt, Synthesis of dysprosium and cerium nitrides by a mechanically induced gas-solid reaction, J. Nucl. Mater. 392[1] (2009) 121-24.

[17] G. Alanko and D. Butt, Mechanochemical Synthesis of Cerium Monosulfide, J. Amer. Ceram.Soc. (2014) In Press.

[18] G. Kaupp, Reactive milling with metals for environmentally benign sustainable production, Crys. Eng. Comm. 13[9] (2011) 3108-21.

[19] F. P. Netzer and J. A. D. Matthew, Surfaces of Rare Earth Metals, Rep. Prog. Phys. 49[6] (1986) 621-81.

[20] Z. Bastl, S. Cerny, and M. Kovar, Calorimetric and XPS Study of the Effect of Copper on the Sorption Properties of Dysprosium, Appl. Surf. Sci. 68[2] (1993) 275-83.

[21] J. A. Schreifels, J. E. Deffeyes, L. D. Neff, and J. M. White, An X-Ray Photo-electron Spectroscopic Study of the Adsorption of N2, NH3, NO, AND N2O on Dysprosium, J. Electron Spectrosc. Relat. Phenom. 25[2-3] (1982) 191-209.

[22] S. P. Willson and L. Andrews, Characterization of the reaction products of laser-ablated late lanthanide metal atoms with dinitrogen. Matrix IR spectra of LnN, (LnN)(2), and Ln(NN)(x) molecules, J. Phys. Chem. A 103[10] (1999) 1311-21.

[23] S. P. Willson and L. Andrews, Characterization of the reaction products of laser-ablated early lanthanide metal atoms with dinitrogen. Infrared spectra of LnN, LnN(2), (LnN)(2), and Ln(NN)(x) molecules, J. Phys. Chem. A 102[50] (1998) 10238-49.

[24] G. P. Kushto, P. F. Souter, G. V. Chertihin, and L. Andrews, An infrared spectroscopic and density functional investigation of dinitrogen activation by group IV metal atoms, J. Chem. Phys. 110[18] (1999) 9020-31.

[25] G. P. Kushto, P. F. Souter, and L. Andrews, An infrared spectroscopic and quasirelativistic theoretical study of the coordination and activation of dinitrogen by thorium and uranium atoms, J. Chem. Phys. 108[17] (1998) 7121-30.

[26] K. L. Johnson, "Contact Mechanics," pp. 452 First (paperback) ed. Cambridge University Press: Cambridge, (1985).

[27] J. Y. Huang, Y. K. Wu, and H. Q. Ye, "Ball-milling of Ductile Metals, Mater. Sci. Eng. A. 199[2] (1995) 165-72.

[28] H. J. Fecht, E. Hellstern, Z. Fu, and W. L. Johnson, "Nanocrystalline Metals Prepared by High-energy Ball Milling, Metall. Trans. A. 21[9] (1990) 2333-37.

[29] P. Y. Butyagin, Y. V. Zhernovenkova, and I. V. Povstugar, Work of formation of grain boundaries upon metal plastic deformation, Colloid J. 65[2] (2003) 141-44.

[30] P. Y. Butyagin and A. N. Streletskii, The kinetics and energy balance of mechanochemical transformations, Phys. Solid State 47[5] (2005) 856-62.

[31] R. T. Hukki, "Proposal for a Solomonic Settlement Between the Theories of von Rittinger, Kick, and Bond, Trans. Am. Inst. Min. Metall. Eng. 220 (1961) 403-08.

[32] A. Thomas and L. O. Filippov, Fractures, fractals and breakage energy of mineral particles, Int. J. Miner. Process. 57[4] (1999) 285-301.

[33] B. Jaques, G. Alanko, D. Osterberg, S. Tamrakar, C. Smith, M. Hurley, and D.P. Butt, In-situ Characterization During Reactive Milling of Dysprosium Nitride, In revision. J. Alloys Compds.

[34] M. E. Brown, M. Maciejewski, S. Vyazovkin, R. Nomen, J. Sempere, A. Burnham, J. Opfermann, R. Strey, H. L. Anderson, A. Kemmler, R. Keuleers, J. Janssens, H. O. Desseyn, C. R. Li, T. B. Tang, B. Roduit, J. Malek, and T. Mitsuhashi, Computational aspects of kinetic analysis Part A: The ICTAC kinetics project-data, methods and results, Thermochim. Acta 355[1-2] (2000) 125-43.

[35] F. J. Gotor, M. Achimovicova, C. Real, and P. Balaz, Influence of the milling parameters on the mechanical work intensity in planetary mills, Powder Technol. 233 (2013) 1-7.

[36] W. E. Brown, D. Dollimore, and A. K. Galwey, Reactions in the Solid State, pp. 340 1 ed. Vol. 22. Elsevier Scientific: New York, NY, (1980).

[37] A. K. Galwey and M. E. Brown, Isothermal kinetic analysis of solid-state reactions using plots of rate against derivative function of the rate equation, Thermochim. Acta 269 (1995) 1-25.

Figures

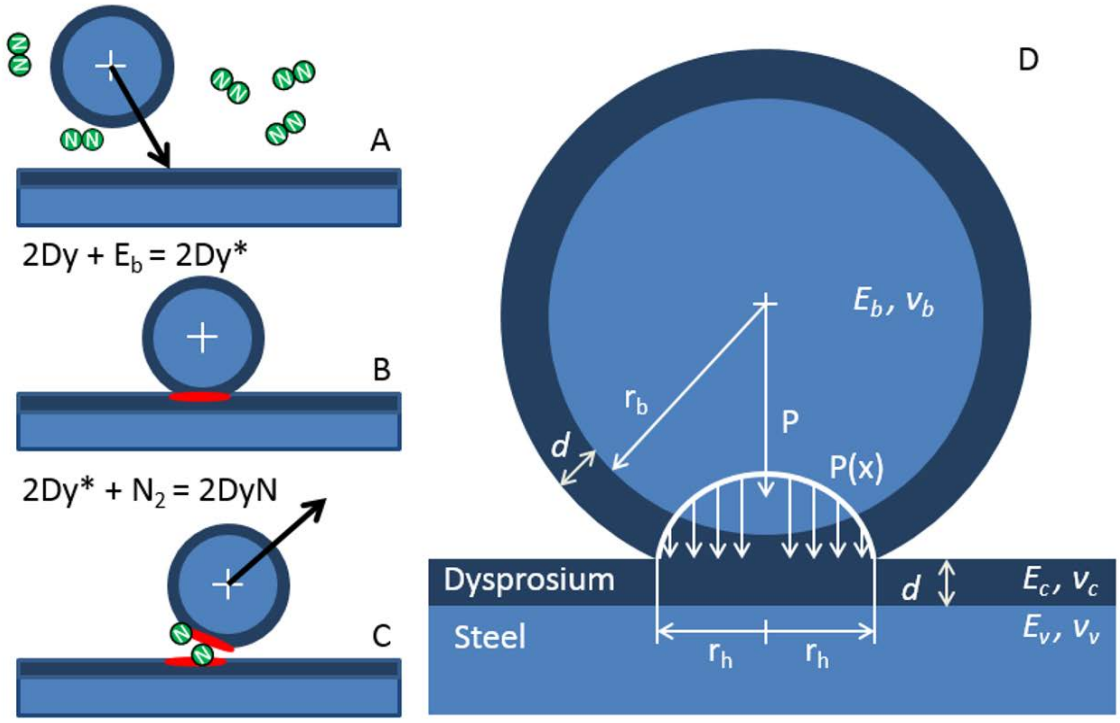

Figure A.1 This figure (a-c) shows a schematic of an impact event renewing the reactive surface. (a) media approaches the vessel wall (b) media impact transfers energy to the impact area πr_h^2 (c) media rebound exposes activated surfaces on the wall and media. Part (d) shows a schematic of the impact event between a dysprosium-coated media and the coated vessel. Listed quantities in (d) are defined in the text.

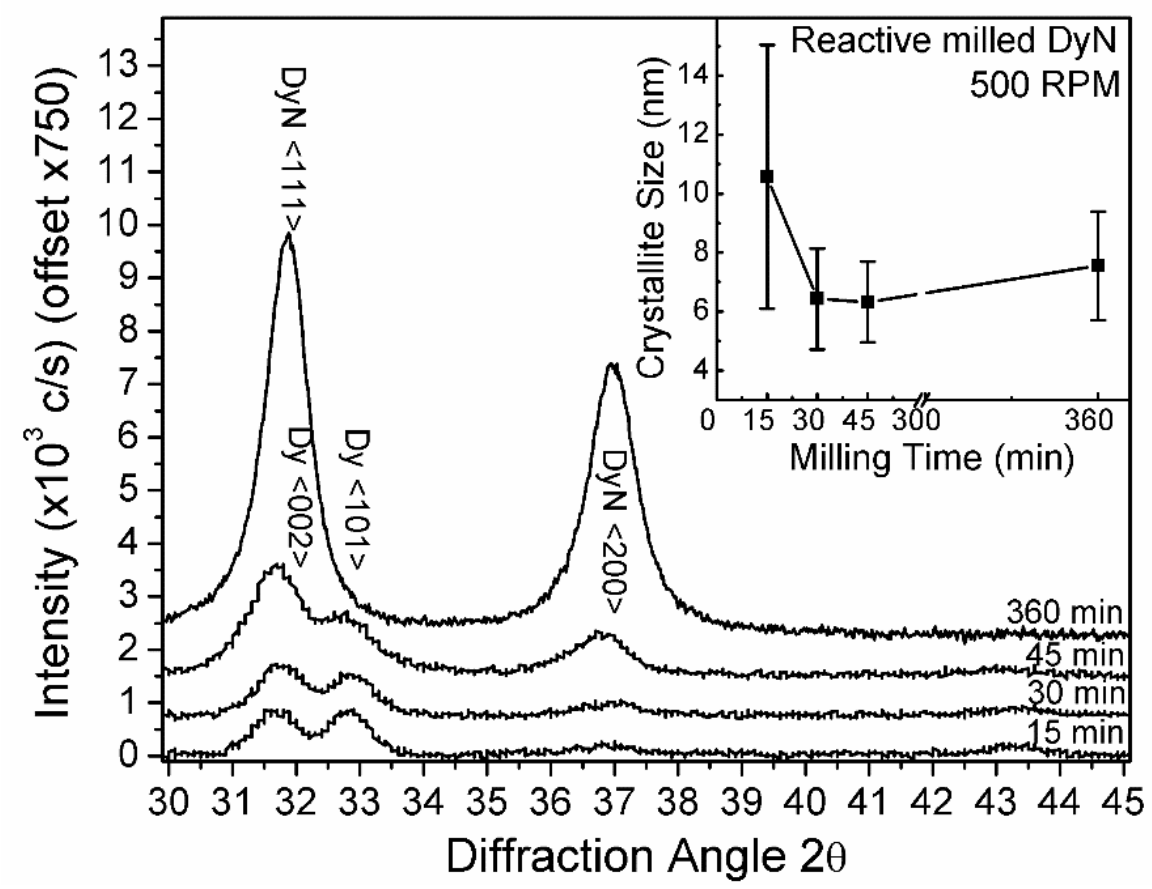

Figure A.2 This figure shows x-ray diffraction plots collected after milling Dy in N_2 at 500 rpm. Milling times are indicated on plot. The inset shows the average DyN crystallite size calculated by the Scherrer equation from the FWHM of five simultaneously-fit peaks.

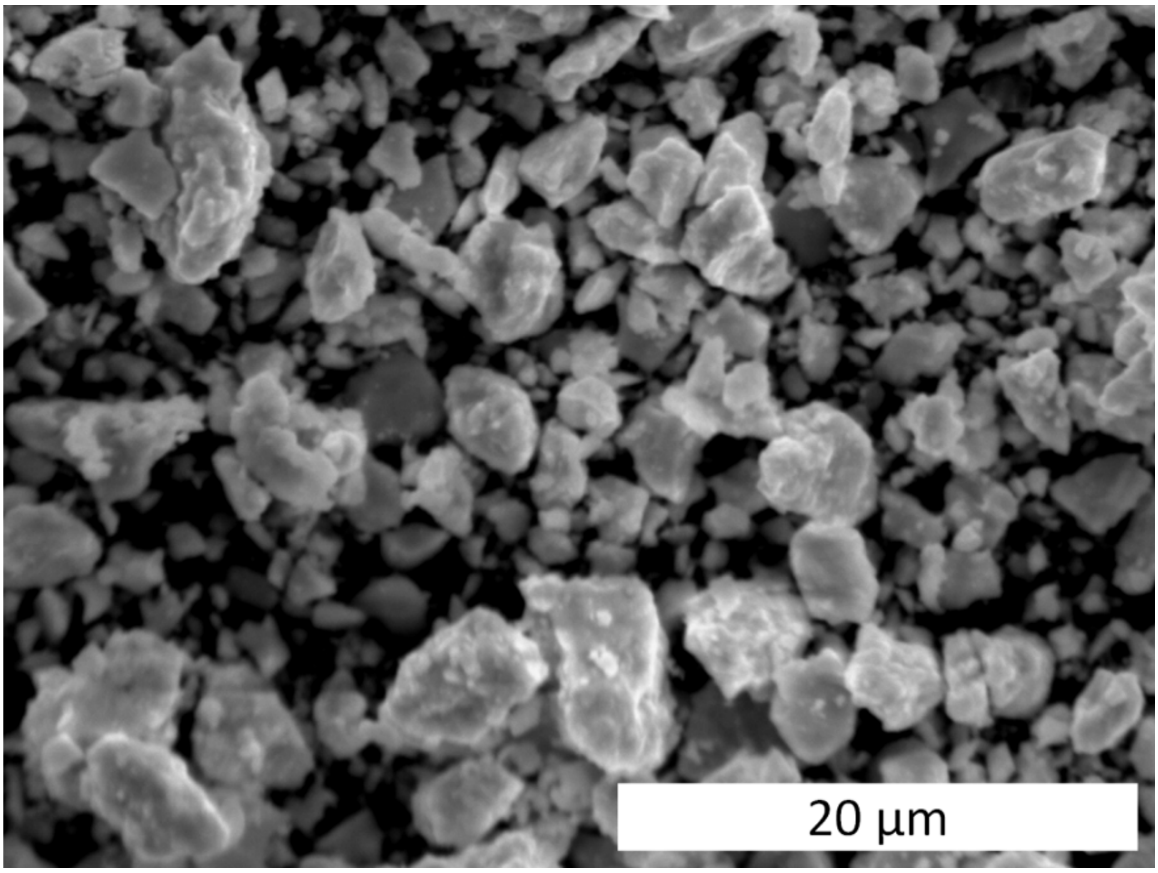

Figure A.3 This SEM micrograph shows a secondary electron image of DyN formed by milling dysprosium for 6 hours at 500 rpm in nitrogen.

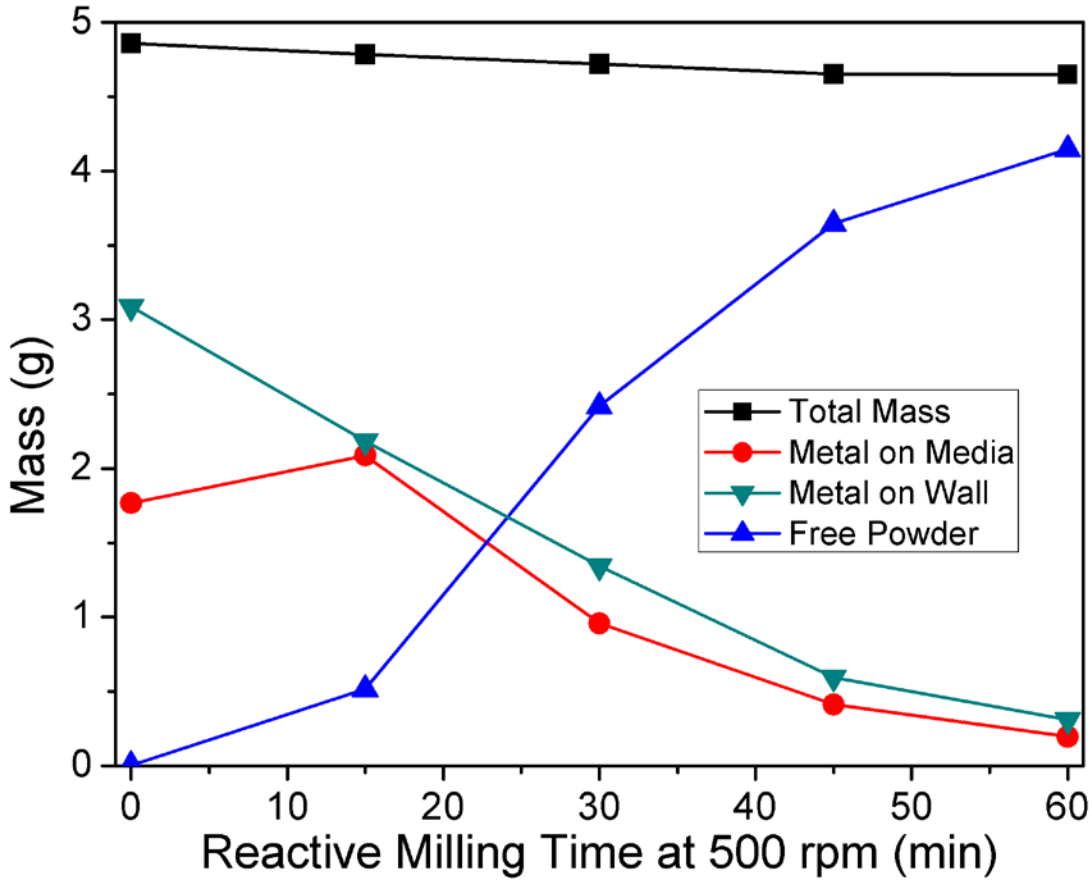

Figure A.4 This plot tracks the disposition of Dy and DyN during reactive milling at 500 rpm. Before the start of RM, ductile Dy was coated onto the media and walls by premilling in argon. The media and wall traces (red circles and green down arrows) show consumption of Dy and formation of free DyN powder (blue up arrows). Total mass in the vessel (black squares) decreases as coated media are removed for further characterization. Color online.

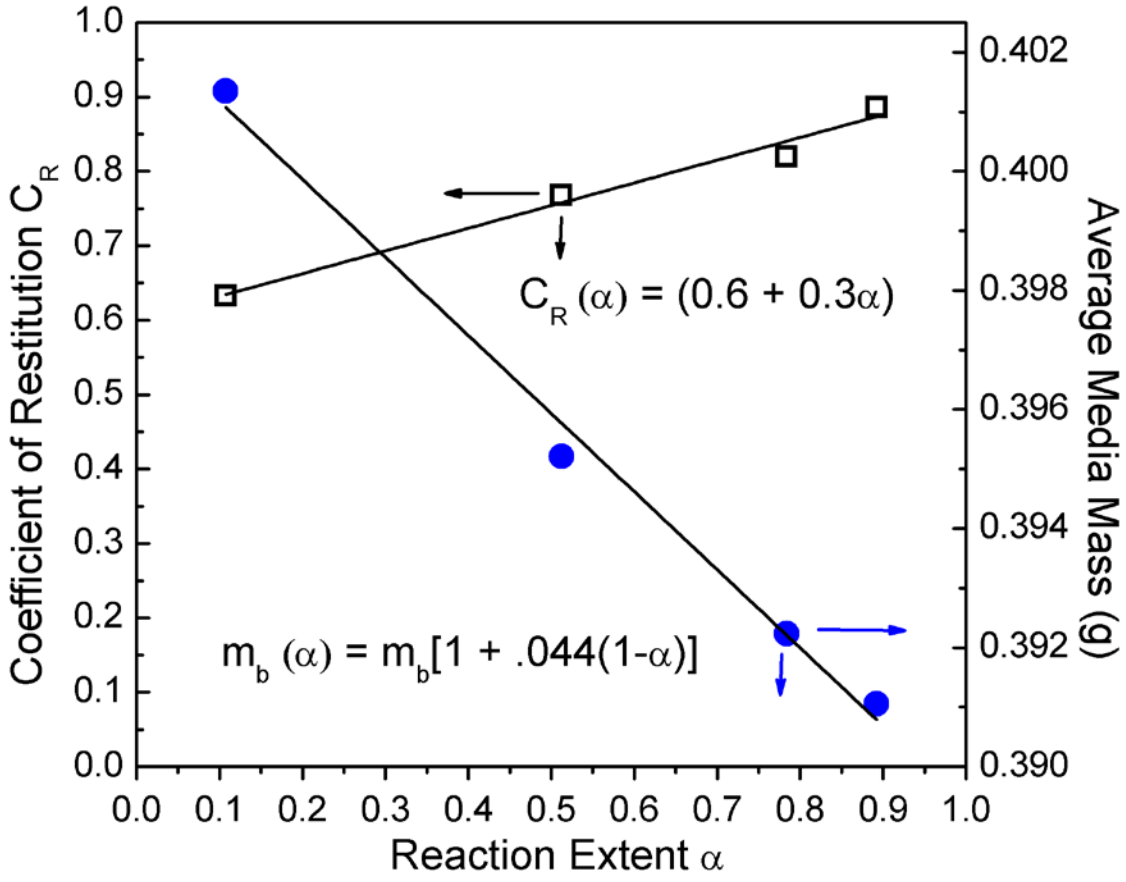

Figure A.5 This plot shows the variation of the coefficient of restitution C_R (black open squares) and media mass m (blue circles) with extent of reaction α during reactive milling of Dy in nitrogen. Equations for the best fit lines are shown. Color online.

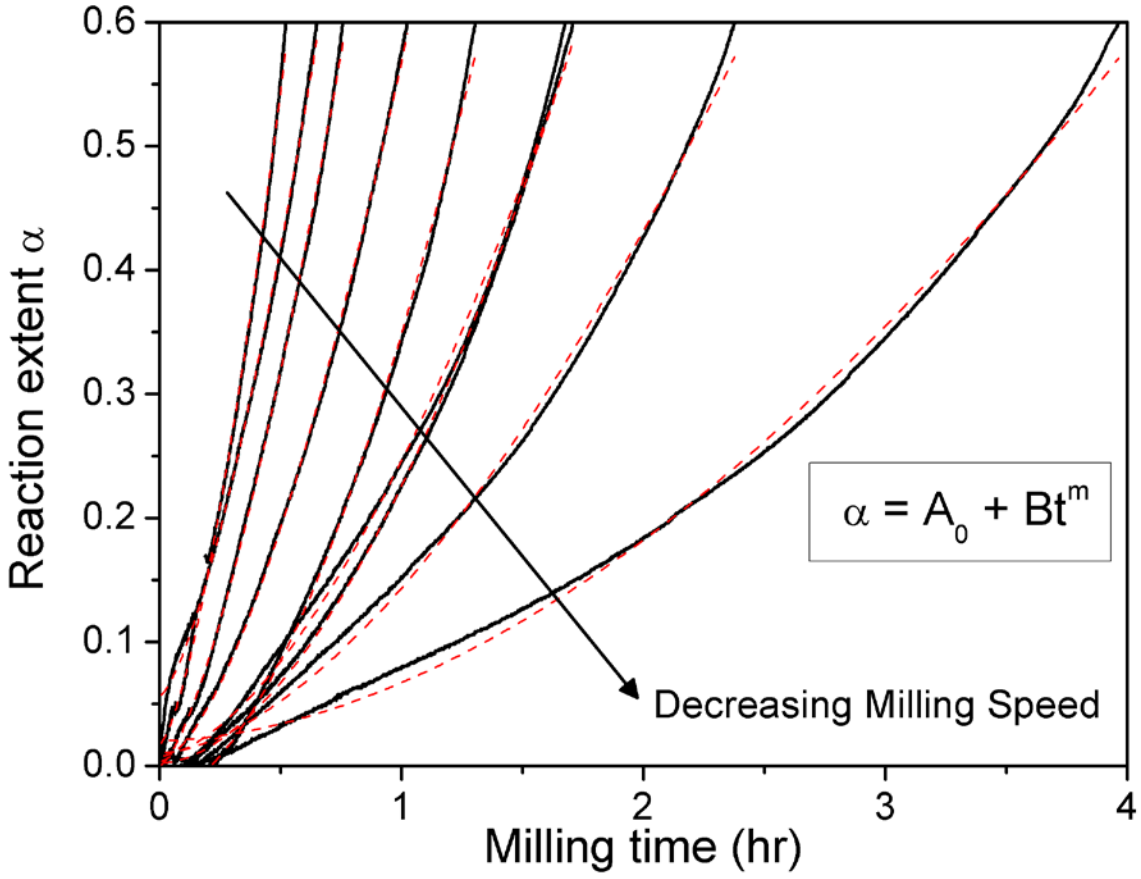

Figure A.6 This figure shows plots of reaction extent data (black traces) fit to the generic power law formula $\alpha = A_0 + Bt^m$ (dashed red traces). The fit coefficients and adjusted r^2 value are tabulated in Table A.3. Color online.

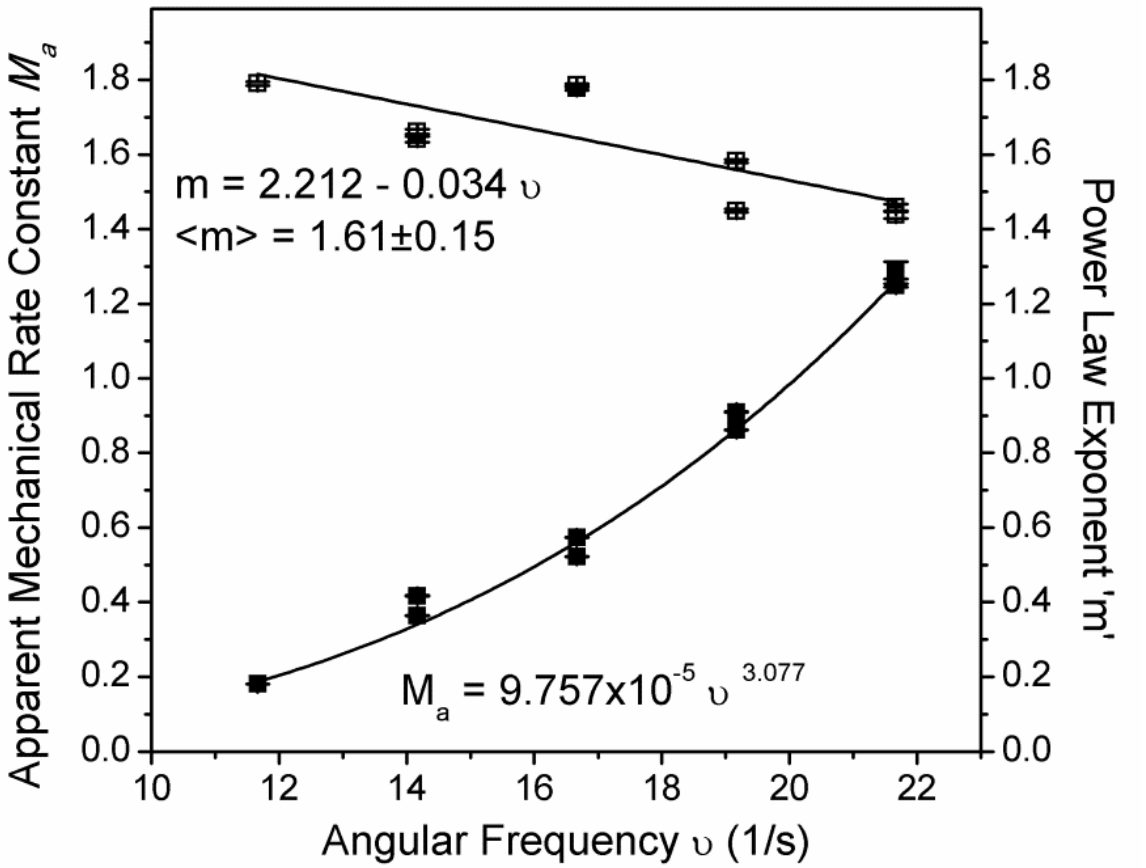

Figure A.7 This figure plots the power law fit coefficients M_a and m versus the angular frequency of the milling vessel. Equations for the best fit lines are shown.

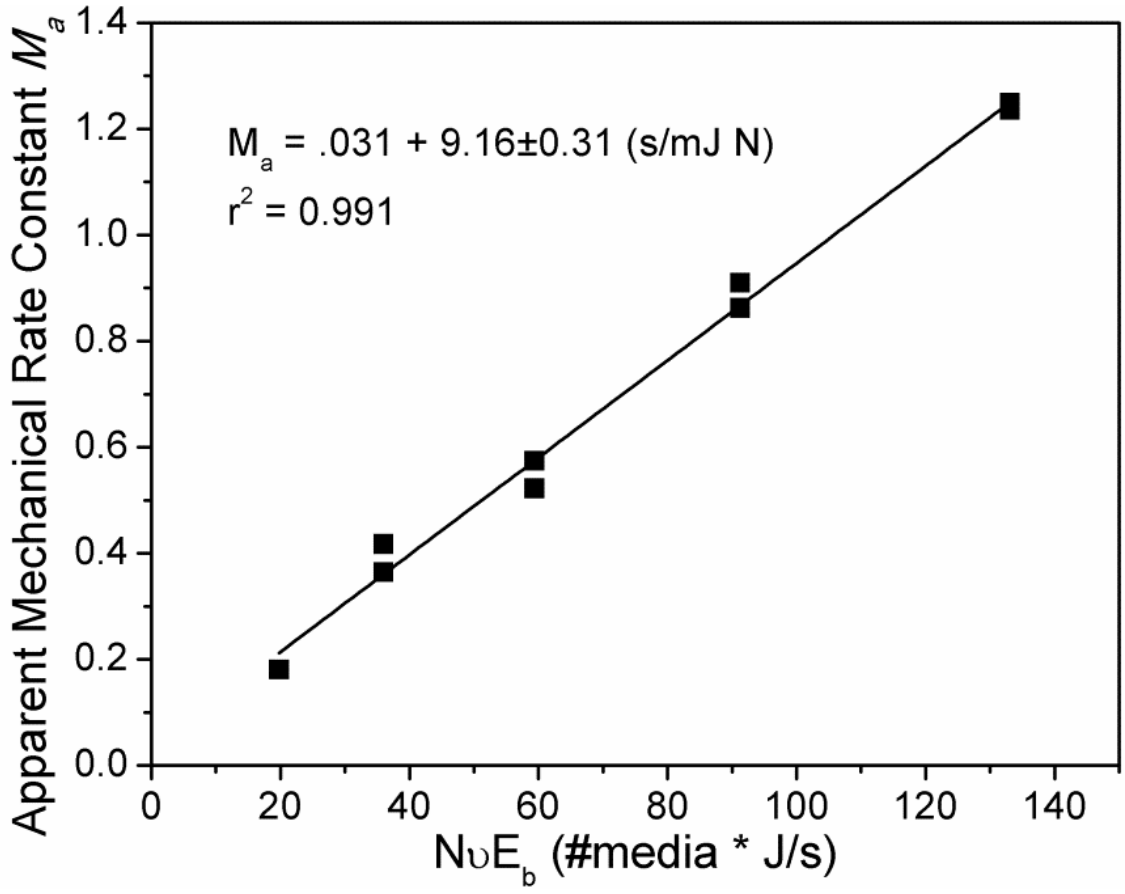

Figure A.8 This figure shows fitted values for M_a plotted versus the milling intensity per media $\upsilon E_b/N$. The equation for the best fit line is shown, and the very good correlation indicates a reaction rate that depends on the milling intensity.

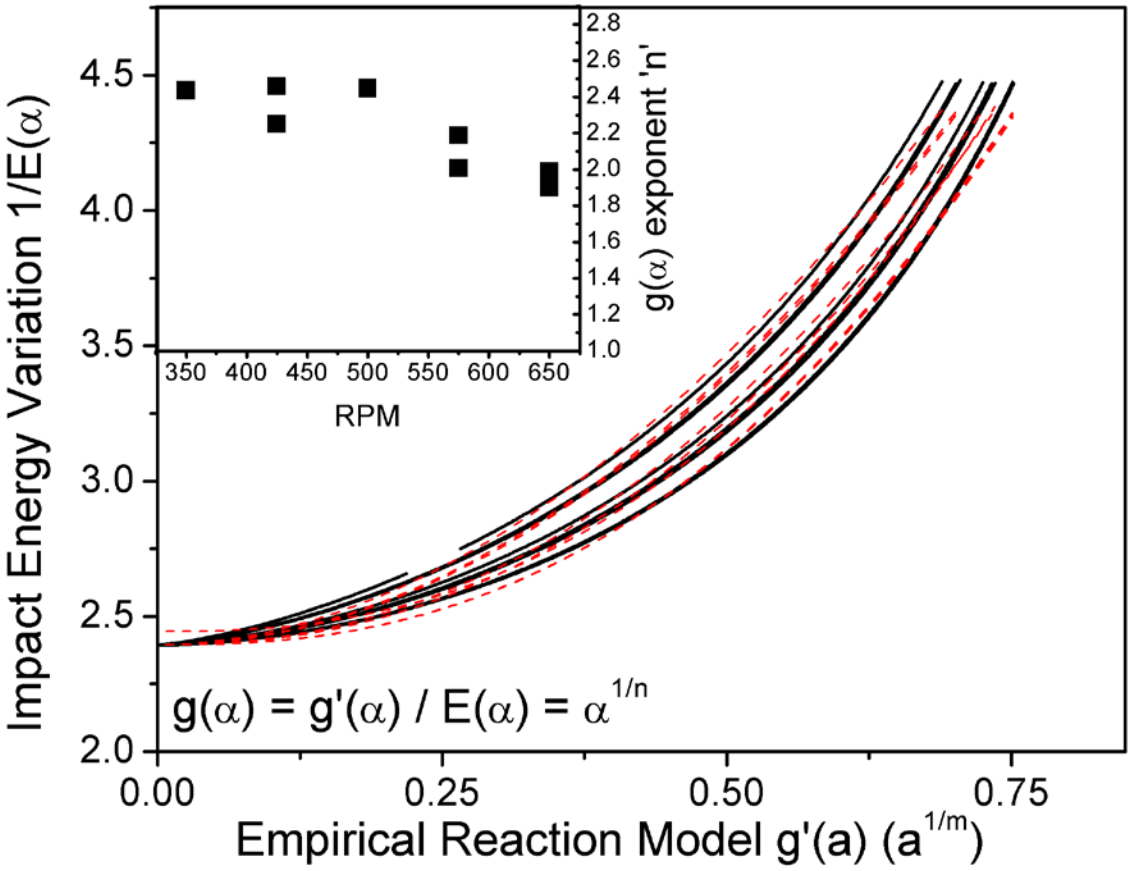

Figure A.9 This figure shows the graphical determination of the reaction model g(α) from Eq. 17 with experimental data from Fig. A.5. The red dashes are best fits to the model. The inset table lists the obtained exponents from a fit to $1/E(\alpha) = A + G(\alpha^{1/m})^n$, and the inset plot shows the reaction model $g(a) = \alpha^{1/n}$.

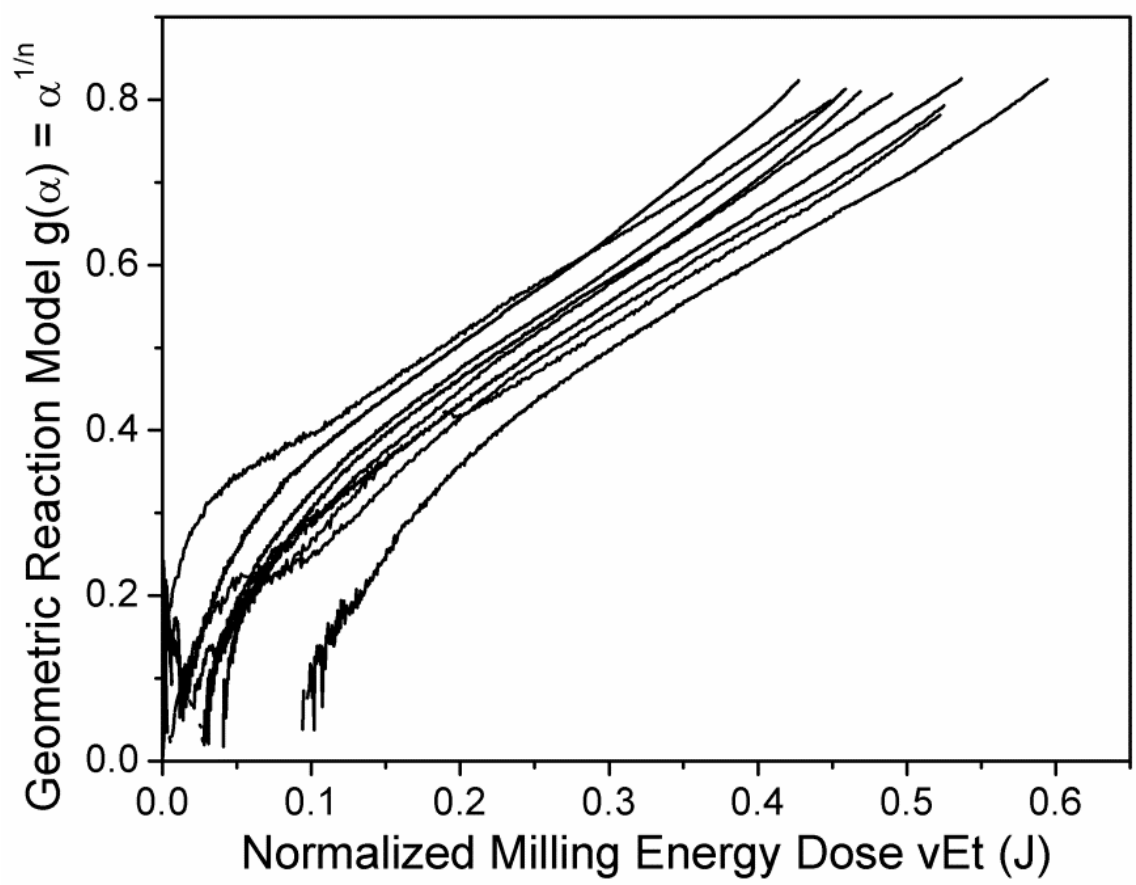

Figure A.10 This figure shows the energy-corrected reaction model g(α) plotted against the normalized milling dose $(vEt)_{rpm} / (vEt)_{650}$. The linear slope outside of the initiation region provides support for the assumed model.